# Artificial Graphene in Nano-patterned GaAs Quantum Wells and Graphene Growth by Molecular Beam Epitaxy

Sheng Wang

Submitted in partial fulfillment of the

requirements for the degree of

Doctor of Philosophy

in the Graduate School of Arts and Sciences

COLUMBIA UNIVERSITY

2016

ABSTRACT

Artificial Graphene in Nano-patterned GaAs Quantum Wells and Graphene Growth by Molecular Beam Epitaxy

Sheng Wang

In this dissertation I present advances in the studies of artificial lattices with honeycomb topology, called artificial graphene (AG), in nano-patterned GaAs quantum wells (QWs). AG lattices with very small lattice constants as low as 40 nm are achieved for the first time in GaAs. The high quality AG lattices are created by optimized electron-beam (E-beam) lithography followed by inductively coupled plasma reactive-ion etching (ICP-RIE) process. E-beam lithography is used to define a honeycomb lattice etch mask on the surface of the GaAs QW sample and the optimized anisotropic ICP-RIE process is developed to transfer the pattern into the sample and create the AG lattices. Such high-resolution AG lattices with small lattice constants are essential to form AG miniband structures and create well-developed Dirac cones.

Characterization of electron states in the nanofabricated artificial lattices is by optical experiments. Optical emission (photoluminescence) yields a determination of the Fermi energy of the electrons. A significant reduction of the Fermi energy is due to the nano-patterning process. Resonant inelastic light scattering (RILS) spectra reveal novel transitions related to the electron band structures of the AG lattices. These transitions exhibit a remarkable agreement with the predicted joint density of states (JDOS) based on the band structure calculation for the honeycomb topology.

I calculate the electron band structures of AG lattices in nano-patterned GaAs QWs using a periodic muffin-tin potential model. The evaluations predict linear energy-momentum dispersion and Dirac cones, where the massless Dirac fermions (MDFs) appear, occur in the band structures. Requirements of the parameters of the AG potential to achieve isolated and well-developed Dirac cones are discussed. Density of states (DOS) and JDOS from AG band structures are calculated, which

provide a basis to interpret quantitatively observed transitions of electrons involving AG bands.

RILS of intersubband transitions reveal intriguing satellite peaks that are not present in the as-grown QWs. These additional peaks are interpreted as combined intersubband transitions with simultaneous change of QW subband and AG band index. The calculated JDOS for the electron transitions within the AG lattice model provide a remarkably accurate description of the combined intersubband excitations.

Novel low-lying excitation peaks in RILS spectra, interpreted as direct transitions between AG bands without change in QW subband, provide a more direct insight on the AG band structures. We discovered that RILS transitions around the Dirac cones are resonantly enhanced by varying the incident photon energies. The spectral lineshape of these transitions provides insights into the formation of Dirac cones that are characteristic of the honeycomb symmetry of the AG lattices. The results confirm the formation of AG miniband structures and well-developed Dirac cones. The realization of AG lattices in a nanofabricated high mobility semiconductor offers the advantage of tunability through methods suitable for device scalability and integration.

The last part of this thesis describes the growth of nanocrystalline single layer and bilayer graphene on sapphire substrates by molecular beam epitaxy (MBE) with a solid carbon source. Raman spectroscopy reveals that fabrication of single layer, bilayer or multilayer graphene crucially depends on MBE growth conditions. Etch pits revealed by atomic force microscopy indicate a removal mechanism of carbon by reduction of sapphire. Tuning the interplay between carbon deposition and its removal, by varying the incident carbon flux and substrate temperature, should enable the growth of high quality graphene layers on large area sapphire substrates.

# Contents

# List of Figures

# List of Tables

# Acknowledgements

The life of a PhD is always challenging, but that is how we learn things.

First of all I would like to thank my advisor Professor Aron Pinczuk for his great mentorship. I constantly benefit from his unique physics insight and intuition. It has been a pleasure to work with Aron in the cutting edge research, and I always admire his enthusiasm for physics. This thesis would not be possible without his help. Probably the most important thing I learned from Aron is to think bravely. Do not set boundaries on thinking.

I would also like to thank Profs. Richard Osgood, who cares about me a lot directly or through my friend Xiang Meng, Chris A. Marianetti, from who I learned about band structure calculations, Shalom Wind, who provides lots of help with fabrications, Cory Dean, who is always available to offer support to our group, Nanfang Yu, who gave wonderful lectures on optics, James Hone, who rose my initial interest on graphene, Phillip Kim, who taught a wonderful class on graphene and others that provide help during my PhD research.

I learned a lot from Dr. Jorge Garcia, Dr. Ulrich Wurstbauer and Dr. Lara Fernandes dos Santos Lavelli, when we worked together on MBE growth of graphene on dielectric substrates. It is also a pleasure to work with Dr. Yuliya Y. Kuznetsova on artificial graphene project, and I enjoyed the time that Yuliya taught me details about the dilution fridge.

I really benefited from the collaboration with Diego Scarabelli and Dr. Shalom

J. Wind on artificial graphene project and I learned a lot from their expertise on nanofabrication. One step of the fabrication, ICP-RIE etch, is done in Princeton University and I want to thank Dr. George(Pat) Watson, who provides help with their cleanroom facilities. I enjoyed the trips from Columbia to Princeton especially when the weather is nice.

The extraordinary high quality GaAs quantum well samples are grown by Dr. Loren N. Pfeiffer, Ken W. West, Dr. Michael J. Manfra and Dr. Geoff C. Gardner. Special thanks go to Loren as we heavily rely on his wide knowledge on semiconductor heterostructures. I would also like to thank Dr. Vittorio Pellegrini, who provides lots of insights on the artificial graphene project. I also enjoyed the period of overlap with his students Tommaso Satzoukidis and Dr. Andrea Gamucci. I also benefited from working with Sebastian Dietl during his visit of Columbia.

I spent a great mount of time discussing everything with Antonio Levy, who is fast and full of imaginations. The life of PhD research has been easier with him. I also want to thank Dr. Ursula Wurstbauer, Dr. Trevor David Nathaniel Rhone, Dr. Jun Yan, Dr. Rui He and Dr. Cyrus Farohk Hirjibehedin. They have been very successful researchers from this group. I enjoyed the interactions with them and I am constantly helped by the treasure they left in the lab.

I would also to thank my friends in Columbia such as Dr. Datong Zhang, Luchang Jin, Xiang Meng, Wencan Jin, Zhaoyi Li, Dr. Ying Wang, Dr. Chenyang Shi, Dr. Olgun Adak, Austin Cheng, Dr. Lei Wang, Dr. Yilei Li, Dr. Yu Gu, Dr. Ningyao Zhang, Dr. Chenxi Guo, Dr. Qian Peng, Dr. Xiao Xiao, Dr. Jianglei Yu, Dr. Hantao Yin, Dr. Daiqian Zhang, Haixing Li, Peijie Ong, Chia-Hao Liu, Tingting Wang, Ziyuan Bai, Qiao Fu, and surely many more. The life at Columbia would not be so enjoyable without them.

I would like to thank my families. My father and mother are always very supportive on whatever choices I make and their support is the strength that keeps me

going through all the difficulties.

In the end, I would like to thank my girlfriend, now my wife, Yangyang Song. All the time we spend together since 2008 in Peking University constitutes a wonderful memory. Her love makes me motivated to face whatever challenges I meet. My life is full of joy and happiness with her.

# Chapter 1

# Introduction

At the beginning of 21st century, graphene, a single layer of carbon atoms arranged in a honeycomb lattice, has attracted extraordinary interest due to its special electronic, optical, and mechanical properties[1–3]. While electronic band structures of graphite/graphene have been studied for many years[4–6], graphene was thought to be thermodynamically unstable in a free state[7, 8]. The initial experimental exfoliated isolations of graphene[9–11] created enormous interest in studies of graphene and related materials.

Quantum Hall effect experiments on exfoliated graphene soon demonstrated that charge carrier in graphene has a linear energy-momentum relation, which can be described by massless Dirac equations[1, 2]. Fig. 1.1 demonstrates the honeycomb lattice underlying graphene and its corresponding first Brillouin zone. The gap of graphene vanishes near the K and K' points of the Brillouin zone, forming the so-called Dirac cones. The energies near the Dirac cones can be described as $E = \hbar v_F k$, where $\hbar$ is the reduced Planck constant, k is the quasiparticle momentum and $v_F$ is the Fermi velocity.

The appearance of massless Dirac fermions (MDFs) around Dirac cones is a direct result of the symmetry of the honeycomb lattice. Thus artificial honeycomb

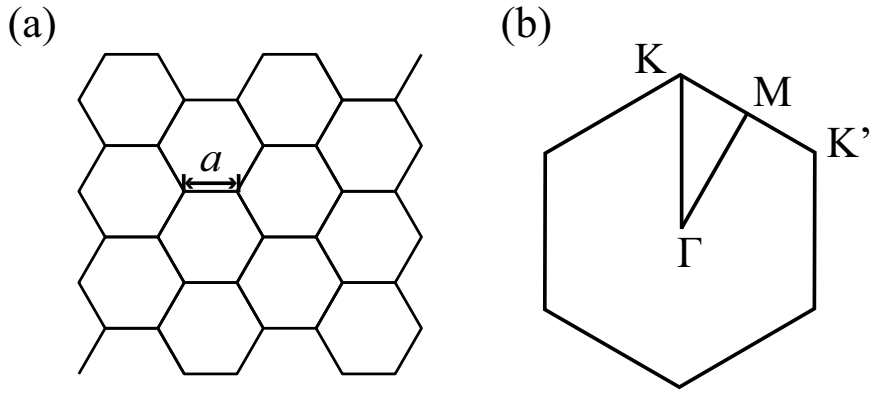


Figure 1.1: (a) A honeycomb lattice representing graphene. $a$ is the distance between two nearest atoms. (b) First Brillouin zone of graphene. High symmetry points of Brillouin zone are labeled.

lattices, also known as "artificial graphene" (AG), can provide a tunable platform for creating and manipulating MDFs and their topological and correlated phases in semiconductors[12, 13]. Similar considerations apply to molecules on cold surfaces , cold atoms in optical lattices and photonic crystals[14].

AG systems allow access to quantum regimes which are not accessible in natural graphene. For example, tuning the interplay of lattice constant and inter-site coupling can continuously change the system from weakly coupled regime to strongly coupled regime. It is also feasible to design AG lattices to probe the Hofstadter's butterfly[15], involving the interplay of the lattice constant and the magnetic length, which requires unachievable large magnetic field in natural graphene. AG band structures can be engineered to have features that are not possible in natural graphene. For example a band gap at Dirac cones can be opened up by breaking the symmetry of two neighboring sites. Another interesting example is the creation of tunable topological insulators with the AG lattices imprinted on semiconductors with spin-orbit coupling significantly stronger than in graphene[16].

Remarkable AG physics has been explored in experiment or theory for molecules on metallic surfaces[17], cold atoms in optical lattices[18–20] and photonic crystals[21–25]. It will be very promising to realize AG in semiconductor systems because advances in semiconductor fabrication methods will provide the means for a highly adjustable, scalable system which can be integrated with other electronic components.

Band engineering of semiconductors was proposed by Esaki and Tsu in 1970 by introducing a modulating potential in one direction[26]. Following this work, nanopatterned semiconductor QW with periodic lattice, also called lateral superlattice, has been intensively studied in the late 1980s and 1990s [27–34]. However it is much harder to create small periods (for instance 10 nm as proposed in Ref [26]) for lateral lattice than that in the growth direction of the heterostructure. With lateral

lattice periods of ≥300 nm[27, 28, 31–34], the band structures induced by the periodic external potential, also called minibands, will be too small to be resolved in experiments.

Current state of the art molecular beam epitaxy (MBE) technology can grow semiconductor QW with very high precision and nearly defect free to host ultrahigh mobility charge carriers [35]. Advances in fabrication technologies demonstrated in this thesis can greatly reduce the lattice period and thus enable us to enter the regime to probe electron minibands of lateral lattices. A particular interest on nano-patterned GaAs QW with honeycomb lattices arose recently in the pursuit of AG physics[12–14, 36–40]. Park et al. [12] present the first theoretical analysis for AG physics in nano-patterned semiconductors based on nearly free electron perturbation theory while Gibertini et al. [13] use a plane-wave method to calculate AG bands with photoluminescence spectra showing the impact of the honeycomb lattice. Nadvornik et al. [39] study nano-patterned antidot system with triangular lattice. However those prior realizations of AG lattices on nano-patterned semiconductor QWs [13, 36, 37, 39] did not find direct evidence of AG electron band structures or Dirac cones because of the relatively large lattice periods (≥130 nm). In those systems the minibands are not well-defined due to the broadening effects from finite temperature and disorder.

In order to observe AG physics in nano-patterned semiconductor QW, it is essential to increase the energy range of the linear dispersion near the Dirac cones by reducing the AG lattice period and advancing the spatial uniformity. Since the energy scale is proportional to $1/a^2$, where $a$ is the lattice constant as shown in Fig. 1.1, reducing the lattice constant by a fractor of three (for example from 120 nm to 40 nm) will increase the energy scale to an order of magnitude. This provides strong motivation to pursue artificial honeycomb lattices with small periods. An example of calculated AG electron bands is shown in Fig. 1.2. The linear energy-momentum dispersion is highlighted by a red circle.

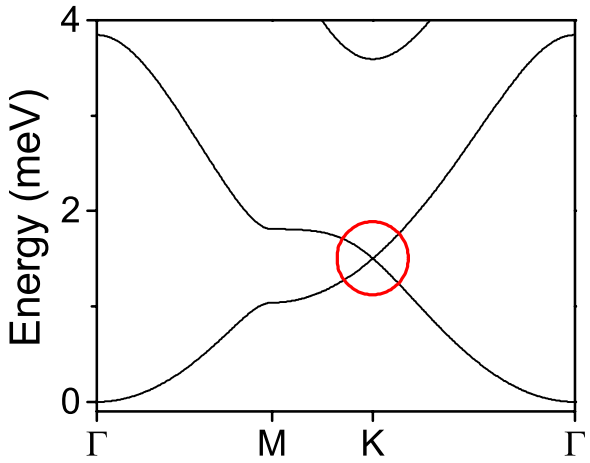


Figure 1.2: Calculated AG bands with $a = 40$ nm for nano-patterned GaAs QWs (replicate of Fig. 5.3(b)). The Dirac cone is highlighted by a red circle. The detail of this calculation can be found in Chapter 5.

In this thesis, I report advances in the studies of AG lattices in nano-patterned GaAs QWs. With current state of the art fabrication technologies, we are able to achieve lattice constants as small as 40 nm. Resonant inelastic light scattering (RILS) is used to probe the electron states in the AG systems. Transitions involving different AG bands are observed in RILS spectra. Those transitions are successfully interpreted within a theoretical model, in which joint density of states (JDOS) between different bands are calculated. Transitions around the Dirac cones are resonantly enhanced by changing the incident photon energies, and with these transitions we can demonstrate experimental evidences related to the Dirac cones.

The last part of this thesis describes the graphene growth on sapphire substrate by MBE with a solid carbon source as another approach to extent graphene physics to industrial applications. Single and bi-layer of graphene are achieved on sapphire substrate at high temperature (about 1300 ℃). The appearances of etch pits suggest a strong interplay between carbon deposition and its removal, which should be helpful to optimize the growth of graphene layers.

This dissertation is organized as follows:

Chapter 2 gives a brief introduction to key properties of a two dimensional (2D) electron gas that are relevant to our studies. I discuss the realizations of such systems by MBE on semiconductor heterostructures as well as the basic physics of 2D electron gas. This chapter also describes the formation of subbands due to the confinement of the GaAs QWs and relevant transitions between them. Density of states (DOS) and joint density of states (JDOS) for different band structures are also calculated as they will be used to understand the transitions relevant to AG band structures.

In Chapter 3, I discuss optical characterizations of GaAs QW nanostructures as well as experimental considerations such as the optical setup. RILS is a powerful tool to study those excitations in dilute 2D electron systems. In this thesis RILS is used as a main tool to probe electron states in the AG lattices. The mechanism of RILS as

well as polarization selection rules are discussed for both 3D and 2D electron systems. Optical emission is used to estimate the Fermi energy of electrons in the QW. The lineshape of optical emission spectra can also provide insight to the electronic bands associated with optical transitions. Those optical characterization methods together will be very powerful to study our AG systems.

In Chapter 4, I discuss the methods used in fabrication of small period AG lattices in nano-patterned GaAs QWs. AG lattices with lattice constant as low as 40 nm are achieved through optimized electron beam (E-beam) lithography and inductively coupled plasma (ICP) reactive-ion etching (RIE): E-beam lithography is used to define an etch mask with honeycomb geometry on the surface of the QW sample and the ICP-RIE is used to transfer the pattern into the QW sample and create the AG lattice. The impact of different fabrication parameters on the AG lattices are discussed and the optimized fabrication procedure is capable to produce high quality AG lattices with excellent spatial uniformity.

The calculation of AG electron bands for nano-patterned GaAs QWs is discussed in Chapter 5. A simple theoretical model, called periodic muffin-tin potential, is employed to calculate the band structures of AG lattices. The parameter space for creating well-developed Dirac cones is analyzed and the energy range of linear dispersion is also discussed here. DOS and JDOS between different AG bands are calculated, and they provide the framework to interpret transitions involving AG bands.

In Chapter 6, I discuss the spectra of AG patterns and provide interpretations of these spectra. Optical emission spectra are used to estimate the Fermi energy and modulation potential. Comparisons between weakly and strongly modulated AG lattices provide insight on the impacts of the modulation potential. RILS of intersubband transitions reveal intriguing satellite peaks, which are interpreted as combined intersubband transitions with simultaneous change of QW subband state

and the AG band. Low-lying excitation peaks in RILS spectra, interpreted as direct transitions between AG bands without change in QW subband, provide a more direct insight on the AG band structures. These transitions exhibit a remarkable agreement with the predicted JDOS based on the band structure calculations for the honeycomb topology. Different features in the RILS spectra are assigned to transitions of different reciprocal space, where they can be resonantly enhanced at different incident photon energies. For transitions around the K and K' point, the spectral lineshape of RILS is interpreted by calculated JDOS around the Dirac cones, where a constant slope indicates the existence of Dirac cones. The formation of AG bands in nano-patterned semiconductors provide a great tunable platform for studies of phenomenons related to MDFs.

In Chapter 7, I discuss graphene growth on sapphire substrates by MBE. Growth of nanocrystalline single- and bi-layer graphene is achieved on a sapphire (0001) substrate by van der Waals MBE with a solid carbon source. Raman spectroscopy reveals that the fabrication of single layer, bilayer or multilayer graphene crucially depends on MBE growth conditions. Etch pits on the sapphire substrate indicate a competition between carbon deposition and a carbon removal mechanism. Tuning the interplay between carbon deposition and its removal, by varying the incident carbon flux and substrate temperature, should enable the growth of high quality graphene layers on large area sapphire substrates.

In Chapter 8, I discuss possible future works. While we have reached significant milestones that demonstrate the formation of AG band structures experimentally, I discuss three approaches to further advance these realms of research. At small lattice constants such as $a = 40$ nm, fabricating etch masks for quantum dots with large radius is essential to obtain well-developed Dirac cones. Triangular antidot lattices can create similar linear energy-momentum dispersion as honeycomb lattice dots, but with larger inter-dot distance than honeycomb lattice. It is especially useful

to use triangular antidot lattices to further increase the energy scale of electronic minibands. Tuning the Fermi level of AG lattices through gating is important to study the Dirac physics. Thus I present sample designs for gating for both honeycomb lattices and triangular antidot lattice. Lots of novel physics should be expected from nano-patterned semiconductors.

# Chapter 2

# 2D Electron Gas in GaAs Quantum Well

## 2.1 GaAs Quantum Well

When electron motion is restricted in one direction and is free on the other two directions, a two dimensional (2D) electron gas is formed. The 2D electron gas is a great platform to study novel phenomenon in physics such as the quantum Hall effect (QHE) and the fractional quantum Hall effect (FQH)[41–43]. To confine electrons in a 2D plane, we need potential barrier on both sides of the structure. A quantum well (QW) is such a system that electrons are confined in a 2D plane by engineering the band structures.

The 2D electron system used in this thesis occurs in GaAs/$Al_xGa_{1-x}As$ QWs. Due to the small lattice mismatch between GaAs and $Al_xGa_{1-x}As$, GaAs/$Al_xGa_{1-x}As$ heterostructures can be grown by molecular beam epitaxy (MBE) with very little strain and thus have nearly defect free interfaces. This technique can produce 2D systems with ultra high electron mobility [35]. The difference of band gaps between GaAs and $Al_xGa_{1-x}As$ is engineered to create various band profiles that confine charge

carriers. The charge carrier type is determined by the dopant type. In this thesis we limit most of discussions to n-doped QWs since our QW samples are n-doped. The band gap of $Al_xGa_{1-x}As$ depends on Al concentration $x$ and temperature $T$. For small x ($< 0.4$), $Al_xGa_{1-x}As$ has a direct band gap approximately at low temperature described by [44]:

$$E_g(eV) = 1.519 + 1.155x + 0.37x^2 - 5.41 \times 10^{-4}\frac{T^2}{T + 204} \tag{2.1}$$

This formula can be used to estimate the potential barrier height of GaAs QWs. A typical layout of the n-doped QW sample used for the AG patterns is shown in Fig. 2.1. An initial GaAs buffer layer($\sim$ 500 nm thick) and a superlattice of a few hundred ($\sim$ 330) periods of GaAs and AlGaAs (typically 3 nm and 10 nm thick respectively) is grown before the QW layers to release the strain and improve sample quality. The active region, the 25 nm GaAs layer denoted by the red region, is sandwiched between two AlGaAs layers. The top AlGaAs layers are doped by one atomic Si layer at a distance $d = 30$ nm from the QW. A capping GaAs layer of 10 nm is grown on the top to prevent reactions between the AlGaAs layers and the environment. Electrons from the doping layer can migrate to the low energy states in the QW, denoted by the green region of conduction band on the left panel of Fig. 2.1. This $\delta$-doping procedure, dopants concentrated on one atomic thin layer with a distance from the QW, is known as modulation doping and provides a clean QW without ionized dopants. This method can produce 2D electron gas with very high mobility. Furthermore the doping layer in the AlGaAs barrier is usually over-doped so electrons in the doping layer can screen the charge in the randomly distributed Si ions. This will reduce the scattering of electrons by remote charges and increase the mobility.

After nano-patterning, the AlGaAs layers in the QWs will be unavoidably exposed to the air and react with oxygen. To minimize such oxidization of AlGaAs, we choose

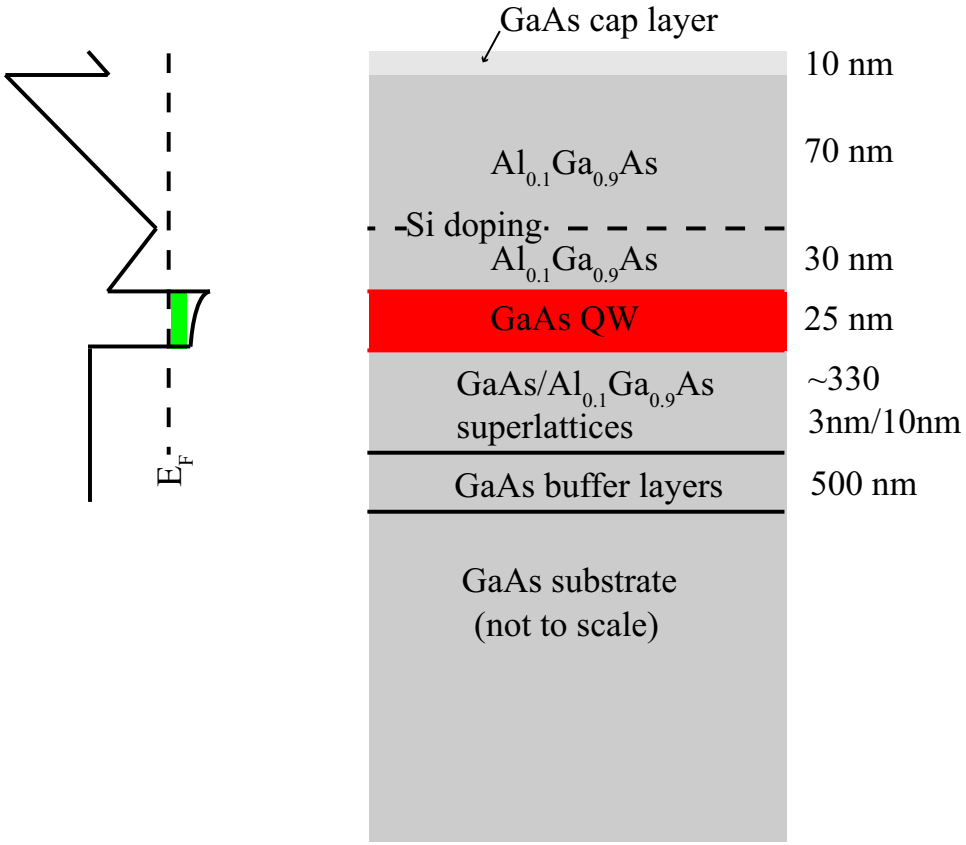


Figure 2.1: Layout of one-side modulation doped $Al_{0.1}Ga_{0.9}As$/GaAs QW typically used in this thesis (not to scale). It has a 25 nm wide QW (in red) with a setback (the distance between the QW and the doping layer) of 30 nm, followed by 70 nm $Al_{0.1}Ga_{0.9}As$ layer and 10 nm GaAs cap layer. The as-grown carrier density is $1.8 \times 10^{11}$ cm$^{-2}$ with a mobility of $3.2 \times 10^6$ cm$^2$/(V·s) at 4 K. Left panel is the corresponding conduction band diagram. The energy range of electron gas is denoted in green. The Fermi level is indicated by the dashed line.

the low Al concentration (10%) in our samples. This ensures that the samples can still maintain good quality after being nano-patterned with AG lattices.

The bandgap difference between GaAs and $Al_{0.1}Ga_{0.9}As$ is 0.12 eV by Eq. 2.1, and this energy difference splits into conduction band and valence band. A rule of thumb about the split between conduction band and valence band is that 67% of the bandgap difference will go into conduction band and the other 33% will go into valence band [45]. So the potential barrier height for electron is roughly 0.08 eV in GaAs/$Al_{0.1}Ga_{0.9}As$ QW, and this can be used to calculate the energy levels due to the confinement of the QW.

## 2.2 Electron Gas in GaAs QW

### 2.2.1 Electronic Band Structures of GaAs QW

In this subsection, I discuss the basic properties of electrons in the GaAs QW. The electrons in the GaAs QW can be described by an envelope wavefunction approximation[46], in which the wavefunction $\psi(\vec{r})$ for electrons is written as:

$$\psi_{j,\vec{q}}(\vec{r}) = u_j(\vec{r})e^{i\vec{q}\cdot\vec{r}}\chi_j(z) \tag{2.2}$$

where $\vec{q}$ denotes wave vector in the $\hat{x}$-$\hat{y}$ plane and $j$ is the index of states confined in $\hat{z}$ direction. $\chi_j(z)$ is the wavefunction related to confinement in $\hat{z}$ direction. $u_j(\vec{r})$ is the periodic component in the Bloch function and varies fast in space $u_j(\vec{r}) = u_j(\vec{r}+\vec{R})$ for any Bravais lattice vector $\vec{R}$. Under this approximation, the energy of electrons $E_{j,\vec{q}}$ in the quantum well can be described as:

$$E_{j,\vec{q}} = E_j + \frac{\hbar^2\vec{q}^2}{2m^*} \tag{2.3}$$

where $m^*$ is the effective mass of the electron and $E_j$ is the eigen energy related to states confined in the $\hat{z}$ direction, determined by

$$(-\frac{\hbar^2}{2m^*}\nabla^2 + V(z))\chi_j(z) = E_j\chi_j(z) \tag{2.4}$$

with boundary conditions of continuity in $\chi_j(z)$ and $\frac{\partial}{m^*\partial z}\chi_j(z)$. Note that the effective mass $m^*$ is different across the boundary and $V(z)$ is the potential in z direction. $m^*$ can be approximated as independent of $q$ when we restrict $q$ to a small K space region around the center ($\Gamma$ point) of the Brillouin zone. A typical value for $m^*$ in GaAs is $0.067m_0$, where $m_0$ is the rest mass of free electron. The range of k space that we are interested in is $0 \leq q \leq k_F$, where $k_F$ is the wave-vector of electrons in the Fermi level. In this work a typical 2D electron gas (2DEG) has density $n = 1.8 \times 10^{11}$ cm$^{-2}$, its Fermi wave-vector can be calculated as $k_F = (2\pi n)^{1/2} \approx 10^6$ cm$^{-1}$. It is much smaller than the Brillouin zone size of GaAs which is about $2\pi/a \approx 10^8$ cm$^{-1}$ and $a = 5.6$ Å is the lattice constant of GaAs. As $k_F \ll 10^8$ cm$^{-1}$, it is reasonable to assume a constant effective mass for electrons in the GaAs QWs used in this thesis.

Using the simplest model, we can consider the confinement of the QW to be an infinitely deep square well with width of $L$, as shown in Fig. 2.2(a), in z direction described by:

$$V(z) = \begin{cases} 0 & 0 < z < L \\ \infty & z < 0 \quad \text{or} \quad z > L \end{cases} \tag{2.5}$$

A simple analytic solution can be obtained as:

$$E_j = \frac{\hbar^2}{2m^*}(\frac{j\pi}{L})^2 \qquad (j = 1, 2, 3...) \tag{2.6}$$

$$\chi_j(z) = \sqrt{\frac{2}{L}}\sin(\frac{j\pi}{L}z) \quad \text{for} \quad 0 < z < L \qquad (j = 1, 2, 3...) \tag{2.7}$$

In Eq. 2.6 and Eq. 2.7, $j$ labels different bands counting from lowest band to higher ones. We usually call these bands in the QW as different subbands. In this thesis, only the first two subbands are discussed. The electronic bands (subbands) for different

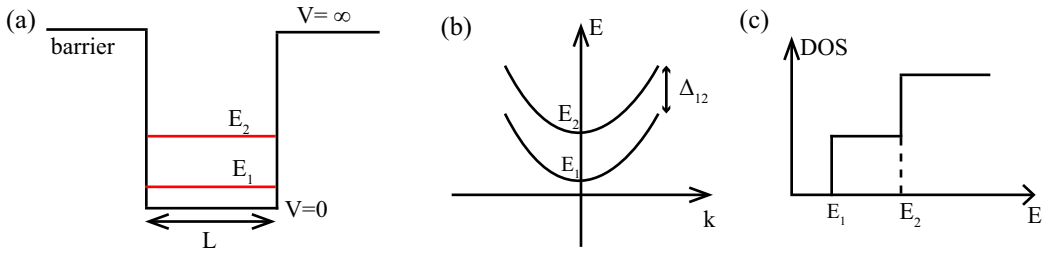


Figure 2.2: Infinite deep square well confinement for electrons. (a)Potential profile of such confinement with first two subbands indicated by red horizontal line. The corresponding energies for these two bands, $E_1$ and $E_2$, are given by Eq. 2.6. (b) Energy dispersion of the first two subbands. The energy separation for these two bands is $\Delta_{12} = E_2 - E_1$. (c) DOS of 2D electron gas in the QW. For each subband, its DOS is a constant given by Eq. 2.11, so the total DOS has a stair-like shape which jumps at $E_j$.

QW confined states are shifted by $E_j$, as shown in Fig. 2.2(b), and its DOS has a stair-like shape, shown in Fig. 2.2(c), which will be explained later in this chapter.

For a more realistic situation, the barrier for the QW has finite depth. In fact it is not hard to solve the finite height square well problem. For a square well with finite height of $V_o$ and a constant effective mass $m^*$ across the QW, its eigen energies of bonding states are described by:

$$\tan(\frac{\sqrt{2m^*E}L}{2\hbar}) = \sqrt{\frac{V_o}{E} - 1} \tag{2.8}$$

$$-\cot(\frac{\sqrt{2m^*E}L}{2\hbar}) = \sqrt{\frac{V_o}{E} - 1} \tag{2.9}$$

The solutions from the combined Eq. 2.8 and Eq. 2.9 give the energies of the states bond in the QW. To make the right hand side of Eq. 2.8 and Eq. 2.9 real, the obvious requirement for a bond state is $E < V_o$. The numerical results can be obtained given the value of $V_o$, with the help of a graphic plot as shown in Fig. 2.3. One comment about the number of bonded states is that there is at least one bonded state no matter how small the barrier is. A more detailed discussion of these solutions can be found in Ref.[47].

A more accurate calculation needs to involve self-consistently the Coulomb interaction. In the one-side modulation doped QW used in this thesis, the potential barrier is asymmetric and is also bent due to spacial distribution of electrons. The actual shape of the conduction band and eigenenergies can be numerically calculated using a self-consistent approach with combined Schrödinger equation and Poisson's equation. A typical conduction band using self-consistent calculation[48] is shown in Fig. 2.4.

Excitations between different subbands of the QW, called intersubband excitations, can be studied by RILS to estimate the energy differences between different

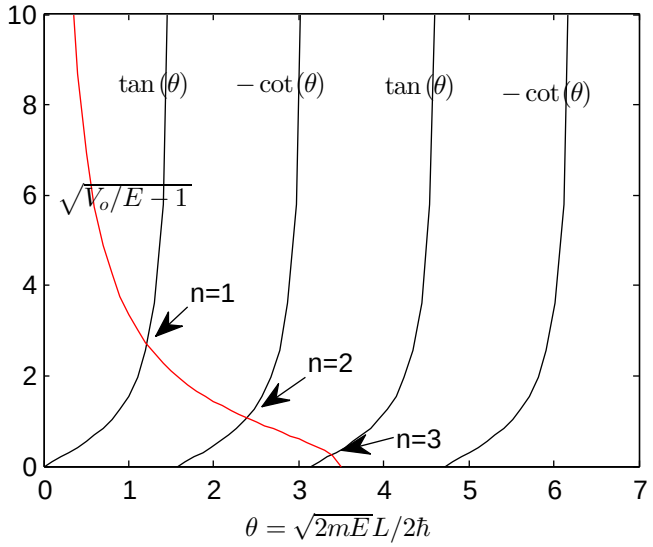


Figure 2.3: Graph showing numerical solutions of Eq. 2.8 and 2.9 indicated by arrows. Dimensionless number $\frac{\sqrt{2m^*E}L}{2\hbar}$ is denoted as $\theta$, the cross points between black line and red line are solutions of Eq. 2.8 and 2.9. In this simulation, I use parameters similar to the QW samples used in this thesis, $\frac{\sqrt{2m^*V_o}L}{2\hbar} = 3.5$, this figure shows that the QW has three bonded states.

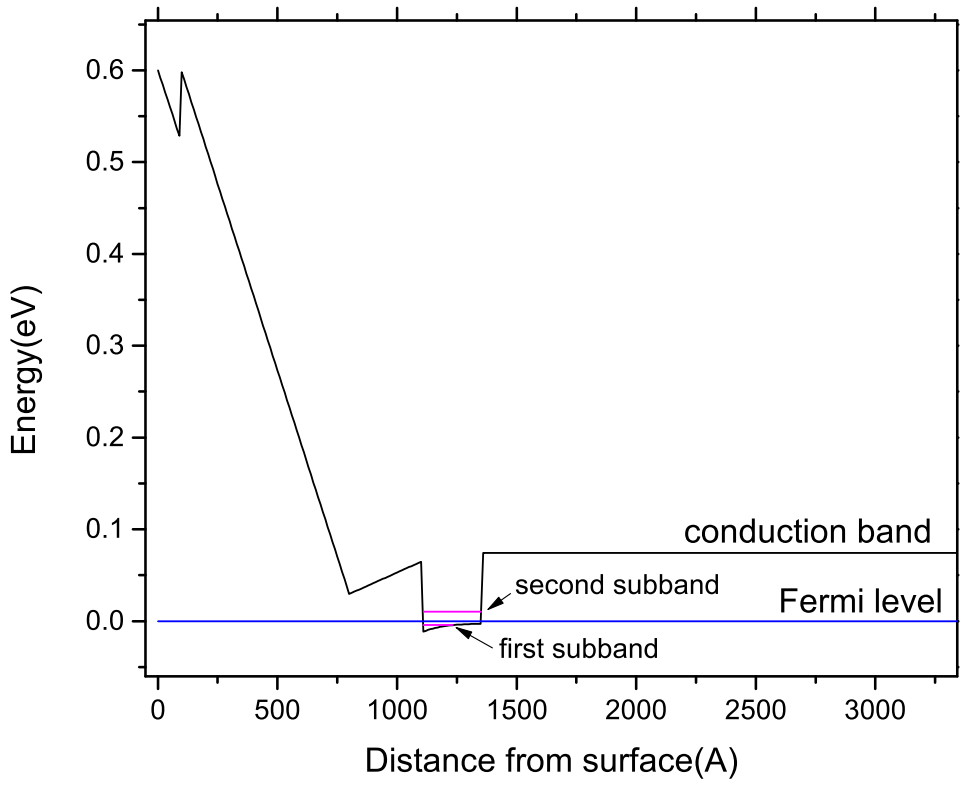


Figure 2.4: Conduction band of a 25nm wide one-side modulation doped QW from a self-consistent calculation. Fermi level and the first two subbands are labeled.

subbands, such as $\Delta_{12}$ in Fig. 2.2(b), and many-body effect related to spin or charge density. The mechanism of intersubband excitations will be discussed in Chapter 3.

### 2.2.2 Density of States and Joint Density of States

In this subsection I will discuss density of states (DOS) and joint density of states (JDOS) of electrons in the GaAs QWs and other related systems.

Within the effective mass approximation, the 2D electron gas in our QW has a constant DOS. Assuming electrons are moving in a large rectangle plane with length $L_x$ and $L_y$ in its $x$ and $y$ direction, the number of electron states $dN$ in K space per area is:

$$dN = 2\frac{L_x}{2\pi}\frac{L_y}{2\pi}d^2k/(L_xL_y) = \frac{d^2k}{2\pi^2} = \frac{kdk}{\pi} \tag{2.10}$$

In Eq. 2.10, the factor 2 comes from counting two spins in one k state. The DOS of 2D electron gas is:

$$DOS_{2D} = \frac{dN}{dE} = \frac{k}{\pi}\frac{1}{dE/dk} = \frac{k}{\pi}\frac{m^*}{\hbar^2 k} = \frac{m^*}{\pi\hbar^2} \tag{2.11}$$

This constant DOS comes from its dimensionality (2D in this case) and parabolic shape of the energy-momentum dispersion. When the dimension is not 2D or the dispersion is not parabolic, the DOS will not necessarily remain constant. Comparisons of DOS for different dimensions and energy-momentum dispersions are illustrated in Fig. 2.5. In 1D and 3D cases with parabolic energy-momentum dispersions, the DOS is not constant, quite different from the 2D case. On the other hand, for 2D electrons with non-parabolic energy-momentum dispersion , such as electrons in graphene, DOS is not constant either.

Another closely related concept is JDOS. When we consider transitions between two bands $E_1(k)$ and $E_2(k)$, the intensity $I(E)$ at transition energy $E$ is proportional to the JDOS between these two bands,

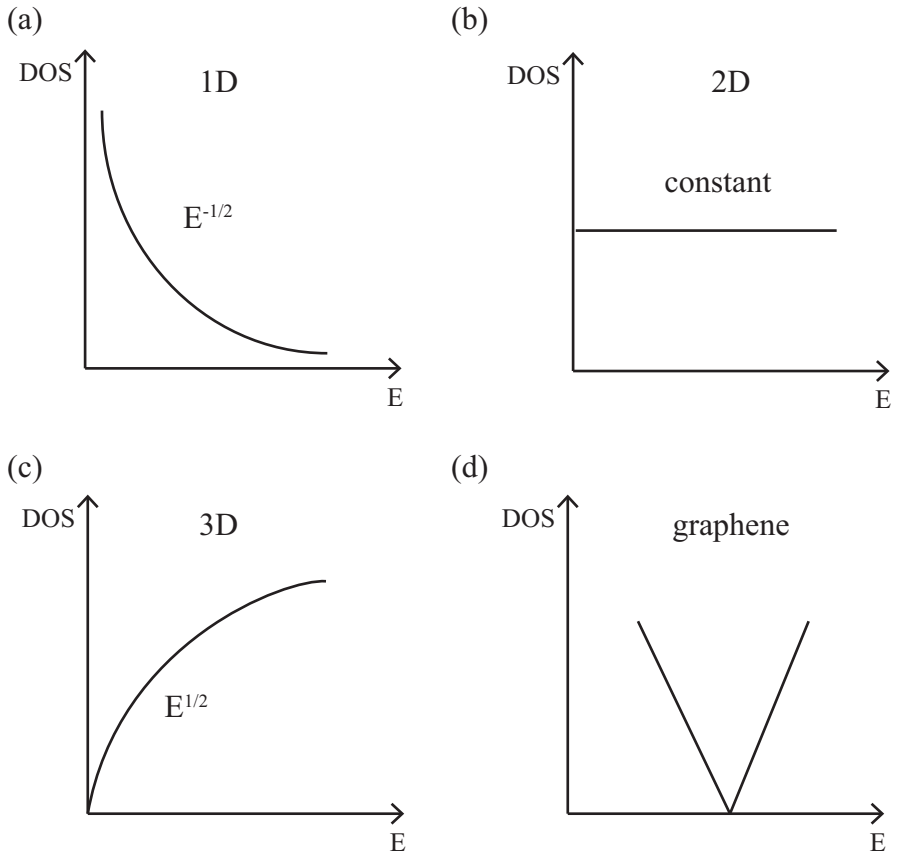


Figure 2.5: DOS for electrons in systems with different dimensions and energy-momentum dispersions. Electrons confined in (a)1D, (b)2D and (c)3D space with parabolic dispersion have different DOS. Electrons in graphene are confined in 2D space but have linear energy-momentum dispersion, thus the DOS has constant slope and vanishes around the Dirac cones as shown in (d).

$$I(E) \propto ||M||^2 \times JDOS(E) \tag{2.12}$$

where $M$ is the relevant matrix element. In 2D case $JDOS(E)$ is defined as:

$$JDOS(E) = \frac{1}{2\pi^2}\delta(E_2(k) - E_1(k) - E)d^2k \tag{2.13}$$

where $\delta$ is the delta function which satisfies $\int \delta(x)dx = 1$. As an example, consider the JDOS between the valence band $E_1(k)$ and conduction band $E_2(k)$ of GaAs QW:

$$E_1(k) = -\frac{\hbar^2 k^2}{2m_h} - E_0 \tag{2.14}$$

$$E_2(k) = \frac{\hbar^2 k^2}{2m_e} \tag{2.15}$$

$$E(k) = E_2(k) - E_1(k) = E_0 + \frac{\hbar^2 k^2}{2m_h} + \frac{\hbar^2 k^2}{2m_e} \tag{2.16}$$

where $m_e$ and $m_h$ denote the effective mass of electron and hole in GaAs. Following similar procedure as Eq. 2.11, $JDOS(E)$ can be calculated:

$$JDOS(E) = \frac{k}{\pi}\frac{1}{dE/dk} = \frac{1}{\pi\hbar^2}\frac{m_e m_h}{m_e + m_h} \tag{2.17}$$

Again the constant JDOS is caused by combined effect of dimensionality (2D) and parabolic dispersion of the energy difference between the two bands.

As we will encounter transitions involving the Dirac cones in later chapter (Chapter 6), it would be very interesting to derive the JDOS between a linear dispersed band and a parabolic band as shown in Fig. 2.6. The energy dispersion of two bands can be described as:

$$E_1(k) = \hbar v_F k \tag{2.18}$$

$$E_2(k) = E_{LC} + \frac{\hbar^2 k^2}{2m^*} \tag{2.19}$$

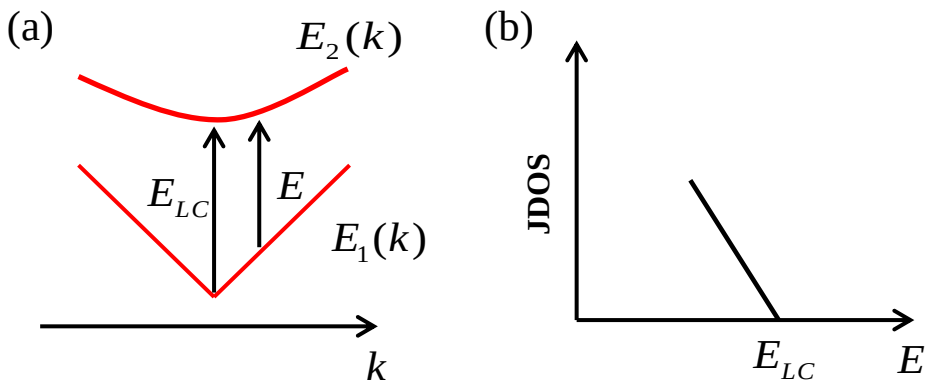


Figure 2.6: JDOS involving the Dirac cone. (a) Electron bands of a Dirac cone and a parabolic band showing transitions between them. (b) JDOS around Dirac cone showing vanishing magnitude with a constant slope.

where $v_F$ is the Fermi velocity, $E_{LC}$ is the energy difference between the two bands at $k = 0$, and $m^*$ is the effective mass of parabolic band. Transition energy $E(k)$ and $JDOS(E)$ can be derived similarly as Eq. 2.17,

$$E(k) = E_2(k) - E_1(k) = E_{LC} + \frac{\hbar^2 k^2}{2m^*} - \hbar v_F k \tag{2.20}$$

$$\begin{aligned} JDOS(E) &= \frac{k}{\pi}\frac{1}{dE/dk} \\ &= \frac{m^*}{\pi\hbar^2}\frac{1}{\frac{m^* v_F}{\hbar k} - 1} \\ &= \frac{m^*}{\pi\hbar^2}((1 - \frac{E_{LC} - E}{m^* v_F^2/2})^{-\frac{1}{2}} - 1) \\ &\to \frac{E_{LC} - E}{\pi\hbar^2 v_F^2}|_{E \to E_{LC}} \end{aligned} \tag{2.21}$$

A unique feature of this JDOS is the constant slope for transitions around Dirac point as shown in Fig. 2.6(b). This is remarkably different from the constant JDOS in the case of two parabolic bands. The importance of JDOS will be emphasized again when the novel peaks found in RILS can be well explained in term of JDOS in Chapter 6.

# Chapter 3

# Optical Characterizations of GaAs Nanostructures

## 3.1 Introduction

Optical spectroscopy is very useful in studying electron states for a wide variety of condensed matter systems. In this chapter I will discuss two optical characterization methods that are employed in our studies of AG systems: resonant inelastic light scattering (RILS) and optical emission. This chapter provides a conceptual framework to understand the experimental data.

I begin with the discussion of experimental setup in Section 3.2. The experimental requirements for the studies of the AG patterns such as low temperature, tunable laser, and high resolution spectrometer, are described here.

RILS is a powerful tool to study weak excitations utilizing the resonant enhancement. I discuss the resonance mechanism of RILS as well as selection rules that are applicable in 2DEG in Section 3.3. The mechanisms of intrasubband and intersubband excitations are also discussed.

In Section 3.4, I discuss the mechanism of optical emission as well as its appli-

cations. Optical emission can provide insights into the Fermi energy of the 2DEG systems. Two examples are given for the as-grown samples and the AG nano-patterns.

## 3.2 Experimental Considerations

Most of the AG patterns were fabricated on a high-quality, single-side modulation-doped GaAs/AlGaAs QW (sample L06-27-14 or similar) with electron density $n = 1.8 \times 10^{11}$ cm$^{-2}$ and mobility $\mu = 3.2 \times 10^{6}$ cm$^2$/Vs at 4 K. Details of the sample layout can be found in Section 2.1. The samples were mounted in an optical cryostat operated at temperatures in the range of 2-10 K. They were attached to a cold copper finger via rubber cement and were in direct contact with helium gas or liquid. Only a portion of the samples was attached to the cold finger and the other portion with AG nano-patterns was in suspended state to minimize the strain caused by contraction during the cooling process.

The layout of the optical experimental setup is schematically shown in Fig. 3.1(a). A back-scattering configuration is used for both RILS and optical emission as shown in Fig. 3.1(b). $\theta$ denotes the angle between the incident/scattered photon and the normal to the sample surface. It is easy to show that the transfered in-plan wavevector for the 2DEG is:

$$k = 2k_L sin(\theta) \tag{3.1}$$

where $k_L = \omega_L/c$ is the wavevector of incident photon in vacuum. In the studies of the AG lattices, no in-plane momentum is needed to be transfered to the 2DEG, so the incident laser beam is almost perpendicular to the sample, and a small angular deviation (about 6°) from perpendicular can be very useful to reduce stray light in the low-lying RILS experiments.

A tunable Ti:sapphire laser provides a sharp ($< 30$ $\mu$eV wide) and continuously

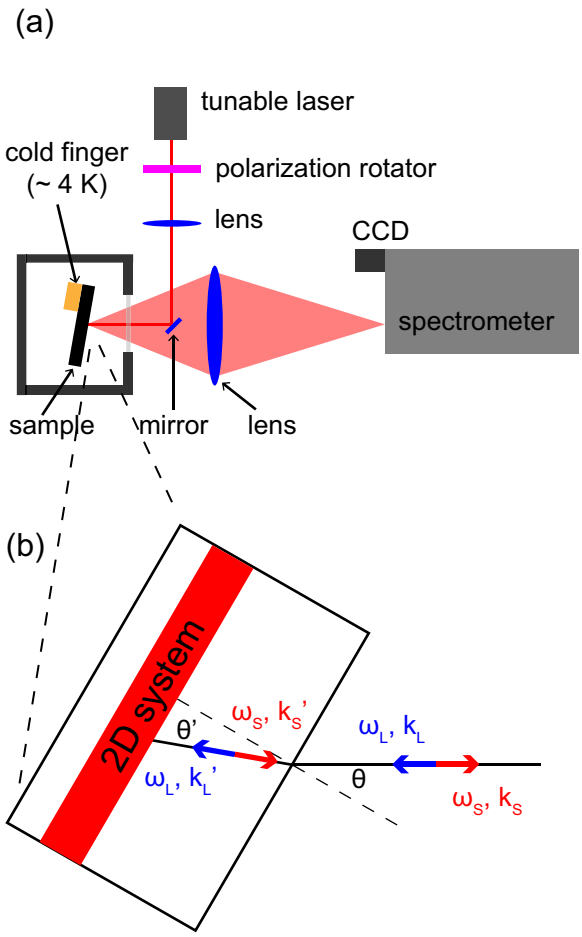


Figure 3.1: Schematic of optical experiment set-up for the studies of the 2DEG systems. (a) Schematic of optical spectroscopy including laser, cryostat, spectrometer and CCD. (b) Back-scattering geometry used in RILS and optical emission. Incident photon and scattered photon in the air are label by $\omega_L, k_L$ and $\omega_S, k_S$.

tunable excitation source. It is optically pumped by an argon ion laser at 488 nm and has emission range (740 nm - 850 nm) covering the fundamental optical gap of GaAs QW (800 nm - 820 nm). The emission of Ti:sapphire laser is linearly polarized and is rotated by a polarization rotator to be either parallel (polarized) or perpendicular (depolarized) to the scattered light. The scattered light is focused on to AG patterns by a spherical lens (with focal length of 20 cm) to a spot of around 100 $\mu$m diameter. The typical power for RILS is 1 mW to avoid heating of electron gas at 4 K. For optical emission, 0.1 $\mu$W - 1 mW is employed.

The scattered light is collected by one lens (with focal length of 8.5 cm) to be focused onto the entrance slits of spectrometer. Light is collected from a finite solid angle set by the cryostat's F# (about 2). Focal lengths and lens sizes are determined through matching the F#s of the cryostat, collection optics and spectrometer; and setting the desired magnification of the collection path. The finite solid angle of the collection defines an uncertainty in the wavevector transferred to the 2D system.

The light scattered from the sample is dispersed by a 0.85 m double grating spectrometer (Spex 1404) which has holographic master gratings that minimize the stray light. Then it is collected using a liquid nitrogen cooled charged coupled device (CCD) with 2048×512 pixels of 13.5 $\mu$m pixel size (Spectrum One from Horiba). The combined resolution of the system with entrance slits width of 30 $\mu$m is 16 $\mu$eV. The response of the spectrometer is linearly polarized, so that spectra can be taken with linear polarization of incident photons parallel or perpendicular to the scattered photons' polarization.

## 3.3 Resonant Inelastic Light Scattering

### 3.3.1 Introduction

Resonant inelastic light scattering (RILS) is a useful tool to directly probe a variety of fundamental properties of condensed matter systems. The discovery of Raman scattering by Sir Chandrasekhara Venkata Raman [49] made light scattering popular and widely used. The term "Raman scattering" traditionally means the inelastic light scattering by optical phonon in crystal or by molecular vibration [50]. In this thesis, I focus on inelastic light scattering by excitations of electrons in the 2DEG system in AlGaAs/GaAs heterostructures and use inelastic light scattering and Raman scattering interchangeably to refer such applications. The history and basic theory of light scattering can be found in Ref.[51].

Inelastic light scattering by electronic excitations involves several steps: the annihilation of the incoming photon with frequency $\omega_L$, wavevector $\vec{k}_L$ and polarization $\hat{e}_L$; the creation or annihilation of an excitation with frequency $\omega$ and wavevector $\vec{q}$; and the creation of a scattered photon with frequency $\omega_S$, wavevector $\vec{k}_S$ and polarization $\hat{e}_S$. The whole process conserves energy $\omega_L = \omega_S \pm \omega$ for creation (annihilation) of an excitation, but each step is a virtual process and does not need to conserve energy. For a translational invariant system, the wavevector has to be conserved in every step. Thus the wavevector $q$ of the excitation must be equal to the transfered in-plane wavevector $\vec{k}$ in Eq. 3.1: $\vec{q} = \vec{k}$. Disorder in the system can break translation symmetry and thus relax the wavevector conservation condition. In this case momentum can be transfered through disorder.

If $\omega_S < \omega_L$, the process is called Stokes scattering. If $\omega_S > \omega_L$, an excitation is annihilated and this process is called anti-Stokes scattering. The ratio of their intensities $I_{AS}/I_A$can be described as:

$$\frac{I_{AS}}{I_S} = \frac{R_{AS}(\omega_L, \omega_{AS})}{R_S(\omega_L, \omega_S)} \frac{n(\omega)}{n(\omega)+1} \tag{3.2}$$

where $R_{AS}$ ($R_S$) is a pre-factor that depends on incident photon frequency $\omega_L$, the Stokes scattered photon frequency $\omega_S$ and the anti-Stokes scattered photon frequency $\omega_{AS}$; and $n(\omega) = (\exp(\hbar\omega/k_BT) - 1)^{-1}$ is the Bose-Einstein distribution function. In non-resonant conditions, $R_{AS} \approx R_S$, so the ratio becomes $I_{AS}/I_S = \exp(-\hbar\omega/k_BT)$. When $\hbar\omega \gg k_BT$ which occurs at low temperature, the ratio $I_{AS}/I_S \ll 1$ and anti-Stokes intensity is normally negligible. In this thesis I mainly focus on Stokes scattering.

Figure 3.2 shows the laser line, Stokes scattering, and anti-Stokes scattering in both absolute energy scale and Raman shift scale. In absolute energy scale, the horizontal axis is the photon energy. In Raman shift scale, the horizontal axis denotes the photon energy difference with respect to the laser energy and, by convention, Stokes scattering is on the positive side of the laser line.The advantage of plotting light scattering spectra on both scales can help to distinguish inelastic light scattering (two photon process) from optical emission (one photon process).

When the 2DEG system absorbs the incident photons by creation of electron-hole pairs, photon emission can occur after relaxation of the pair into a state with an allowed optical transition. As the final photon emission is only related to the relaxed state, its energy is independent of incident photon energy $\omega_L$. Optical emission and photoluminescence (PL) are used interchangeably in this thesis. Figure 3.3 shows that on absolute energy scale Raman peaks shift while PL peaks stay at fixed energy when incident laser energy $\omega_L$ is tuned. On Raman shift scale, PL peaks shift while Raman peaks stay. In Fig. 3.3, the intensity of Raman peaks get resonant enhancement when incident laser energies is continuously tuned. This is called resonant inelastic light scattering (RILS) and will be explained below.

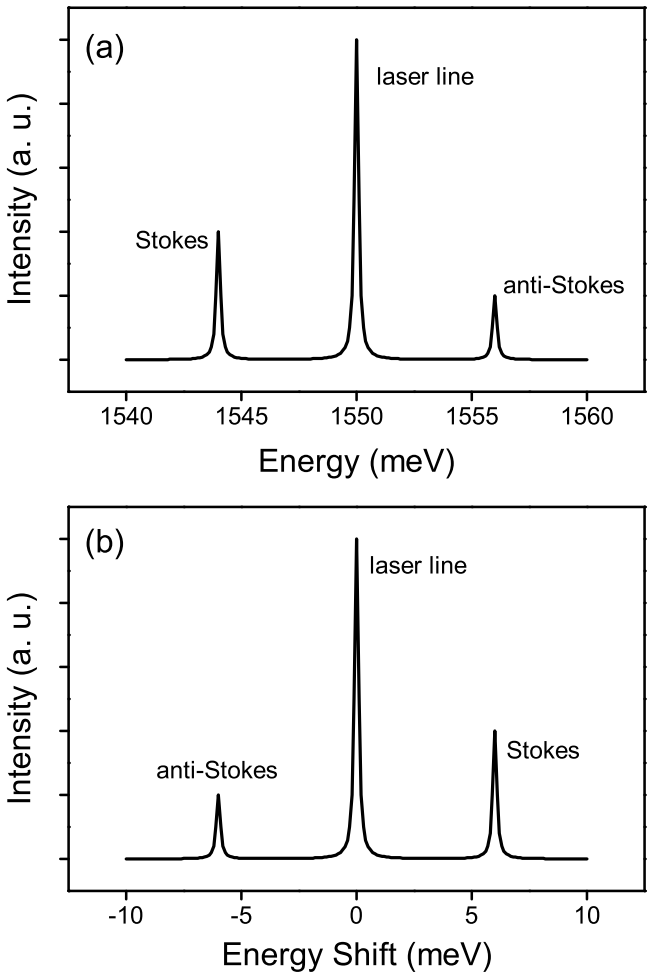


Figure 3.2: Schematic of Stokes scattering and anti-Stokes scattering on both scales: (a) absolute energy scale (b) Raman shift scale. Stokes scattering has energy smaller than laser energy while anti-Stokes scattering has energy larger than laser energy. On Raman shift scale, Stokes scattering has positive shift by convention.

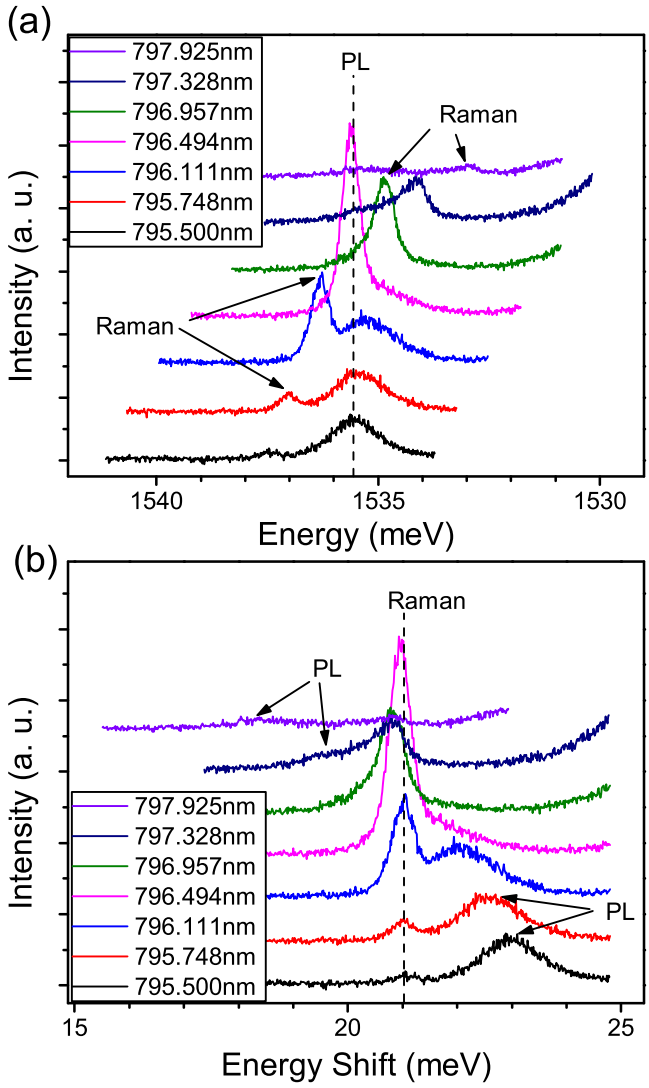


Figure 3.3: RILS by intersubband excitations (Sample # L06-27-14.1 Dev12, $a = 50$ nm pattern) at different laser energies showing both Raman and PL peaks. Spectra are vertically shifted for clarity. (a) Spectra are plotted in absolute energy scale, PL peak stays at fixed energy (vertical dashed line) while Raman peak shifts as incident laser energy varies. (b) Spectra are plotted in Raman shift scale, Raman peak stays at fixed energy shift (vertical dashed line) while PL peak shifts as incident laser energy varies.

### 3.3.2 Inelastic Light Scattering in 3D Systems: Mechanism and Selection Rules

Inelastic light scattering in 3D systems is first discussed here, so it will provide background to discuss light scattering in 2D systems that is relevant to this work.

The Hamiltonian of electrons in the presence of a radiation field can be written as[51]:

$$H = \frac{1}{2m^*}\sum_i [\vec{p}_i + \frac{e}{c}\vec{A}(\vec{r}_i)]^2 + \frac{1}{2}\sum_{i\neq j} V_C(\vec{r}_i - \vec{r}_j) \tag{3.3}$$

where $\vec{A}(\vec{r})$ is the vector potential for the photons, $\vec{p}_i$ is the momentum operator of the electron labeled by index $i$, $\vec{r}_i$ is the electron position and $V_C$ represents electron-electron interaction. The summations extend to all electrons. Magnetic field is ignored here, but it can be considered by adding magnetic related terms in the vector potential[52–54]. We can treat the system perturbatively by rewriting the Hamiltonian as:

$$H = H_0 + H_{int} \tag{3.4}$$

$$= H_0 + H_{ee} + H_{int}^{(1)} + H_{int}^{(2)} \tag{3.5}$$

$$H_0 + H_{ee} = \sum_i \frac{\vec{p}_i^2}{2m^*} + \frac{1}{2}\sum_{i\neq j} V_C(\vec{r}_i - \vec{r}_j) \tag{3.6}$$

$$H_{int}^{(1)} = \frac{e}{2m^*c}\sum_i [\vec{p}_i \cdot \vec{A}(\vec{r}_i) + \vec{A}(\vec{r}_i)\cdot\vec{p}_i] \tag{3.7}$$

$$H_{int}^{(2)} = \frac{e^2}{2m^*c^2}\sum_i |\vec{A}(\vec{r}_i)|^2 \tag{3.8}$$

The $H_{int}^{(2)}$ is a second order term in fields and therefore contributes to the light scattering process described by first order perturbation theory. The $H_{int}^{(1)}$ term is a first order term in fields thus it appears in the second order terms of perturbation theory for the calculation of the light scattering intensity.

The scattering rate from an initial state $|I\rangle$ to a final state $|F\rangle$ can be calculated using Fermi's golden rule[55]:

$$\frac{1}{\tau_{FI}} = \frac{2\pi}{\hbar}|H_{FI}|^2\delta(E_F - E_I - \hbar\omega) \tag{3.9}$$

where

$$H_{FI} = \langle F|H_{int}|I\rangle + \sum_{i>1}\sum_{l_1\cdots l_{i-1}} \frac{\langle F|H_{int}|l_{i-1}\rangle \langle l_{i-1}|H_{int}|l_{i-2}\rangle \cdots \langle l_1|H_{int}|I\rangle}{(E_I - E_{l_{j-1}})(E_I - E_{l_{j-2}})\cdots(E_I - E_{l_1})} \tag{3.10}$$

for all i-step scattering processes where $E_I$ and $E_F$ are the energies of initial and final state and $E_{l_i}$ is the energy of the intermediate state $|l_i\rangle$. To get the total scattering rate, $1/\tau_{FI}$ is summed over all initial states and final states . Each $i$-step process involves $i$ corresponding matrix elements of $H_{int}$ between initial, intermediate or final states described by Eq. 3.10. Resonance enhancement can be achieved when one of the denominator factor goes to zero, resulting a maximum of $H_{FI}$. Only two-step and three-step processes are relevant in this thesis and we will restrict our discussions to two-step and three-step processes.

The scattering rate allows us to quantify the differential cross-section $\frac{d^2\sigma}{d\Omega d\omega}$ as[54, 56]:

$$\frac{d^2\sigma}{d\Omega d\omega} = \hbar\frac{\omega_S}{\omega_L}\left\langle \sum_F \mid M_{FI} \mid^2 \delta(E_F - E_I - \hbar\omega)\right\rangle \tag{3.11}$$

where $M_{FI}$ is the relevant matrix element, $\Omega$ is the solid angle and the angle brackets indicate average over the initial states in thermal equilibrium.

We restrict discussion here to be light scattering via single electron states in a semiconductor. Since light scattering is second order in vector potential, the lowest order perturbation theory expansion of $M_{FI}$ is first order in $H_{int}^{(2)}$ and second order in $H_{int}^{(1)}$[54, 57]. $M_{FI}$ can be rewritten as

$$M_{FI} = r_0 \sum_{\alpha,\beta} \gamma_{\alpha\beta} \langle F|C_\alpha^\dagger C_\beta|I\rangle \tag{3.12}$$

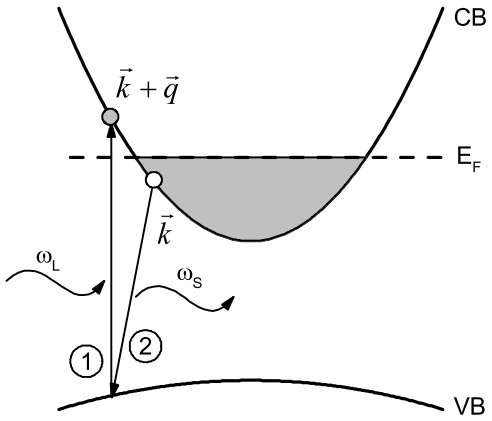


Figure 3.4: Transition diagram showing intraband single-particle excitations from two-step light scattering process in GaAs. The time ordering of transitions are indicated by numbers. In step one, the incident photon $\omega_L$ excites an electron from the valence band (VB) to conduction band (CB) state above Fermi level, leaving a hole in the valence band. In step two, an electron from the conduction band below Fermi level recombines with the hole and emits a scattered photon $\omega_S$. These two transitions are both virtual.

where $r_0 = e^2/m^*c^2$ is the "classical" electron radius. $\alpha$ and $\beta$ are labels for the electron states, which are characterized by wavevector and spin $s_\alpha$; $C_\alpha^\dagger$ and $C_\alpha$ are the creation and annihilation operators for the single particle state $|\alpha\rangle$. Coefficient $\gamma_{\alpha\beta}$ is given by:

$$\gamma_{\alpha\beta} = \langle\alpha|e^{i\vec{q}\cdot\vec{r}}|\beta\rangle\,\hat{e}_L\cdot\hat{e}_S + \sum_l \Big[\frac{\langle\alpha|j_S|l\rangle\,\langle l|j_L|\beta\rangle}{E_\beta - E_l + \hbar\omega_L} + \frac{\langle\alpha|j_L|l\rangle\,\langle l|j_S|\beta\rangle}{E_\alpha - E_l - \hbar\omega_L}\Big] \tag{3.13}$$

where $j_{L(S)} = \hat{e}_{L(S)}\cdot\vec{p}e^{\pm i\vec{k}_{L(S)}\cdot\vec{r}}/m^*$. $E_\alpha(E_\beta)$ is the energy of the single particle state $|\alpha\rangle\,(|\beta\rangle)$ and $E_l$ is the energy of intermediate state $|l\rangle$. For intraband scattering and scattering from free electrons, the second and third term in $\gamma_{\alpha\beta}$ almost cancel each other[52] thus the first term dominates. The first term comes from $H_{int}^{(2)}$ and is clearly non-resonant. The last two terms are linked to the second order contributions of $\vec{p}\cdot\vec{A}$ term which is in $H_{int}^{(1)}$. For interband transitions the cancellation of the last two terms in $\gamma_{\alpha\beta}$ does not occur, so $H_{int}^{(1)}$ is essential in light scattering of interband transitions. The role of $H_{int}^{(1)}$ can be significant when the resonant enhancement of light scattering cross-section happens if the photon energy is close to the energy gap[52] and the denominator approaches zero. In this case $H_{int}^{(1)}$ is responsible for resonant effect, and examples of such transitions are shown in Fig. 3.4. Electron-electron interaction $H_{ee}$ plays is not relevant in the two-step light scattering processes described above, but it is important in three-step processes.

To simplify the expressions of light scattering cross-section, we consider the electronic band structures of GaAs around zone center as this is our primary experimental interest. Kane model[58] is an appropriate model to describe the band structures here based on n-type III-V semiconductors with electrons occupying the Brillouin zone center (the Γ-point). In the Kane model, the conduction band states are s-like and we denote them as $S\uparrow$ and $S\downarrow$ where S denotes spatial part of wavefunctions and the arrow denotes spin orientation. The valence band basis functions are p-like and are

| band | $\|J, J_z\rangle$ | wavefunction |
|---|---|---|
| cb | $\|\frac{1}{2}, +\frac{1}{2}\rangle$ | $S \uparrow$ |
| | $\|\frac{1}{2}, -\frac{1}{2}\rangle$ | $S \downarrow$ |
| hh | $\|\frac{3}{2}, +\frac{3}{2}\rangle$ | $\sqrt{\frac{1}{2}}(X + iY) \uparrow$ |
| | $\|\frac{3}{2}, -\frac{3}{2}\rangle$ | $\sqrt{\frac{1}{2}}(X - iY) \downarrow$ |
| lh | $\|\frac{3}{2}, +\frac{1}{2}\rangle$ | $\sqrt{\frac{1}{6}}(X + iY) \downarrow - \sqrt{\frac{2}{3}}Z \uparrow$ |
| | $\|\frac{3}{2}, -\frac{1}{2}\rangle$ | $\sqrt{\frac{1}{6}}(X - iY) \uparrow + \sqrt{\frac{2}{3}}Z \downarrow$ |
| so | $\|\frac{1}{2}, +\frac{1}{2}\rangle$ | $\sqrt{\frac{1}{3}}(X + iY) \downarrow + \sqrt{\frac{1}{3}}Z \uparrow$ |
| | $\|\frac{1}{2}, -\frac{1}{2}\rangle$ | $\sqrt{\frac{1}{3}}(X - iY) \uparrow - \sqrt{\frac{1}{3}}Z \downarrow$ |

Table 3.1: Wavefunctions along $k_z$ for electron states of GaAs near zone center from Kane model for conduction band (cb), heavy hole (hh), light hole (lh) and split-off (so) valence bands. Electron states are labeled by total angular momentum $J$ and its z-component $J_z$.

denoted as $X \uparrow$, $X \downarrow$, $Y \uparrow$, $Y \downarrow$, $Z \uparrow$ and $Z \downarrow$. These basis can be combined into states with good quantum number (total angular momentum $J$ and its z-component $J_z$) to produce zone center wavefunctions (along $k_z$) listed in Table 3.1.

Using the Kane model and the approximation $\omega_L \sim \omega_S$, Hamilton and McWhorter[59] have obtained:

$$\gamma_{\alpha\beta} = \langle\alpha|e^{i\vec{q}\cdot\vec{r}}|\beta\rangle \left[\hat{e}_L \cdot \overleftrightarrow{A} \cdot \hat{e}_S + i(\hat{e}_L \times \hat{e}_S) \cdot \overleftrightarrow{B} \cdot \langle s_\alpha|\vec{\sigma}|s_\beta\rangle\right] \tag{3.14}$$

where $\vec{\sigma}$ is the vector form of the Pauli matrices, and $|s_\alpha\rangle(|s_\beta\rangle)$ is the spin state of $|\alpha\rangle(|\beta\rangle)$. $\overleftrightarrow{A}$ and $\overleftrightarrow{B}$ are tensors we will discuss their forms in the following sections. They are linked to excitations with and without a change in spin state respectively. In the following sections, we can see that light scattering from electrons in GaAs will consist of two distinct components: one that is symmetric in the polarizations and the other that is antisymmetric in the polarizations. In other words, one is maximized when the polarization of the incident photon is parallel with the polarization of the scattered photon while the other is maximized when their polarizations are perpen-

dicular. Out of resonance, we have $\overleftrightarrow{A} \propto \overleftrightarrow{m}^{*-1}$, where $\overleftrightarrow{m}^{*}$ is the effective mass tensor, so the first term is related only to charge density excitations. On the other hand, the Pauli matrices in the second term show that it is related to excitations with a change in the spin quantum number. This ability to differentiate between charge and spin density excitations by using polarization selection rules is one powerful aspect of inelastic light scattering.

#### 3.3.2.1 Parallel Polarization

Consider the case of $\hat{e}_L \parallel \hat{e}_S$ and assume parabolic valence bands, we can get the form of $\overleftrightarrow{A}$ as[59]:

$$\overleftrightarrow{A} = \overleftrightarrow{I}\left[1 + \frac{2P^2}{3m}\left(\frac{E_1^*}{E_1^{*2} - (\hbar\omega_L)^2} + \frac{E_2^*}{E_2^{*2} - (\hbar\omega_L)^2} + \frac{E_3^*}{E_3^{*2} - (\hbar\omega_L)^2}\right)\right] \tag{3.15}$$

where $\overleftrightarrow{A}$ is the unit matrix, $P = |\langle S|p_z|Z\rangle|$ is the interband matrix element of the momentum and $E_1^*$, $E_2^*$ and $E_3^*$ are the gaps associated with the heavy, light and split-off valence band from the Kane model[58]. In GaAs the heavy and light valence bands are degenerate at the Γ-point and the split-off valence band is separated by $\Delta_0$ shown in Fig. 3.5. At low temperature, $E_1^* \approx E_2^* \approx E_0 = 1.519$ eV and $E_3^* = E_0 + \Delta_0 = 1.859$ eV[60]. This term in $\gamma_{\alpha\beta}$ is symmetric in the incident and scattered polarizations and will be maximized in parallel polarizations and minimized in perpendicular polarizations.

#### 3.3.2.2 Cross Polarizations

Now we consider the case of $\hat{e}_L \perp \hat{e}_S$. The second part of $\gamma_{\alpha\beta}$ in Eq. 3.14 can be written as:

$$\overleftrightarrow{B} = \overleftrightarrow{I}\frac{2P^2}{3m}\hbar\omega_L\left[\frac{1}{E_0^2 - (\hbar\omega_L)^2} - \frac{1}{(E_0 + \Delta_0)^2 - (\hbar\omega_L)^2}\right] \tag{3.16}$$

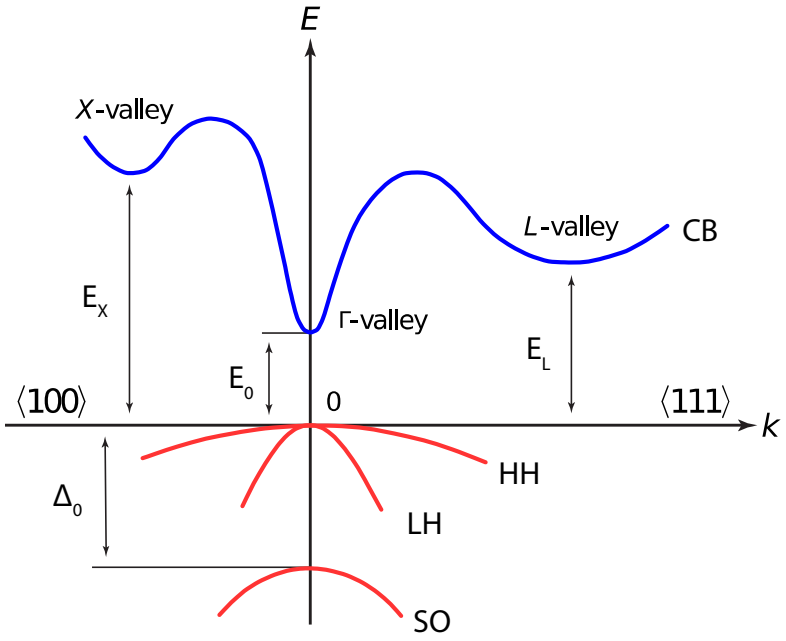


Figure 3.5: Schematic of band structures of bulk GaAs. Heavy hole (HH) and light hole (LH) bands are degenerate and split-off (SO) valence band is separated by $\Delta_0$.

We can see here $\overleftrightarrow{B} \to 0$ as $\omega_L \to 0$ which was discussed earlier in Eq. 3.13 and as $\Delta_0 \to 0$. The Pauli matrix $\langle s_\alpha|\vec{\sigma}|s_\beta\rangle$ term is only non-zero when $|\alpha\rangle$ and $|\beta\rangle$ have different spin states, so this antisymmetric term is proportional to electron density fluctuation for each value of spin[57]. This term is related to spin density excitations and will be maximized in perpendicular polarization and vanish in parallel polarization.

### 3.3.3 RILS in 2D Systems

We have discussed resonant inelastic light scattering in 3D electron systems, but our main interest is in 2D electron systems. It turns out that most of the results in 3D case are also applicable in 2D systems. If we examine the Hamiltonian describing the in-plan behavior of the electrons in the 3D system, we can find that it is equivalent to what is in the 2D systems with effective mass approximation. In particular the light scattering mechanisms in 2D and 3D systems are similar and so are the polarization selection rules[61]. However the exact matrix elements and selection rules for electron transitions within a quantum well are more complicated due to the mixing of the heavy and light holes in the valence band.

In fact it was initially thought that the intensities of inelastic light scattering from 2D electron gases would be too weak to be observable. In 1978, Burstein and Pinczuk[62] proposed that resonant enhancement should make light scattering sensitive enough to observe electronic excitations of 2DEG with densities about $10^{11}$ $\text{cm}^{-2}$. Soon after this proposal, experimental observations of intersubband excitations of 2DEG were reported by Pinczuk et al. [63] and Abstreiter and Ploog[64] using the resonant enhancement of the $E_0 + \Delta_0$ gap.

Resonant inelastic light scattering spectroscopy in 2D systems are powerful because it can both probe and differentiate between collective and single-level excitations. Moreover it can distinguish charge and spin excitations. This allows for the

determination of energy level structures and electron-electron interaction energies which are of key interests in these systems. In addition, it can access modes that are extremely weak for other techniques, such as transmission or absorption.

Figure 3.6 shows the two step light scattering processes for intersubband excitations as well as intrasubband excitations in 2D systems, similar to that in Fig. 3.4 for 3D systems. Intersubband excitations involve more than one subband while intrasubband excitations involve only one subband. Similar to the case of 3D systems, the intensity of light scattering in 2D systems is proportional to the matrix element:

$$I(\omega) \propto \left| \sum_{l} \frac{\langle F|H_{int}^{(1)}|l\rangle \langle l|H_{int}^{(1)}|I\rangle}{\omega_I - \omega_l} \right|^2 \tag{3.17}$$

where $|I\rangle$, $|F\rangle$ and $|l\rangle$ are the initial state, final state and intermediate state. $H_{int}^{(1)}$ is the interaction Hamiltonian defined in Eq. 3.7. $\omega_I$ and $\omega_l$ are the energies of the initial state and intermediate state respectively. From this equation we can clearly see the resonance condition for this two-step light scattering as the denominator goes to zero: $\omega_I - \omega_l = \omega_L - (E_0 + \Delta_{10}) = \omega_S - E_0 \to 0$, where $E_0$ is the band gap between conduction band and valence band, and $\Delta_{10}$ is the energy shift between subband 0 and subband 1. This expression shows that a resonance arises when the incident photon energy matches $E_0 + \Delta_{10}$ (called incoming resonance) or when the scattered photon energy matches $E_0$ (called outgoing resonance).

There are more complicated light scattering processes such as three-step process. Figure 3.7 shows a Feynman diagram that describes a three-step Raman scattering process. The first and last step are same steps as the two-step process just described above. However the second step involves an electron-electron interaction which causes a transition from the first intermediate state to a second intermediate state, resulting an emission of a collective mode as described by:

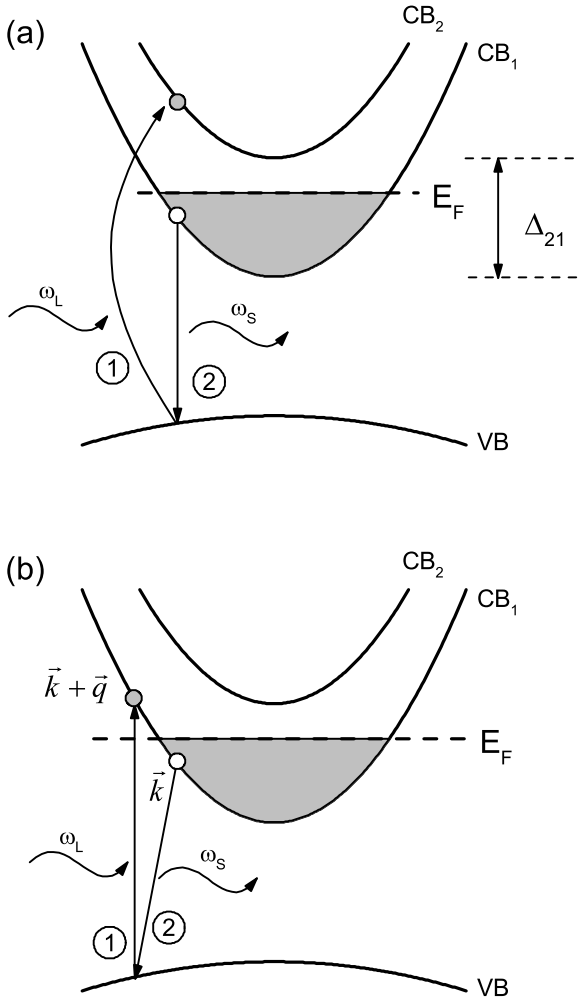


Figure 3.6: Transition diagram showing (a) intersubband excitation and (b) intrasubband excitation from two-step light scattering process in GaAs. The time ordering of transitions are indicated by numbers. In step one, the incident photon $\omega_L$ excites an electron from the valence band (VB) to conduction band (CB) state above Fermi level, leaving a hole in the valence band. In step two, an electron from the conduction band below Fermi level recombines with the hole and emits a scattered photon $\omega_S$. The two steps involve different subbands for intersubband excitations while they occur in same subband for intrasubband excitations.

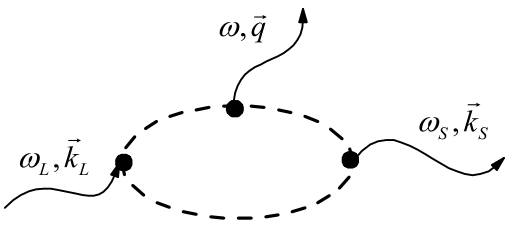


Figure 3.7: Feynman diagram showing a three-step inelastic light scattering process. In step 1, the incident photon $\omega_L, \vec{k}_L$ is annihilated and creates an electron-hole pair. In step 2, the electron-hole pair interacts with the 2D system to emit a collective excitation $\omega, \vec{q}$. In step 3, electron-hole pair is annihilated and emits the scattered photon. Alternative time ordering might be possible.

$$I(\omega) \propto \left| \frac{\langle F|H_{int}^{(1)}|l_2\rangle \langle l_2|H_{ee}|l_1\rangle \langle l_1|H_{int}^{(1)}|I\rangle}{(\omega_I - \omega_{l_2})(\omega_I - \omega_{l_1})} \right|^2 \tag{3.18}$$

In addition the same resonance related to $l_1$ transition, the three-step process has a second resonance condition associated with $l_2$: $\omega_I - \omega_{l_2} = \omega_L - (E_{l_2} + \omega) = \omega_S - E_{l_2}$, where $E_{l_2}$ is the energy of the transition between $|l_2\rangle$ and $|I\rangle$. Because this resonance condition is determined by the overlap of the scattered photon energy with an optical transition, it is referred as an outgoing resonance.

## 3.4 Optical Emission

Optical emission (or photoluminescence, PL) provides another useful way to probe electronic band structures. In 2D electron systems, optical emission occurs when electrons recombine with photo-excited holes. With respect to GaAs QWs, the line-shapes of optical emission often give insight into the Fermi energy or electron density of the system. Although it is often easier to get optical emission than light scattering, it is sometimes harder to interpret optical emission. Thus only some preliminary discussions are devoted to optical emission and more discussion in depth can be found in Ref.[65].

A schematic of optical emission in GaAs QW is shown in Fig. 3.8. An incident photon with energy $\omega_L$ can be absorbed if its energy is larger enough to excite an electron from the valence band to a state above the Fermi level. This creates an electron-hole pair as shown in Fig. 3.8(a). The electron-hole pair will thermalize to a relaxed state via phonon scattering[66] as shown in Fig. 3.8(b). Photo-excited holes form non-degenerate hole gas and can recombine with electrons in the conduction band and emit a photon. The recombination occurring at the bottom of the conduction band has the minimum photon energy denoted by $E_1$ shown in Fig. 3.8(c) while the one occurring at Fermi level has the maximum photon energy denoted by

$E_2$ shown in Fig. 3.8(d). Assuming parabolic shape of both conduction band and valence band, electron Fermi energy can be calculated in terms of $E_1$ and $E_2$[67, 68]:

$$E_F = \frac{m_h}{m_e + m_h}\Delta E \tag{3.19}$$

$$\Delta E = E_2 - E_1 \tag{3.20}$$

where $m_e$ and $m_h$ are effective masses of electron and hole of GaAs. Typical values of effective masses are often used[69]: $m_e = 0.068m_0$ and $m_h = 0.45m_0$, where $m_0$ is rest electron mass in vacuum.

The intensity of optical emission $I(E)$ in a GaAs QW can be derived similarly to Ref.[70]. When $E < E_1$, optical emission is not allowed; when $E \geq E_1$, intensity can be described as:

$$I(E) \propto |M|^2 f(E_c(k))(1 - f(E_v(k)))\delta(E_c(k) - E_v(k) - E)d^2k \tag{3.21}$$

where $M$ is the matrix element, $f(E) = 1/(1 + e^{(E-E_F)/k_BT})$ is the Fermi-Dirac distribution function, $E_c(k)$ ($E_v(k)$) is the conduction (valence) band energy, and $\delta(E_c(k) - E_v(k) - E)$ represents the conservation of energy. The conservation of momentum is implicitly included by using same $k$ in the conduction and valence band energies while the transferred in-plane momentum by phonon is ignored. Same as before, we use parabolic band structures to simplify the intensity expression:

$$E_c(k) = \frac{\hbar^2}{2m_e}k^2 \tag{3.22}$$

$$E_v(k) = -\frac{\hbar^2}{2m_h}k^2 - E_1 \tag{3.23}$$

Conduction and valence band energies can be solved via energy conservation $E_c -$

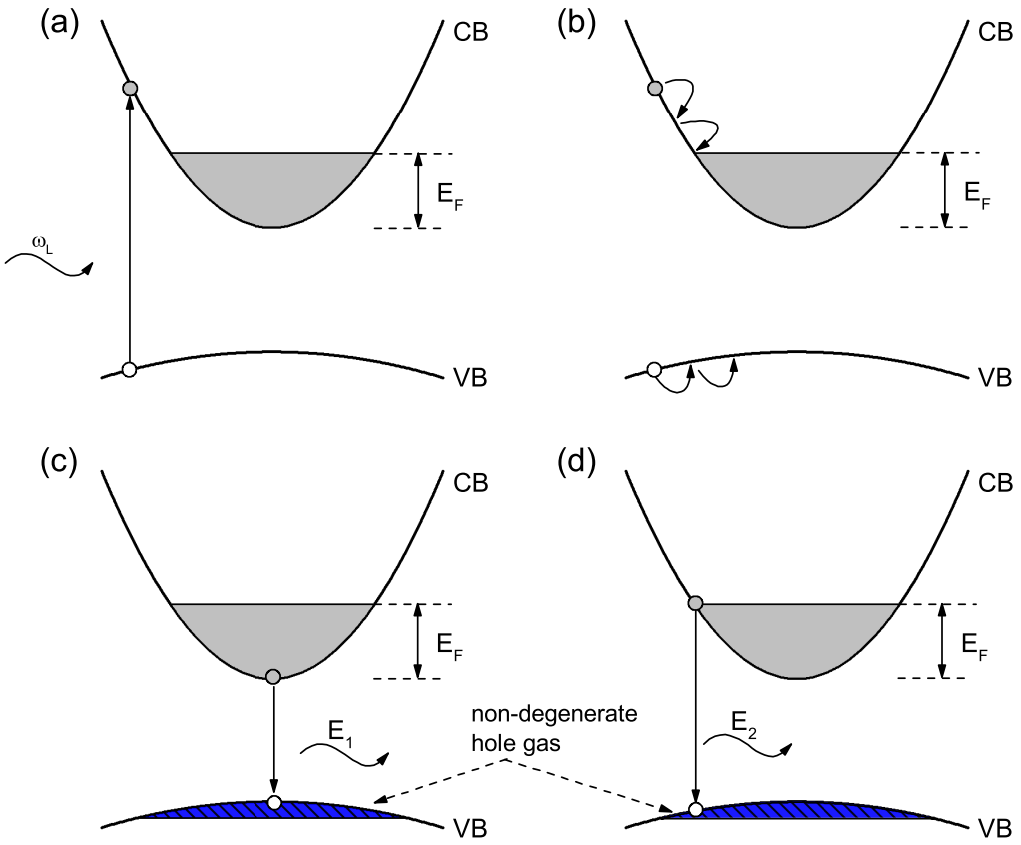


Figure 3.8: Schematic of optical emission from 2DEG in GaAs QW.(a) An incident photon $\omega_L$ is absorbed, resulting an electron-hole pair. (b)The electron-hole pair thermalizes. Then it relaxes to a state where the emission of a photon can occur at (c) bottom of conduction band with energy $E_1$ or (d) occurring at Fermi level with energy $E_2$. $E_1$ and $E_2$ are the minimum and maximum energy of the optical emission.

$E_v = E$:

$$E_c = \frac{m_h}{m_e + m_h}(E - E_1) \tag{3.24}$$

$$E_v = -\frac{m_e}{m_e + m_h}(E - E_1) - E_1 \tag{3.25}$$

Equation 3.21 can be simplified using Eq. 3.22-3.25:

$$I(E) \propto |M|^2 \frac{1}{1 + e^{(E_c - E_F)/k_B T}} \frac{1}{1 + e^{-(E_v - E_F)/k_B T}} \frac{2\pi m_e m_h}{\hbar^2 (m_e + m_h)} \tag{3.26}$$

$$\propto \frac{1}{1 + \exp\left(\frac{m_h}{m_e + m_h} \frac{E - E_2}{k_B T}\right)} \exp\left(-\frac{m_e}{m_e + m_h} \frac{E}{k_B T}\right) \tag{3.27}$$

where several constant factors are dropped out in Eq. 3.27. $|M|$ does not depend on $E$ when parabolic dispersion is applicable, thus it is constant in the evaluation of $I(E)$. The factor of $\frac{1}{1+e^{-(E_v - E_F)/k_B T}}$ in Eq. 3.26 represents the non-degenerate hole gas distribution, the factor 1 in the denominator is ignored in Eq. 3.27 since the exponential part is much larger than 1. The last term in Eq. 3.26 represent the joint density of states between conduction band and valence band which is a constant for parabolic shape band structure, thus it is ignored in Eq. 3.27.

The overall shape of optical emission is surprisingly determined by the non-degenerate hole distribution as we can see in Eq. 3.27. It has exponential decay as the energy increases, and the decay rate depends crucially on temperature.

The first term in Eq. 3.27, the Fermi-Dirac distribution, will only come to play when energy is close to $E_2$. Thus a cut-off will appear around $E_2$.

Remarkably Eq. 3.27 describes the obtained optical emission spectra well, shown in Fig. 3.9, except on the low energy range around $E_1$. Ideally $I(E)$ jumps from zero to maximum value at $E = E_1$, but broadening due to various effects, such as fluctuation of QW thickness and defects, will smooth this step-function behavior and form a tail on the low energy side. A smoothed step function, $\arctan(\frac{E - E_1}{\Gamma})/\pi + 1/2$, is employed here to fit the spectra and $\Gamma$ is a fitting parameter that can determine the smoothness of such step function. The complete fitting of optical emission, shown in

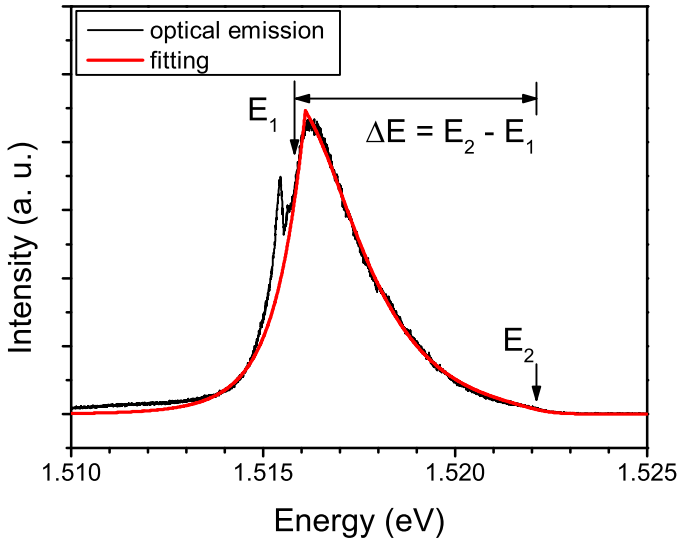


Figure 3.9: Optical emission from 2DEG in GaAs QW. Red curve is the best fit of optical emission spectrum using Eq. 3.27 (described in text). $E_1$ and $E_2$ correspond to transitions at the bottom of conduction band and at Fermi level respectively as described in Fig. 3.8.

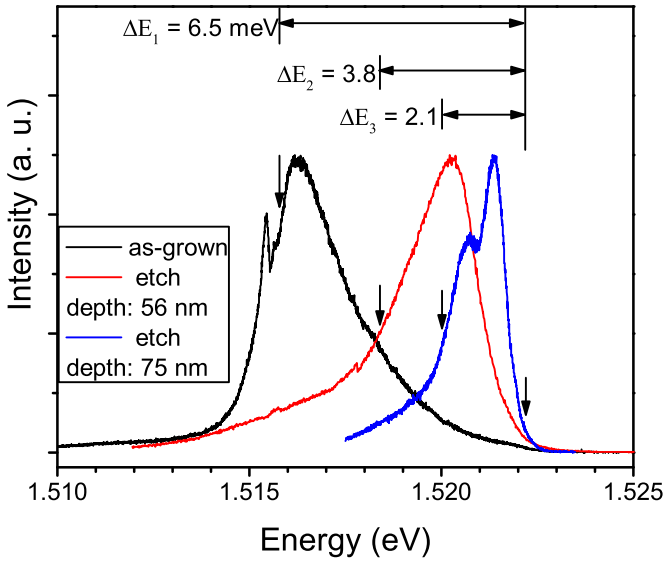


Figure 3.10: Optical emission from as-grown and nano-patterned QW. The energy difference between $E_2$ and $E_1$, $\Delta E$, is labeled for each spectrum. There is a reduction of Fermi energy for the nano-patterned samples, and the deeper etched sample has larger reduction.

Fig. 3.9, is in good agreement with experimental data for energies above $E_1$ while it also captures the low energy tail below $E_1$. The sharp peak around 1.515 eV in optical emission may be due to defect states and will not be discussed here. The two critical energies $E_1$ and $E_2$, shown in Fig. 3.9, can be extracted from the fitting parameters to calculate Fermi energy via Eq. 3.19. Additionally the electron temperature can also be extracted from optical emission spectra, and this is especially useful when electron temperature is shifted from the cold-finger temperature due to various effects such as spacial gradient of temperature and heating effect by absorption of photons.

In this thesis, optical emission spectra are primarily used to monitor the Fermi energy of electrons in the artificial lattices created in nano-patterned GaAs QWs. An example is shown in Fig. 3.10. Optical emission of the as-grown sample is plotted for comparisons with those from AG lattices on nano-patterned QW with different etch depth. The energy difference between $E_2$ and $E_1$ (Eq. 3.20), $\Delta E$, is indicated to monitor the Fermi energies of each sample. We can clearly see a reduction of Fermi energy in the nano-patterned samples. It is easy to see that the larger etch depth, the more reduction of Fermi energy. For the as-grown sample, the Fermi energy is calculated to be $E_{F1} = 5.7$ meV, via Eq. 3.19. As the AG potential modifies band structures, the ratio of valence band contribution to $\Delta E$ is no longer a constant in nano-patterned samples. As a rule of thumb, we deduct 10% from $\Delta E$ to estimate the Fermi energy. The Fermi energies of the two nano-patterned samples are: $F_{F2} = 3.4$ meV, $E_{F3} = 1.9$ meV. Combined with RILS, optical emission provides unique access to electron states in nano-patterned structures which will be described in Chapter 6.

# Chapter 4

# Nano-fabrication of AG Lattices in GaAs QWs

## 4.1 Introduction

The pioneering work on band engineering of semiconductors by Esaki and Tsu[26] in 1970 proposed a one-dimensional periodic potential structure, or "superlattice", in which electron minibands can be formed. Lateral nano-patterned semiconductor QWs with lateral periodic lattices were intensively studied in the late 1980s and 1990s [27–34].

Lateral nanopatterns offer great tunability for manipulation of electron states. The external periodic potential can be controlled to generate different electron systems from weakly modulated 2D electron gas to isolated quantum dots. Both atom-like single particle behavior and collective many-body effects were observed from such systems[29–33]. However clear cut evidences of the electron miniband structures in lateral superlattice systems were not observed, because the periods were relatively large (>400 nm) due to fabrication limit. Large periods minibands are not resolved due to the broadening effects from temperature and disorder. While periods of 10

nm can be produced by MBE in the growth direction[26], such periods in the plane perpendicular to growth directions are very difficult to achieve. Technologies used in lateral patterning, such as electron beam (E-beam) lithography, depositions, and etching, met challenges to produce structures with periods less than 100 nm.

As graphene attracts lots of interest, its linear energy-momentum dispersion described by the Dirac equation, known as massless Dirac fermions (MDFs)[1, 2], is a direct result of the lattice symmetry. Artificial graphene, engineered lattice in honeycomb or triangle topology, is a platform to explore new physics that emerges from the tunable interplay between topology and quasiparticle interactions[12–14, 17, 20].

AG physics has been studied for molecules on metallic surfaces[17], cold atoms in optical lattices[18–20] and photonic crystals[21–25]. It would be promising to realize AG in an engineered high-mobility semiconductor system such as that offered by GaAs QWs, that is highly adjustable, scalable and can be integrated with other electronic devices. Previous reports on nano-patterned GaAs QW find no evidence of AG minibands or MDFs because its still relative large periods[13, 36, 37, 39]. To have linearly-dispersed bands not washed away by broadening effect, AG lattices with lattice constants well below 100 nm are required.

In this chapter we demonstrate small period AG lattices on nano-patterned GaAs QWs with lattice constants as low as 40 nm. These results define the current state-of-the-art in the field. We will go through the key steps required to achieve such high resolution AG lattices in the following sections. These achievements makes the observation of electron minibands and studies of Dirac physics possible.

## 4.2 Fabrication Methods

A periodic potential modulation of 2DEG can be achieved by either through a patterned top gate[31–33, 71–74] or by etching the patterned surface, forming an array

of nanowires or nanodots[13, 29, 30, 36, 37, 39]. In this thesis we employed the latter approach as it creates strong modulation potential when the etch brings the surface close to the QW. It is also easier to be implemented than the top gate approach because electrode will lose contact to 2DEG when electrons are localized underneath pillars.

The steps in nano-fabrication of AG patterns is illustrated in Fig. 4.1. It mainly consists two segments. First a honeycomb array of etch mask is defined by E-beam lithography. Then inductively coupled plasma (ICP) reactive-ion etching (RIE) is used to etch away the material outside the mask. Different photoresists and processing procedures are tested, and the optimized method for producing nanodots with large diameter and superior uniformity is described below.

### 4.2.1 Metal Mask by E-beam Lithography

First the sample was spin-coated with a 40 nm-thick film polymethyl-methacrylate (PMMA) of molecular weight 35K, to form the bottom layer as shown in Fig. 4.1, and baked for 5 min at 180 ℃. Then another 30 nm thick layer of 495K molecular weight PMMA was spun and baked at 180 ℃ for 15 min. Since the sensitivity of PMMA is higher for lower molecular weight, the bottom layer develops more rapidly than the top layer, causing an undercut profile to form upon development, which facilitates the subsequent metal lift-off.

The E-beam exposure was performed with a beam current of 400 pA and an accelerating voltage of 80 kV. The 200 $\times$ 200 $\mu$m$^2$ AG lattices were patterned by exposing honeycomb arrays of circles with various lattice constants (40, 50, 60, and 70 nm). The diameter of the circles was varied as a function of period, and the exposure dose ranged between 500 and 2500 C/cm$^2$.

The resist was developed for 60 s in a solution of methyl isobutyl ketone : isopropanol (MIBK:IPA, 1:3 by volume) at 5 ℃, applying ultrasonic agitation for in-

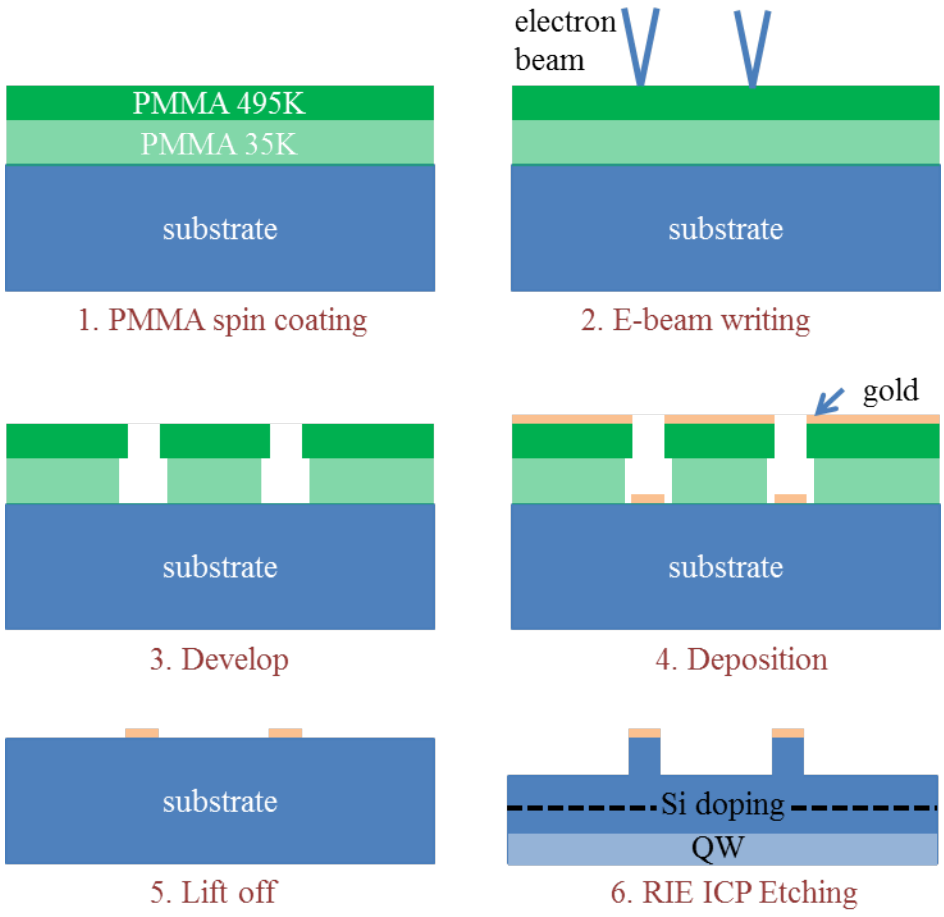


Figure 4.1: Steps in of nano-fabrication of AG patterns. Six steps are outlined here: (1) PMMA spin coating (2) E-beam writing (3) develop (4) deposition (5) lift off (6) ICP-RIE etching. Details of each step are described in text. The Si doping layer and QW is only indicated in (6) for clarity.

creased resolution and contrast[75, 76], then rinsed in isopropyl alcohol. After the development, the samples were under a 10 s oxygen plasma treatment (Diener Tetra 30 PC plasma cleaner, 0.25 mbar, 4 sccm $O_2$ flow, 212 V DC bias, and 300 W RF power at 13.56 MHz) to eliminate residual resist from within the developed features and terminate the surface of the sample with hydroxyl groups, which can aid in adhesion of the metal mask.

Electron beam evaporation was used to deposit 2 nm Ti (adhesion layer) followed by 8 nm Au as shown in Fig. 4.1(4). The metal deposition was performed at a rate of 0.5 Å/s while maintaining the chamber pressure below 5 $\times 10^7$ mbar (Angstrom EvoVac e-beam evaporator). The lift-off of the metal was accomplished by soaking the sample for 12 h in Remover PG (MicroChem), solution containing N-methyl-2-pyrrolidone (NMP), and then spraying acetone with a syringe for complete removal of the resist and any metallic debris, followed by rinsing in IPA and water.

### 4.2.2 ICP RIE Etching

The honeycomb array of Au nanodisks was transferred to the GaAs QW wafer using the ICP-RIE etcher(Samco International RIE200iP) at the PRISM Micro/Nano Fabrication Laboratory of Princeton University. This is the last step in Fig. 4.1.

The plasma conditions were controlled by means of two independent RF power sources. The first RF source (RF1) was inductively coupled to the gas in the process chamber (13.56 MHz, maximum power 1000 W), capable of generating a high density of radicals and ions without applying a potential difference between the plasma and the wafer surface. The second RF source (RF2) operates by applying a DC bias between the chuck and the plasma (13.56 MHz, maximum power 300 W), as in the case of traditional RIE, primarily affecting the ion energy. The advantages of using ICP etching over conventional parallel plate RIE are well documented; of particular importance to this work is the ability to adjust the plasma density and the ion energy

separately, allowing for a better tuning of the degree of anisotropy of the etch.

Samples of GaAs QW with honeycomb patterns were mounted on a silica carrier wafer with silicone-based vacuum grease, and the chuck temperature was maintained at 50 °C during the etch. The gas employed was a mixture of 50 sccm Ar and 5 sccm $BCl_3$, which has been shown to achieve nonselective etching of GaAs/AlGaAs heterostructures with good degree of anisotropy[77, 78]. We independently varied the power of the two RF sources within the range of 50-75 W in order to optimize the vertical sidewall profile. The chamber pressure was set at 3.7 mbar in all the cases, and the etch time was varied between 60 and 150 s.

Following the dry etching, it is possible to remove the gold mask by a few-second immersion in a TFA gold etchant solution (Transene Company, Inc.) at room temperature, which does not alter the patterned surface. Nevertheless the presence of the gold nanodisks on top of the etched pillars, it is not expected to have an observable effect on the electron density modulation of the 2DEG and the surface state filling mechanism, since the density of states of these gold nanoparticles at the chemical potential is very low due to their small size and to the electron confinement.

## 4.3 Results and Discussion

Our E-beam lithography method, which creates a metallic etch mask via lift-off, was shown to be capable of achieving honeycomb lattices with period as small as 40 nm and with excellent uniformity.

Figs. 4.2(a-d) show representative SEM micrographs of Au masks with lattice period 50 and 70 nm and different disk diameters. The ability to vary the disk diameter is critical for optimal tuning of the honeycomb potential that generates the artificial graphene. Moreover, in reducing the scale, it is essential to maintain a high lattice uniformity, i.e., homogeneous disk diameter and lattice period, as well as to

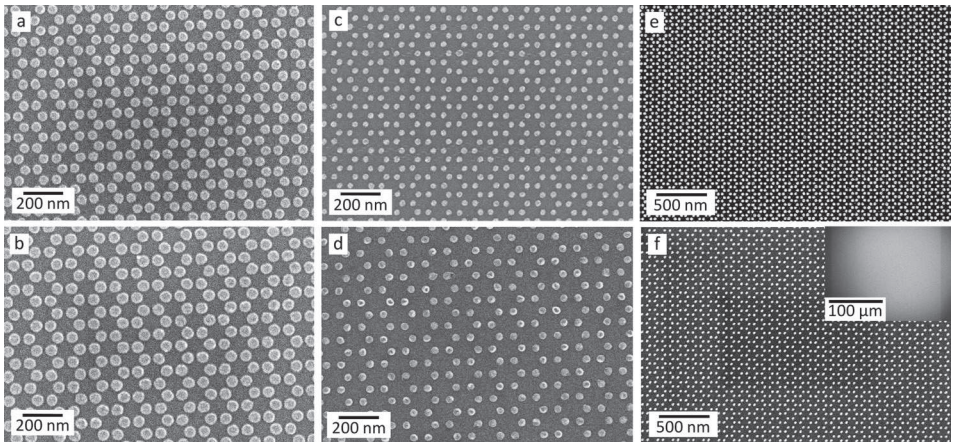


Figure 4.2: SEM micrographs of honeycomb arrays of Au nanodisks constituting the mask for the dry etching, with a variation in the lattice period and disk diameter. (QW sample # L06-27-14.1) (a) 50 nm period and 40nm diameter, (b) 70nm period and 60nm diameter, (c) 50nm period and 25nm diameter, and (d) 70nm period and 35nm diameter. Lower magnification images in (e) and (f) show defect-free arrays with excellent uniformity over tens of unit cells for 40 nm and 50 nm period, respectively. Inset: low magnification image of the entire 200 $\times$ 200 $\mu$m$^2$ array.

avoid lattice defects, such as missing or misplaced sites. Lower magnification SEM images of honeycomb lattices with 40 and 50 nm period can be seen in Figs. 4.2(e-f), respectively, for which these requirements are met over dozens of unit cells.

We note that the achievement of high-resolution and uniform arrays over large areas (up to 200 $\times$ 200 $\mu$m$^2$ in this work) by electron beam lithography and lift-off becomes increasingly challenging as the feature size and period are decreased. This is especially true for relatively high atomic number substrates such as GaAs (Z = 32), where the backscattering intensity is about 40% higher than on Si[79]. The process we have developed is both high resolution and low contrast, enabling us to achieve uniform honeycomb lattices with periods as small as 40 nm.

After etching, the samples were examined in a Hitachi S4700 SEM, with 65° tilt angle, acceleration voltage 20 kV and current 10 $\mu$A. The two AG lattices shown in Fig. 4.3 had identically patterned hard-masks but were etched with two different processes, as described in Subsection 4.2.2 on ICP RIE etching. One can see how the lattice in Fig. 4.3(a), which underwent an etch with higher ICP RF power (75 W) and lower bias-inducing RF power (50 W), presents evidence of lateral etching, resulting in the collapse of some pillars. Modification of the process leads to an optimal combination of ICP and bias inducing RF powers (50 and 75 W, respectively), which resulted in straight sidewalls as shown in Fig. 4.3(b). The increase of the physical bombardment due to the higher ion energy, and the reduced chemical etching due to a lower plasma density, did not significantly alter the selectivity of the RIE process; in fact, in both cases, the gold nanodisks are still observable as brighter dots on top of the etched pillars.

It is worth noting that in all cases, we observed a reduction in the diameter of the metallic nanodisks overlying each pillar following the etch. SEM images are presented in Fig. 4.4, which shows 50 nm period AG lattices patterned for different etching times, from 60 to 110 s, using the optimized etch process. The height of the

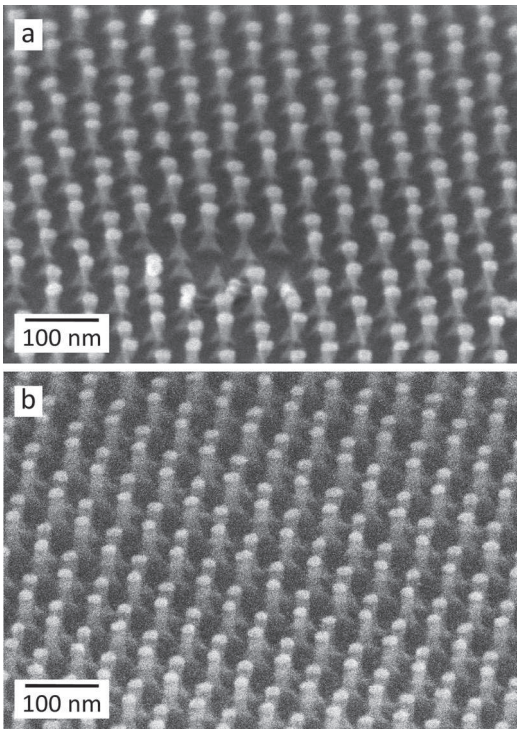


Figure 4.3: SEM micrographs (65° tilt) of AG lattices (QW sample # L06-27-14.1) with 50 nm period for different etch conditions (disk diameter 20 nm; pillar height 60 nm. Gas mixture: 50 sccm Ar, 5 sccm $BCl_3$; chamber pressure 3.7 mbar). (a) RF power (RF2) = 50 W; ICP RF power (RF1) = 75 W. (b) RF2 = 75 W; RF1 = 50 W.

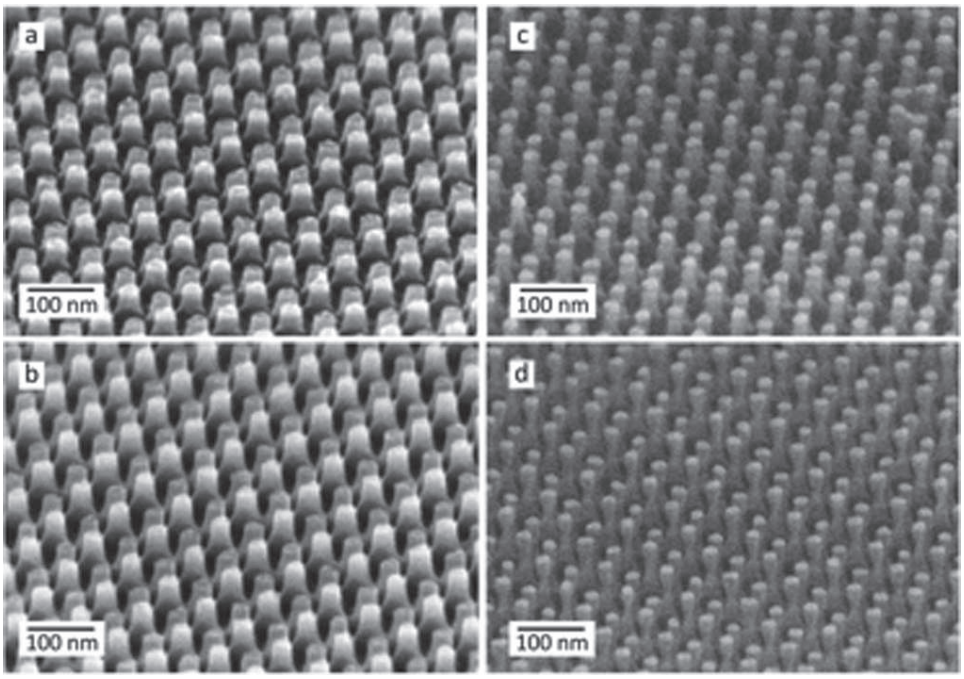


Figure 4.4: SEM micrographs (65° tilt) of artificial graphene lattices (QW sample # L06-27-14.1) with 50 nm period for different etch times. (a) 60 s (etch depth = 45 nm); (b) 80 s (etch depth = 55 nm); (c) 95 s (etch depth = 62 nm); and (d) 110 s (etch depth = 75 nm). In (c) and (d), the metal mask is still present; this was taken into account for the evaluation of the depth of the etch. The sidewall profile is almost vertical in all cases; only the deepest etch presents a certain degree of undercut. The AG lattice in (d) was etched to within 5 nm from the Si doping layer, which constitutes the limit.

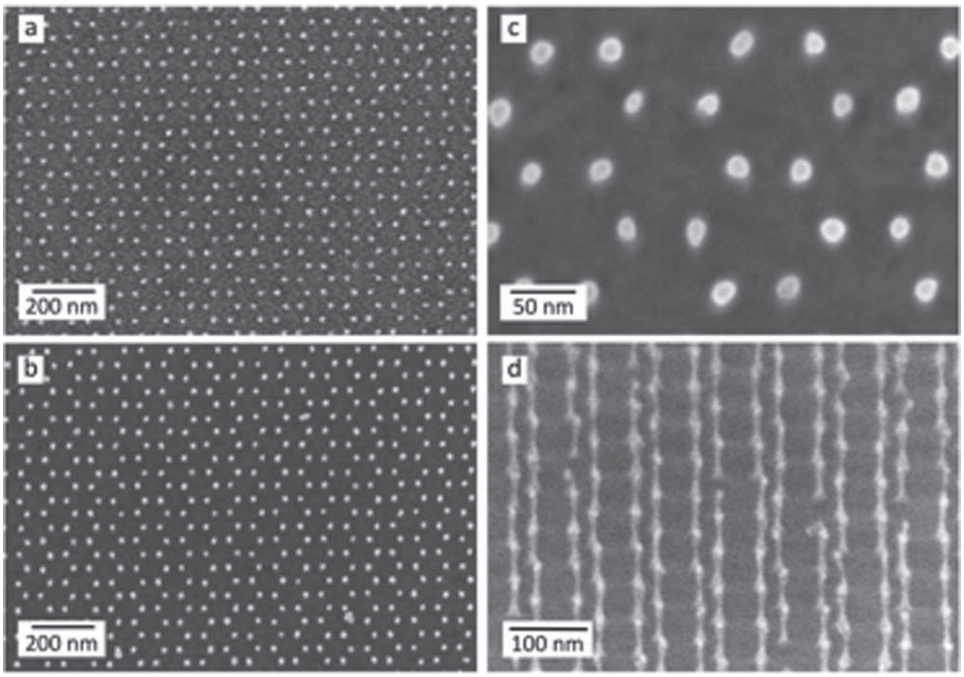


Figure 4.5: (a) SEM image of a 40nm pitch honeycomb array of gold nanodisks obtained using the metal hard-mask method. (b) The same sample after annealing at 450°C for 2 h. The edge roughness of the Au disks noticeably improves. (c) Detail of the mask after annealing. The disk diameter is approximately 15nm. (d) The resulting AG lattice after a 50nm-deep etch with the optimized process (the metal mask is still present). The average width of the pillars isabout 10nm, resulting in an aspect ratio of 5. (QW sample # L06-27-14.1)

pillars determines the intensity of the effective periodic potential and the final degree of modulation of the electron density of the 2DEG; therefore, it is important to control the etch depth with nanometer accuracy. For 110 s etch time, shown in Fig. 4.4(d), the measured depth was about 75 nm, only 5 nm above the Si d-doping layer. This should give the strongest potential modulation and well-defined AG minibands with linear dispersion. The verticality of the etch profile decreases with increasing etch time; nevertheless, the mechanical stability of the pillars appears to be unaffected. The aspect ratio of the fabricated pillars in Fig. 4.4(d) is 3.5.

As noted above, the challenges related to proximity effects and the reliability of the lift-off can be managed using the hard mask method we described here. The hard mask actually allows a slight underexposure of the honeycomb pattern, resulting in minimal broadening of the features, increasing the process window and the ultimate resolution achievable. The $O_2$ plasma etching process produces an undercut in the resist that eases the lift-off. Furthermore, the complete removal of the resist residue and the hydrophilization of the surface facilitate the adhesion of the metal, promoting defect-free arrays with excellent long range order. A disadvantage of the hard mask method is an increase in the edge roughness of the metal nanodisks, resulting from the irregularity of the grains of the metal coating the border of the developed resist features. This can affect the uniformity of the lattice, as can be seen in Fig. 4.5(a) for a 50 nm period array. One possible way to overcome this drawback is to anneal the sample, causing each metal disk to melt and form a smoother droplet, as displayed in Figs. 4.5(b-c), in which case the annealing has been performed on a hot plate at 450 °C for 2 h. Another consequence of the use of a metal hard mask and high temperature annealing is that the nanodisks are smaller. The hard mask in fact narrows the diameter of the apertures, and the annealing turns disks into nanoparticles, shrinking their in-plane cross-section. This method can be used to achieve very narrow pillars, as can be seen in Fig. 4.5(d), where the average width is about 10 nm, with an aspect

ratio of 5.

## 4.4 Summary

High resolution electron beam lithography and reactive ion etching were used to create artificial honeycomb lattices with lattice constants as small as 40 nm on GaAs/AlGaAs quantum wells hosting a two dimensional electron gas. The aim is to replicate in a tunable manner the massless Dirac fermion physics which is a hallmark of graphene. The use of bilayer PMMA, metal deposition, and lift-off enables the achievement of patterns with high resolution, excellent uniformity, and long range order. By performing a postdevelopment oxygen plasma descum protected by a metal hard mask, and postprocessing annealing of the etch mask, it is possible to obtain AG lattices with higher aspect ratio. The optimized etch process yields nearly vertical sidewalls, with no evidence of pillar collapse. By probing the electron states of these devices, we expect to be able to observe for the first time a graphenelike band structure in an artificial semiconductor lattice.

Part of the results presented in this chapter are published in Ref.[80].

# Chapter 5

# Electronic Band Structures of AG Lattices in GaAs QWs

## 5.1 Introduction

Electrons moving in a periodic potential can be described by Bloch wavefunctions[81]. Thus we can create artificial crystals to manipulate electron states. Calculations of electron band structures in artificial lattices with different potential configurations, such as lattice symmetry, lattice constant and potential magnitude, can provide insights for fascinating physics such as massless Dirac fermions (MDFs).

Charge carriers in graphene may have a unique linear energy-momentum dispersion [1, 2, 4], which arises from the symmetry of the honeycomb lattice. MDFs can be described by relativistic Dirac equations and exploration of MDF physics attracts great interest. To replicate MDFs in a highly tunable manner, nano-patterned semiconductor with honeycomb topology has been proposed [12–14, 38–40].

This chapter presents evaluations of electron band structures of honeycomb lattices on nano-patterned GaAs QWs. The calculations confirm that linear energy-momentum dispersion are realized around the Dirac cones at the K and K' points of

the Brillouin zone. The parameter space for creating well-developed Dirac cones is analyzed and the energy range of linear dispersion is also discussed here. In order to interpret experimental results presented in Chapter 6, we consider here the DOS and JDOS defined in Subsection 2.2.2 for transitions between different AG bands. The parameters used in the analysis are based on experimental realizations and the results provide key insights for the design of nano-patterns that manifest intriguing physics that emerges in artificial graphene lattices.

## 5.2 Modeling of AG Lattices in GaAs QWs

The potential modulation in nano-patterned GaAs QWs created by shallow etching is provided by periodic electrostatic potential given by the non-screened ionized donors [82] as shown in Fig. 5.1(a).

Such periodic electrostatic potential in the QW does not have a simple analytic form, so we use a simplified model for the purpose of calculating AG band structures. I use a periodic muffin-tin potential: it has a constant value $V_0$ under the pillars arranged in a honeycomb lattice pattern and has a value of zero outside the pillars as shown in Fig. 5.1(b). The radius of the potential circles is $r$. Due to the surface states on the side walls of the pattern, $r$ is smaller than the radius of AG pillars $r_0$. The distance between adjacent pillars is $a$. This model is simple yet powerful and was used in the previous studies[13, 38] with excellent results. Other forms of potential such as triangular lattice muffin-tin potential[12] and potential described by smooth functions[39] give similar band structures. A more realistic potential should be smooth near the boundaries of the pillars as schematically depicted in Fig. 5.1(c). The most important aspect for calculations of AG band structures is the lattice symmetry instead of exact potential. The AG band structures and conclusions of my calculations remain qualitatively valid regardless the exact form of potential being

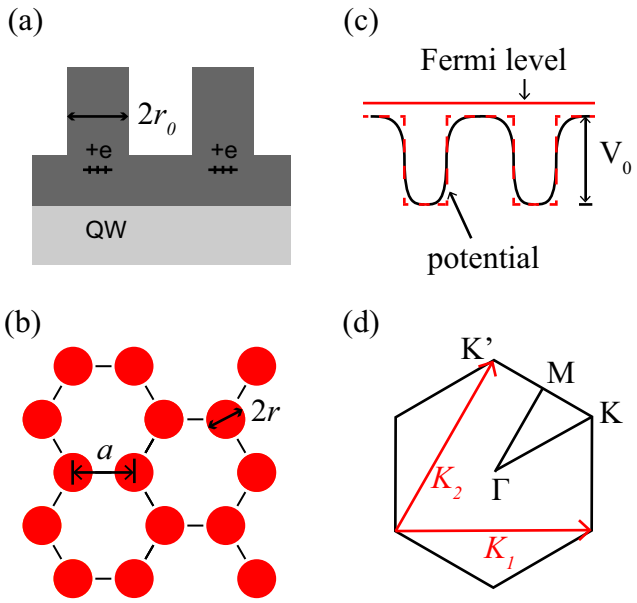


Figure 5.1: (a) Schematic of AG pillars showing ionized donors which provide periodic electrostatic potential in the QW. (b) Muffin-tin potential arranged in honeycomb lattice. (c) A more realistic potential for our AG systems indicated by black solid line. It is smoother than Muffin-tin potential indicated by red dashed line. (d) The Brillouin zone of honeycomb lattice. High symmetry points Γ, K and M are labeled. $\vec{K_1}$ and $\vec{K_2}$ are reciprocal lattice vector basis.

employed. Fig. 5.1(d) shows the Brillouin zone and reciprocal lattice vectors for the honeycomb lattice.

Within the envelope wavefunction approximation[46], or effective mass approximation, the electrons in GaAs QW under periodic muffin-tin potential $V(\vec{r})$ can be described in a single particle approximation as:

$$(-\frac{\hbar^2}{2m_e}\nabla^2 + V(\vec{r}))\psi(\vec{r}) = E\psi(\vec{r}) \tag{5.1}$$

$$V(\vec{r}) = \begin{cases} V_0 & \text{if there exists } \vec{R} \text{ such that } |\vec{r} - \vec{R}| < r \\ 0 & \text{elsewhere} \end{cases} \tag{5.2}$$

where $m_e = 0.067m_0$ is the effective mass of electrons in GaAs with $m_0$ being the rest mass of electron. $\psi(\vec{r})$ is the wavefunction of electrons and $\vec{r}$ is position vector in the plane of 2D electron gas. $\vec{R}$ is the Bravais lattice vector in real space. Using Bloch's theorem, the wavefunction can be written as combination of plane wave functions,

$$\psi_{\vec{k}}(\vec{r}) = \sum_{\vec{K}} c_{\vec{k}-\vec{K}} e^{i(\vec{k}-\vec{K})\cdot\vec{r}} \tag{5.3}$$

and Eq. 5.1 can be written as:

$$(\frac{\hbar^2}{2m_e}(\vec{k} - \vec{K})^2 - E_{\vec{k}})c_{\vec{k}-\vec{K}} + \sum_{\vec{K}'} V_{\vec{K}'-\vec{K}} c_{\vec{k}-\vec{K}'} = 0 \tag{5.4}$$

$$V(\vec{r}) = \sum_{\vec{K}} V_{\vec{K}} e^{i\vec{K}\cdot\vec{r}} \tag{5.5}$$

where $\vec{K}$ and $\vec{K}'$ are reciprocal lattice vectors. All reciprocal lattice vectors $\vec{K}$ can be described as $\vec{K} = n_1\vec{K}_1 + n_2\vec{K}_2$ with $n_1$, $n_2$ being integers, and $\vec{K}_1$, $\vec{K}_2$ being the reciprocal lattice vector basis shown in Fig. 5.1(d)[81]. Solving Eq. 5.4, it is equivalent to solve the eigenvalues and eigenvectors of the Hamiltonian matrix:

$$det||(\frac{\hbar^2}{2m_e}(\vec{k} - \vec{K})^2 - E_{\vec{k}})\delta_{\vec{K},\vec{K}'} + V_{\vec{K}'-\vec{K}}|| = 0 \tag{5.6}$$

In principle we need to consider an infinite number of reciprocal lattice vectors $\vec{K}$ in Eq. 5.6. However we are only interested in the first several electron bands, where the linear dispersion happens. A finite number of $\vec{K}$ can be used to get accurate results for the lowest few bands (48 $\vec{K}$ are used in my calculations). To give an idea of how to construct this Hamiltonian matrix, I list the first seven $\vec{K}$ used in my calculations labeled as $\vec{K}^n$:

$$\begin{cases} \vec{K}^1 &= \frac{4\pi}{3\sqrt{3}a}(0,0) \\ \vec{K}^2 &= \frac{4\pi}{3\sqrt{3}a}(\sqrt{3},0) \\ \vec{K}^3 &= \frac{4\pi}{3\sqrt{3}a}(\sqrt{3}/2,3/2) \\ \vec{K}^4 &= \frac{4\pi}{3\sqrt{3}a}(\sqrt{3}/2,-3/2) \\ \vec{K}^5 &= \frac{4\pi}{3\sqrt{3}a}(-\sqrt{3}/2,3/2) \\ \vec{K}^6 &= \frac{4\pi}{3\sqrt{3}a}(-\sqrt{3}/2,-3/2) \\ \vec{K}^7 &= \frac{4\pi}{3\sqrt{3}a}(-\sqrt{3},0) \end{cases} \tag{5.7}$$

The off diagonal elements of Hamiltonian matrix can be calculated as the Fourier components of the AG potential, and they have analytic form for muffin-tin potential:

$$V_{\vec{K}} = V_0 \cdot \frac{8\pi}{3\sqrt{3}} cos(\vec{K}_x a/2) J_1(|\vec{K}|r) \frac{r}{|\vec{K}|a^2} \tag{5.8}$$

where $\vec{K}_x$ is the $x$ component of $\vec{K}$ and $|\vec{K}|$ is the magnitude of $\vec{K}$. $J_1(x)$ is the first-order Bessel function. $r$ is the circle radius and $a$ is the distance between neighboring circle centers. The Matlab code (see Appendix C) is used to calculate the Hamiltonian matrix and to solve Eq. 5.6.

## 5.3 Results and Discussion

### 5.3.1 Impact of the Size of the Basis

To investigate the accuracy of my calculation, first I consider the impact of using a finite plane wave basis. The first three bands are calculated by using different number of basis as shown in Fig. 5.2. The minimum of the first electron band is shifted to zero for comparison. It is easy to see that the calculations converge with 18 plane waves. The band structures calculated with 18 basis and 48 basis are almost identical as shown in Fig. 5.2(d). In subsequent calculations, 48 plane wave basis are used to ensure accuracy.

One note about choosing the basis is that we need to preserve symmetry for the set of basis used in the calculation. It means all degenerate states at K and K' points should be included for solving the eigenvalue problem. Otherwise the electron bands may have a band gap at K and K' points due to calculation errors from inappropriate set of plane wave basis.

### 5.3.2 Impact of Potential Period, Radius, and Magnitude on AG Band Structures

The energy scale of electron bands of AG lattices can be characterized by the free electron kinetic energy at the corners of the Brillouin zone, which is $8\pi^2\hbar^2/(27m_e a^2) \propto 1/a^2$, so reducing lattice constant will enlarge the energy scale of electron band structures. The electron band structures for different lattice constants are shown in Fig. 5.3. The energy range of linear dispersion near the K points increase an order of magnitude from $a = 130$ nm to $a = 40$ nm. Since we have achieved AG lattices with $a = 40$ nm as discussed in Chapter 4, I will focus most of my calculations on AG lattices with $a = 40$ nm.

If the linear dispersion energy range around Dirac cones are too small, the effects

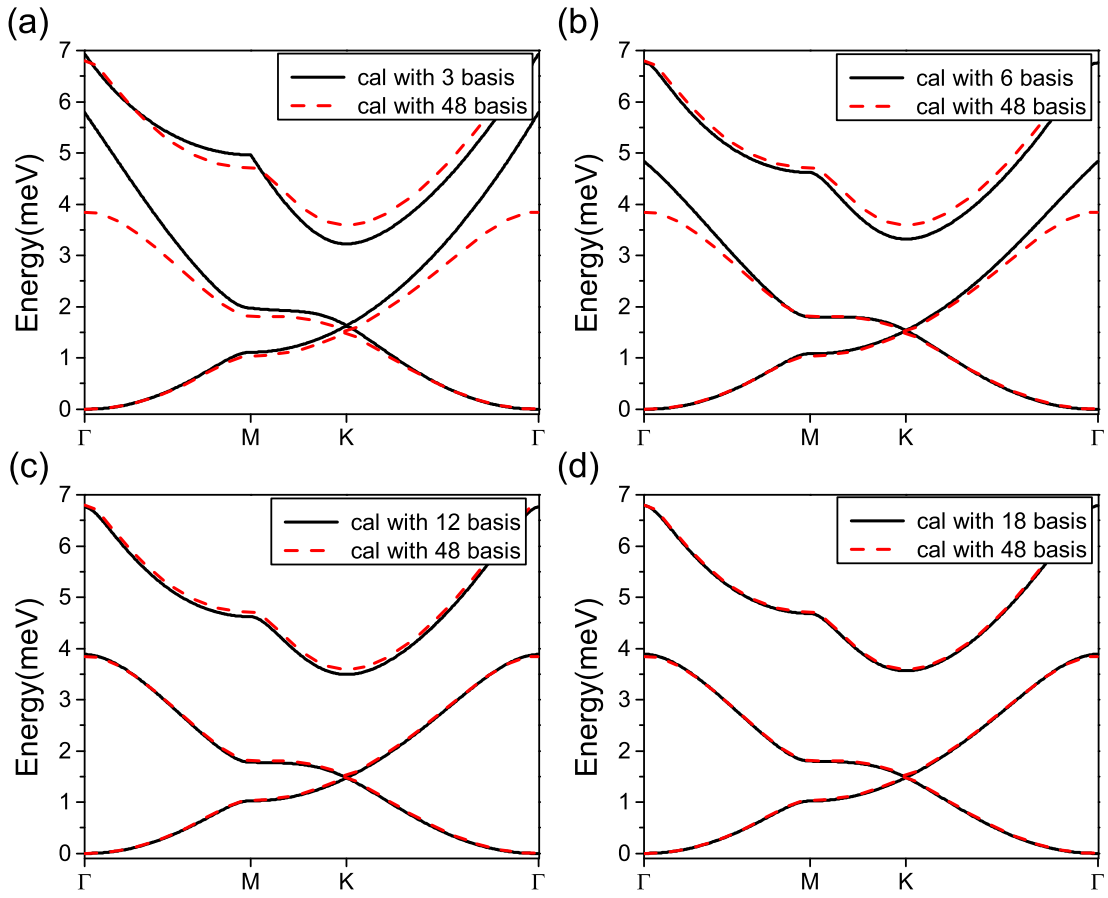


Figure 5.2: The impact of finite number of plane waves basis used in the calculation of electron bands. The number of plane wave in the basis used in each calculation is (a)3, (b)6, (c)12 and (d)18. The electron bands calculated with 48 plane wave basis are plotted as red dashed lines for reference. The calculation converges with 18 plane wave in the basis, the band structures calculated with 18 basis and 48 basis are almost identical. The parameters are $a = 40$ nm, $r = 12$ nm, $V_0 = -6.0$ meV.

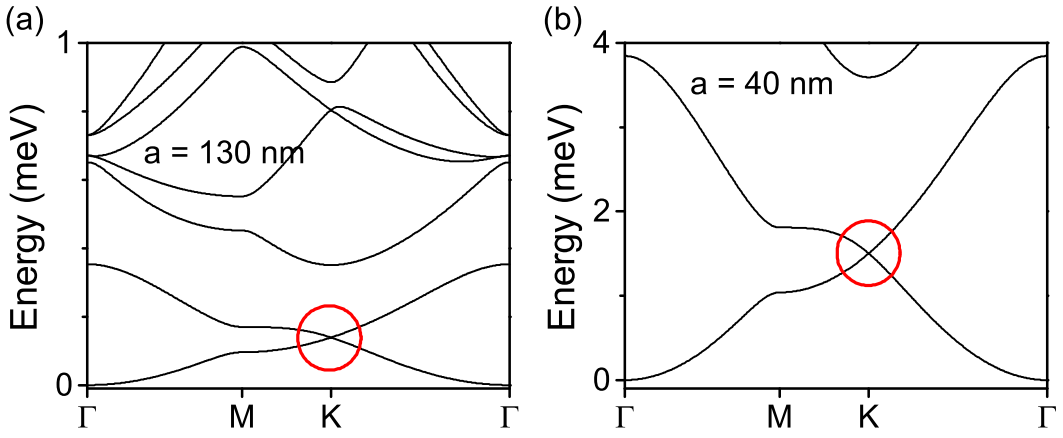


Figure 5.3: Electron band structures calculated for two different lattice constants. The linear dispersion regions around Dirac cones are highlighted by red circles and it has significantly increased from $a = 130$ nm to $a = 40$ nm. The parameters used in the calculations are (a) $a = 130$ nm, $r = 39$ nm, $V_0 = -0.6$ meV, (b) $a = 40$ nm, $r = 12$ nm, $V_0 = -6.0$ meV.

might be washed away by broadening effects. For example, at a temperature of 4.2 K, the thermal broadening is roughly $k_BT \approx 0.4$ meV. In order to get a linear dispersion range of 0.4 meV, the lattice constant needs to be around 40 nm with a potential depth larger than 5 meV. Other broadening effects from nano-fabrication and random distribution of ionized donors can still come into play. Thus in order to successfully observe AG band structures, it requires QW with minimal defects and fabrication protocals that yield patterns with high uniformity.

We limit our discussions of Dirac cones to the first two AG bands for simplicity. Pinning the Fermi level to Dirac cones will need two electrons per unit cell, corresponding to an electron density of $2/(3\sqrt{3})a^{-2}$. For AG lattices with $a = 40$ nm, the required areal electron density is $6.2 \times 10^{10}$ cm$^{-2}$, which is typical in our experiments.

To study Dirac physics, we seek to have only linearly dispersed electron states in the states close to the Fermi level. To create such isolated Dirac bands, we require values of the appropriate radius $r$ and the potential depth $V_0$.

First we consider the appropriate range for the potential depth $V_0$. Electron bands with different potential are calculated in Fig. 5.4. The lattice constant and radius used in the calculation are parameters achieved in experiment: $a = 40$ nm and $r = 8.0$ nm. Fig. 5.4(a) is the empty lattice case, and AG bands are just parabolic bands folded in the reciprocal space of AG lattices. At a potential depth of $V_0 = -4$ meV a Dirac cone is formed as shown in Fig. 5.4(b), however it is not isolated because there are other states with same energy indicated by the horizontal dashed line. If the Fermi level is at the Dirac cone point, there will be mixed states of massless electrons and massive electrons. With $V_0 = -10$ meV, an isolated Dirac cone is well-developed as shown in Fig. 5.4(c).

To monitor the emergence of isolated Dirac cones, and a linear dispersion range, we study as a "figure of merit" the energy difference between states at M point and at K point of the second AG band[38]. This energy difference labeled $\Delta E_M$ is shown in

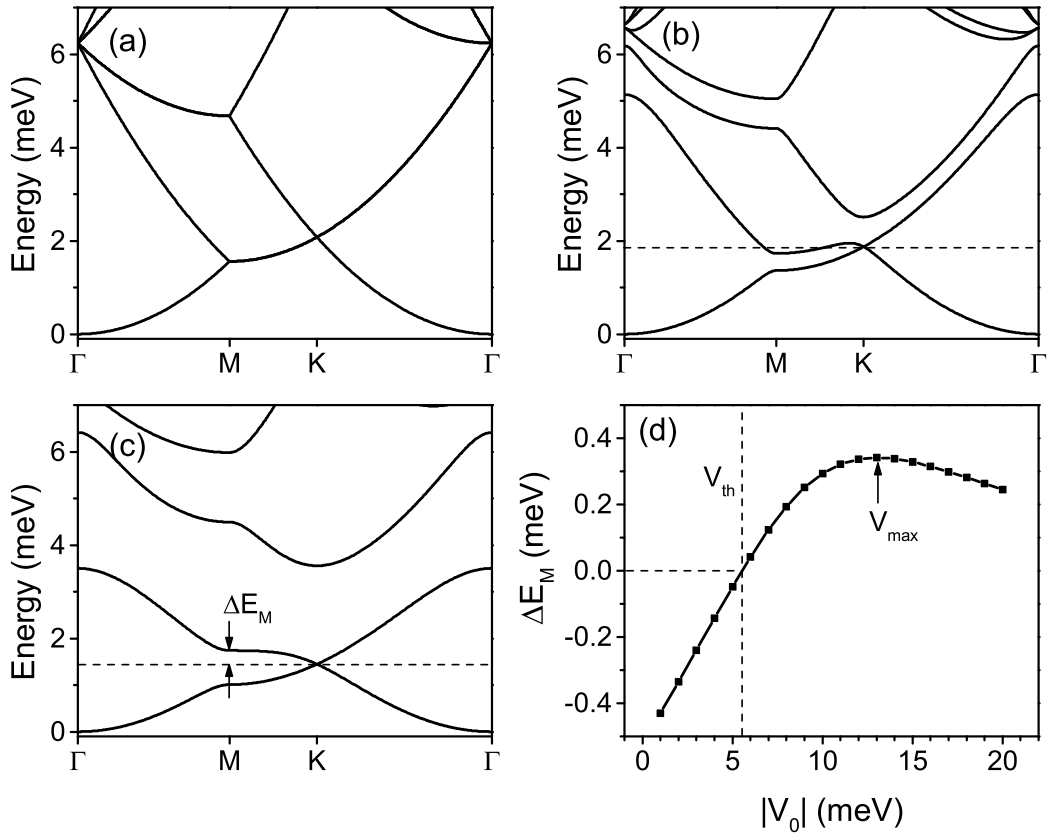


Figure 5.4: Calculated AG bands for $a = 40$ nm, $r = 8.0$ nm with different potential depth $V_0$ (a) $V_0 = 0$ meV, (b) $V_0 = -4$ meV and (c) $V_0 = -10$ meV. Energy gap at M point $\Delta E_M$ (see text) is indicated in (c). (d) $\Delta E_M$ as a function of potential depth $|V_0|$. $\Delta E_M$ can approximately represent the linear dispersion range. The threshold potential to have isolated Dirac cones, corresponds to positive $\Delta E_M$, is $V_0 = V_{th} = -5.5$ meV. At $V_0 = V_{max} = -13$ meV, $\Delta E_M$ reaches its maximum.

Fig. 5.4(c). Isolated Dirac cones are formed when $\Delta E_M$ is positive, and $\Delta E_M$ is also a good estimate for the linear dispersion range in the Dirac cones. Fig. 5.4(d) shows the calculated values of $\Delta E_M$ as function of the potential depth. The threshold of $V_0$ to form isolated Dirac cones, $V_{th}$, is - 5.5 meV and the maximum value of $\Delta E_M$ is reached at $V_0 = V_{max} = -13$ meV. Fig. 5.4(d) provides guidance on the range of $V_0$ that yields well-developed Dirac cones.

Values of $\Delta E_M$ have a crucial dependence on the quantum dot radius $r$ as shown in Fig. 5.5. It is worth pointing out that the radius used in modeling is actually smaller than the physical radius of pillars due to surface states on the side walls. In order to be consistent between AG lattices with different periods, we use the ratio of radius over lattice constant:

$$\text{ratio} = r/a \tag{5.9}$$

as the horizontal coordinate in Fig. 5.5. As we can see, isolated Dirac cones are formed above the $\Delta E_M = 0$ horizontal line. This implies that for fixed potential used here ($V_0 = -6$ meV), the threshold ratio is 0.19 to form isolated Dirac cones.

A complete map of $\Delta E_M$ as a function of potential depths and ratios for AG lattices with $a = 40$ nm is plotted in Fig. 5.6. Different colors represent different magnitude of $\Delta E_M$. The red dashed line indicates the threshold parameters required to form isolated Dirac cones. On the upper right side of the red dashed line, isolated Dirac cones are formed while there are no isolated Dirac cones on the bottom left side. Since the potential magnitude can experimentally achieve the as-grown Fermi energy (about 6 meV in our sample)[36, 37], it requires a threshold ratio of 0.19 to form isolated Dirac cones. A large ratio such as 0.35, which should be experimentally desirable, will provide a reasonable large linear dispersion range (about 0.4 meV).

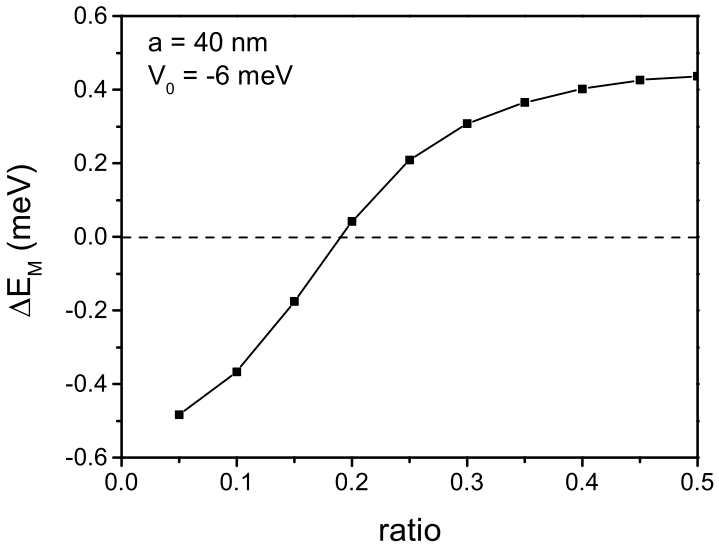


Figure 5.5: Evaluation of $\Delta E_M$ at different ratios for $a = 40$ nm and $V_0 = -6$ meV. Isolated Dirac cones are formed above the horizontal line $\Delta E_M = 0$ indicated in the figure.

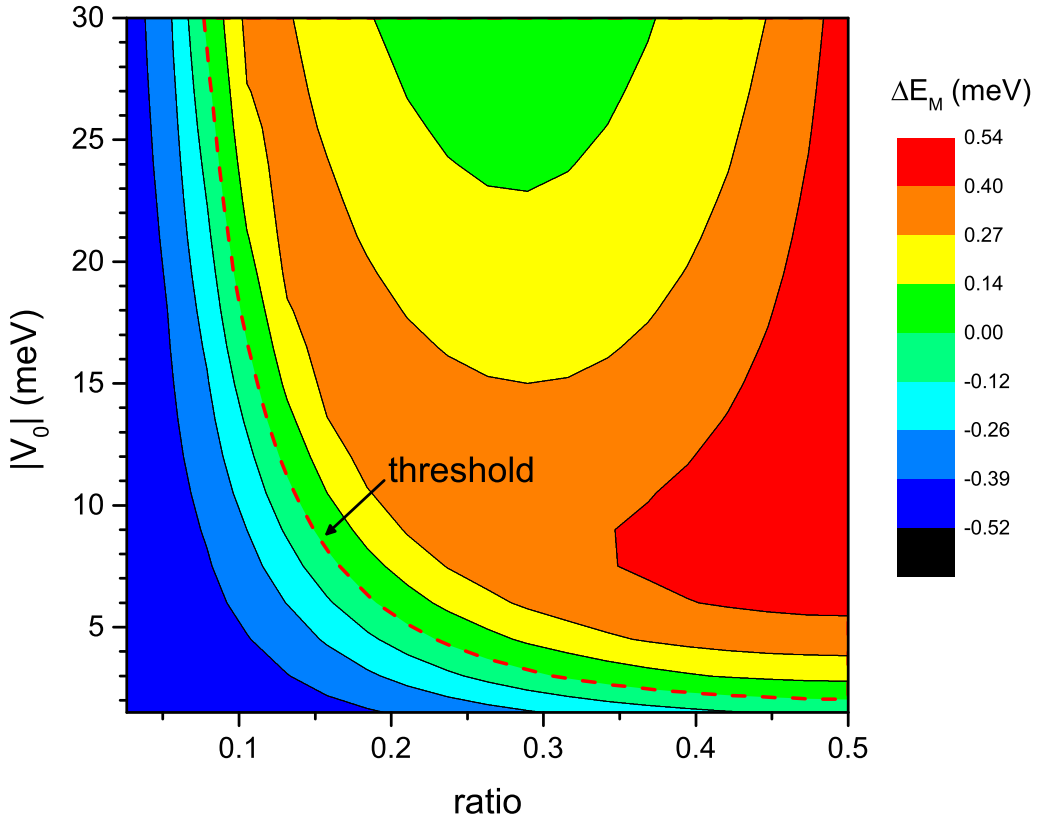


Figure 5.6: Map of $\Delta E_M$ at different ratios and potential depth for AG lattices with $a = 40$ nm. The threshold to form isolated Dirac cones is indicated by the red dashed line denoting the boundary $\Delta E_M = 0$.

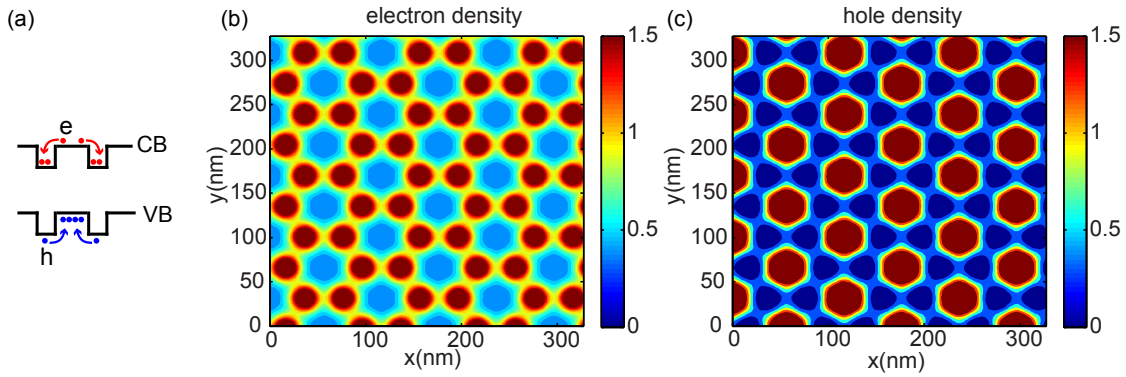


Figure 5.7: (a)Illustration of spatial separation of electrons and holes in the AG lattices. The electrons, denoted by the red circles, accumulate in the positions of the pillars, while holes, denoted by the blue circles, accumulate outside of the pillars. The ground state areal density is calculated for (b) electrons and (c) holes from an AG lattice with $a = 40$ nm, $V_0 = -6$ meV and ratio $= 0.25$.

### 5.3.3 Spatial Separation of Electrons and Holes

Another consequence of the AG potential is that spatial distributions of electrons and holes are modified. Due to different charge types of electrons and holes, they are spatially separated as shown in Fig. 5.7(a). Electrons will be attracted under AG pillars while holes will be repelled away by such pillars. A typical spatial distribution of electrons and holes is shown in Fig. 5.7(b)(c). The electron and hole density is normalized to the uniform distribution case. We can clearly see the accumulation of electrons under pillars and the opposite case for hole.

A careful comparison of distributions of electrons and holes reveals a stronger localization for holes. This is in contradiction to the intuition that electrons should be more localized because AG pillars are separated while etched regions are connected. A simple explanation to this contradiction is the different effect masses of electrons and holes. Since heavy holes have much larger (a factor of 7) effective mass ($0.45m_0$) than electrons ($0.067m_0$), the kinetic portion in Hamiltonian is smaller for heavy holes. Thus the hole wavefuction does not extend far into potential barrier.

Due to this spatial separation of electrons and holes, the overlap between electron and hole envelop functions is reduced. Thus the optical emission at the bottom of the conduction band in the AG lattices has diminished intensity. This spatial indirect transitions should be considered in the determination of band gap though optical emission in Chapter 6[29, 30].

### 5.3.4 DOS and JDOS of AG Band Structures

DOS and JDOS have been discussed in Subsection 2.2.2 for parabolic band structures (Eq. 2.17) and linearly dispersed band structures (Eq. 2.21). This section will evaluate the DOS and JDOS of calculated AG band structures.

Figure 5.8 shows the calculated DOS of AG lattices with $a = 40$ nm, $V_0 = -6.1$ meV, and two ratios: 0.17 and 0.30. The reason to use two different ratios

is to compare the DOS between mixed states around Dirac cone and isolated, well-developed Dirac cone. For AG lattice with a ratio of 0.17, there are mixed states around the energy of Dirac cone, so the DOS does not reduce to zero as see in Fig. 5.8(a). The DOS does not change linearly with energy above the Dirac cone, which indicates the Dirac cone is not well-developed. The DOS also has a large portion of constant value, which is similar to the DOS of 2D free electron. In contrast, the AG lattice with a ratio of 0.3 has isolated and well-developed Dirac cones as seen in Fig. 5.8(d). In consequence the DOS reduces to zero at the energy of Dirac cone and change linearly with energy. By changing the Fermi level via gating, experiments measuring DOS, such as conductance measurements, can provide direct evidences of MDFs.

Using RILS methods introduced in Chapter 3, we are able to detect the formation of AG miniband structures optically. Different types of transitions involving AG miniband structures are possible.

Fig. 5.9 discusses inter-AG-band transitions and intersubband transitions from AG lattices. Inter-AG-band transitions are direct transitions with change in AG band index and no change in QW subband index. The initial and final states of the electron are both in the first (lowest) subband of the QW that supports the AG lattices. In intersubband transitions there is a change in QW subband. There are also "combined" intersubband transitions in which there is also a simultaneous change in AG band index. The initial and final states are in the first and second subband of the QW respectively. Combined intersubband excitations do not exist on the as-grown GaAs QWs.

Electron bands calculated with periodic muffin-tin model are labeled by two indexes in sequence, subband index and AG band index. The two index count from the lowest band starting from zero. For example, the first AG band in the ground subband is $c_{00}$ and the first AG band in the second subband is labeled as $c_{10}$. Inter-

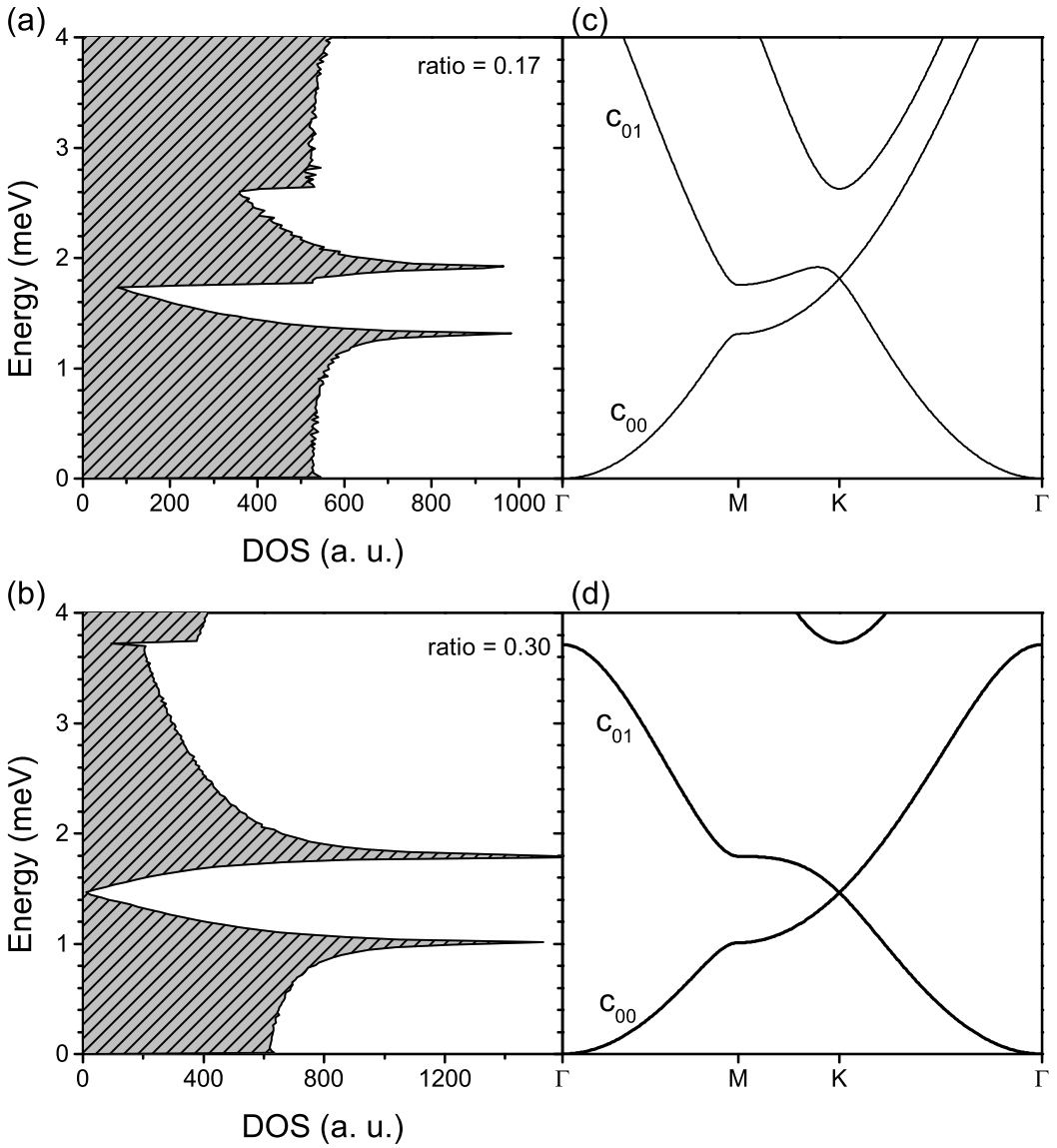


Figure 5.8: DOS of AG band structures for $a = 40$ nm, $V_0 = -6.1$ meV, (a) ratio = 0.17 and (b) ratio = 0.30 (ratio defined in Eq. 5.9). The corresponding AG bands are in (b) and (d). The AG lattice with ratio = 0.17 does not have an isolated Dirac cone as seen in (c), thus the DOS does not reduce to zero and shows non-linearity around the energy of the Dirac cone as seen in (a). In contrast, the AG lattice with ratio of 0.30 has an isolated, well-developed Dirac cones, and the DOS diminished linearly to zero around the energy of the Dirac cone shown in (b)(d).

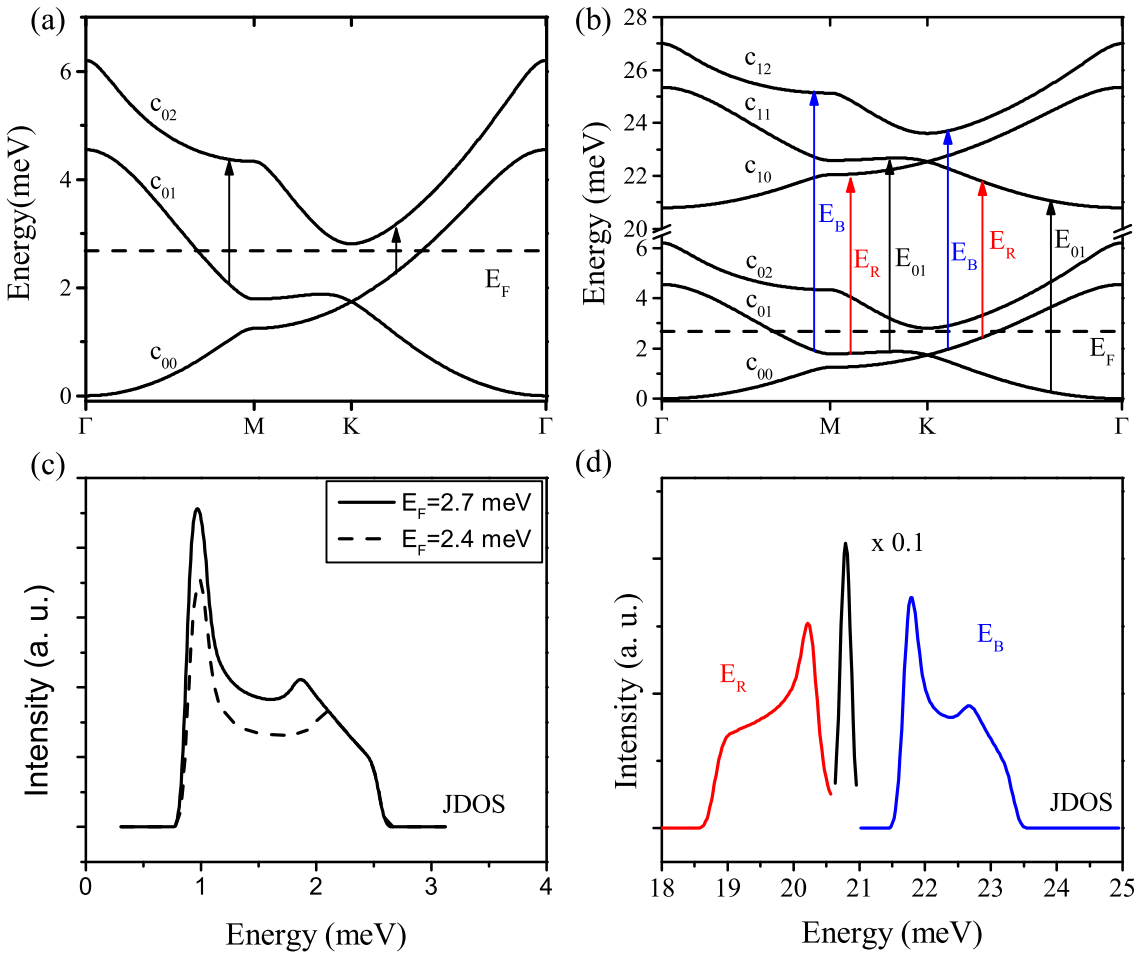


Figure 5.9: (a) Schematic description of transitions between AG minibands. (b) Schematic of intersubband transitions involving AG minibands. JDOS of transitions indicated in (a) and (b) are calculated in (c) and (d) respectively. The parameters used in modeling are: $a = 40$ nm, $r = 8.0$ nm, $V_0 = -6.1$ meV, $E_F = 2.7$ meV except in (c) where JDOS with $E_F = 2.4$ meV is also calculated. Transitions directly between AG minibands can be seen in (a) and (c), while AG lattices will result several satellite peaks in intersubband transitions illustrated in (b) and (d).

AG-band transitions, transitions between AG minibands in the same subband, are only involving the first subband while intersubband transitions involve the first two subbands. In Fig. 5.9, parameters used in the modeling are close to those in our samples: $a = 40$ nm, $r = 8.0$ nm, $V_0 = -6.1$ meV, and $E_F = 2.7$ meV. Only vertical transitions are considered here as the in-plane momentum transfered from photons is negligible in our experiment setup.

Figure 5.9(a) illustrates transitions between AG minibands. Electrons from states below Fermi level are excited to states above the Fermi level, as indicated by vertical arrow from $c_{01}$ to $c_{02}$. In a simplified description, the transition intensity is proportional to the JDOS between these two bands. Transitions from $c_{00}$ to $c_{02}$ are also possible, however they do not form sharp peaks due the small JDOS between these oppositely dispersed bands. On the other hand, AG bands $c_{01}$ and $c_{02}$ are nearly parallel and contribute large JDOS with sharp peaks.

Fig. 5.9(c) displays the calculated JDOS related to the transitions indicated by vertical arrows in Fig. 5.9(a). In the JDOS we can clearly identify a sharp peak formed around 1.0 meV and a broad continuum with maximum around 1.9 meV. The reciprocal space for allowed transitions between $c_{01}$ and $c_{02}$ is determined by the Fermi level, thus the lineshape of the JDOS will depend on Fermi energy. The JDOS with a different Fermi energy, $E_F = 2.4$ meV, is shown as the dashed line for comparison with the JDOS with $E_F = 2.7$ meV. Besides the reduced intensity, the peak originally around 1.9 meV shifts to higher energy at 2.1 meV, showing a large impact of the Fermi energy on the lineshape of the JDOS. Optimization of AG band structures can give the best fit between JDOS and experimental data, and it is discussed in Subsection 5.3.5.

Combined intersubband transitions provide direct evidence for the formation of AG miniband structures, and they also allow additional transitions that are not possible in inter-AG-band transitions. Figure 5.9(b) shows possible transitions involving

the first two subbands, and corresponding JDOS are calculated in Fig. 5.9(d). Transitions involving same AG band index, indicated by black arrow in Fig. 5.9(b), have a large JDOS as shown in Fig. 5.9(d). Transitions from lower AG band index to higher AG band index, indicated by blue arrow in Fig. 5.9(b), appear as blue shift satellite peaks on the JDOS as shown in Fig. 5.9(d). A close observation reveals that the shape of this blue shifted peaks $E_B$ is identical to the one from inter-AG-band transitions as shown in Fig. 5.9(c). However the energy is shifted by the $E_{01}$, the energy difference between the first two subbands. *Transitions from higher AG band index to lower AG band index, which are not allowed in inter-AG-band transition, are labeled by red arrows in Fig. 5.9(c).* These transitions, from $c_{01}$ to $c_{10}$, contribute to the red shift peak $E_R$ in JDOS as shown in Fig. 5.9(d), and provide powerful tool to probe electron states in the AG lattices.

### 5.3.5 Optimization of AG Band Structures

The JDOS functions provide an excellent tool to interpret RILS spectra involving AG band structures. In a simplified description, RILS spectra involving AG bands are proportional to the JDOS between these bands. The calculation of JDOS is based on the AG band structures, thus is determined by the parameters used in the muffin-tin potential model. A rough estimate of these parameters is obtained through experimental results, but fine-tuning such parameters will give the best fit between JDOS and RILS spectra.

Figure 5.10 shows the optimization of parameters in the AG lattice for the best fit of the RILS spectra with the JDOS. In Fig. 5.10(a), the upper panel displays the RILS spectra of intersubband transitions from an AG lattice with $a = 40$ nm. The strong main peak around 20.8 meV is due to intersubband excitations without a change in AG band index. The energy is due to confinement in the QW, interpreted as $E_{01}$ in Fig. 5.9(b). The full scale of peak $E_{01}$ is not displayed here to better show

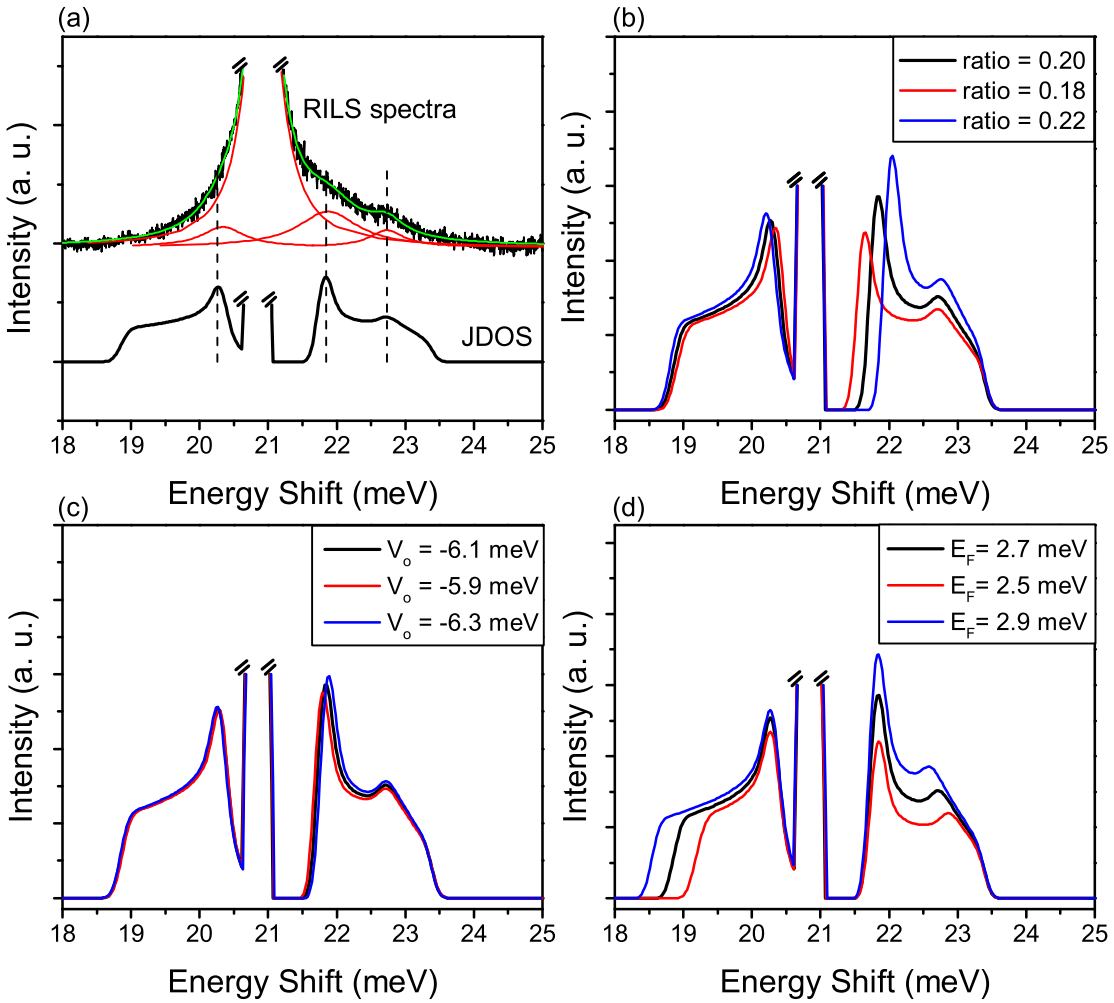


Figure 5.10: Optimization of AG band structures to fit the RILS spectra. (a) RILS spectra of intersubband transitions in parallel polarization configuration from an AG lattice with $a = 40$ nm. The RILS spectra are fitted by multiple Lorentzian-shape peaks to identify the energy positions of satellite peaks. The JDOS in the lower panel is from optimized AG band structures to match the energy positions of satellite peaks in the RILS spectra. The agreement between JDOS and RILS spectra is very good. The parameters used in the calculation of the JDOS are: $a = 40$ nm, ratio $= 0.20$, $V_0 = -6.1$ meV, and $E_F = 2.7$ meV. The impacts of tuning parameters on JDOS are shown for (b)ratio, (c)$V_0$ and (d) $E_F$.

the satellite peaks on the shoulder, which are more interesting as they are combined excitations that involve a change of AG band index. To identify the energies of these satellite peaks, the RILS spectra are fitted by multiple Lorentzian peaks. The JDOS in the lower panel of Fig. 5.10(a), similar to the one in Fig. 5.9(d), is from the optimized AG band structures and shows excellent agreement of peak positions with the RILS spectra above. Thus these satellites peaks are well explained by the JDOS from combined transitions discussed in Subsection 5.3.4. A more detailed discussion of such intersubband transitions can be found in Subsection 6.2.2.

The impacts of tuning different parameters on the JDOS are shown in Fig. 5.10(b-d). Since the resonance enhancement of the RILS is not taken into account, we focus on the changes of peak positions of the JDOS rather than the changes of intensities. Tuning ratio $r/a$, $V_0$, or $E_F$ has different impacts on the JDOS, as the peaks located around 20.3 meV and 21.8 meV only change energies with different ratio or $V_0$ while the peak located around 22.7 meV only changes energy with different $E_F$. Equivalently a change of Fermi energy, according to this calculation, will only change the energy of the peak around 22.7 meV. Such unique dependence enables us to fit the parameters separately, resulting a more stable optimization of AG band structures.

The optimization of AG band structures not only provides an excellent agreement between the RILS spectra and the calculated JDOS, it also deeps our understanding of the AG band structures. By varying the desire of the AG lattices, such as changing the ratio or Fermi energy, the RILS spectra should display distinct features on the energies of the satellite peaks.

## 5.4 Summary

We use a simple yet powerful muffin-tin model to study electron states in AG lattices on nano-patterned GaAs QW. The accuracy and convergence are demonstrated by

changing the finite number of plane waves basis used in the calculation. Other forms of potential[12, 39] or inclusion of electron-electron[38, 40] interaction does not change our results qualitatively. Small periods of AG lattices (sub 100 nm) are required to have large linear dispersion range around Dirac cones. The impacts of potential $V_0$ and radius $r$ on AG bands are discussed and the threshold to have isolated Dirac cones is demonstrated. One result of AG lattice is the spatial separation of electrons and holes, which are discussed by calculating the density distributions of electrons and holes. DOS of non-isolated Dirac cones and isolated Dirac cones have been calculated for comparison. A direct measurement of DOS at different energies should provide evidences of MDFs. Possible transitions involving AG minibands are discussed and corresponding JDOS are calculated. The optimization of AG band structures provides the best fit between the JDOS and relevant RILS spectra. These modelings provide means to interpret our experimental spectra and also give guidance on designing optimal samples.

Topics in parts of this chapter are described in an article that submitted for publication[83].

# Chapter 6

# Formation of AG Electronic Band Structures

## 6.1 Introduction

In this chapter, I will discuss the results of optical spectroscopy measurements of the AG lattices with small lattice constants (as low as 40 nm) on nano-patterned GaAs QWs.

Optical emission is used to determine the Fermi energy of electrons in the AG lattices. A reduction of Fermi energy due to nano-patterning is clearly observed. I will present evidences of formation of AG electron band structures that are seen in RILS spectra. Intersubband transitions from the AG lattices reveal satellite peaks that are interpreted as combined electronic transitions between subbands of the QW confinement with a change in the AG band index. RILS of low-lying transitions, on the other hand, reveal transitions between different AG electron bands within the same subband. These transitions, both involving AG bands, exhibit a remarkable agreement with the predicted JDOS based on the band structure calculations for the honeycomb topology. The results offer evidence of the occurrence of the Dirac bands

and MDFs in artificial lattices on semiconductors.

The ability to create small period AG lattices in semiconductors opens new and highly tunable pathways for the exploration of fundamental condensed matter science, including access to novel topological phases in semiconductors with strong spin-orbit coupling[16].

## 6.2 Results and Discussion

We have demonstrated AG lattices on nano-patterned modulation doped GaAs QW with AG lattice constants as small as 40 nm (see Chapter 4 and Ref. [80]). In this chapter, I take advantage of this milestone to explore formation of AG electron bands in small period honeycomb lattices. Results from AG lattices with $a = 40$ nm and $a = 50$ nm are presented.

For the convenience of the reader I recall the concept of AG lattices discussed in previous chapters. Figure 6.1 describes the methods for the realizations of AG lattices in a GaAs QW. The fabricated AG lattices are superimposed on a two-dimensional electron gas confined within a 25 nm-wide one-side modulation-doped $GaAs/Al_{0.1}Ga_{0.9}As$ QW (Fig. 6.1(a)). The QW is positioned 110 nm below the surface and 30 nm below the Si $\delta$-doping layer. The as-grown electron density is $1.8 \times 10^{11}$ $cm^{-2}$, with low-temperature mobility of $3.2 \times 10^6$ $cm^2/(Vs)$. High-resolution electron beam lithography is used to create $200 \times 200$ $\mu m^2$ honeycomb arrays of metallic nano-disks, which serve as masks for etching. ICP-RIE is used to etch the samples to a depth of around 70 nm. Details of the fabrication procedure and optimization can be found in Chapter 4 and Ref.[80]. The resulting pillars are arranged in a honeycomb lattice, shown in Fig. 6.1(b). The pillars act as attractive potentials $V_0$ for electrons in the GaAs QW. Sufficiently small feature size, $a$, is necessary here because the energy scale of the band structures is proportional to $1/a^2$. Figs. 6.1(c)(d) show the

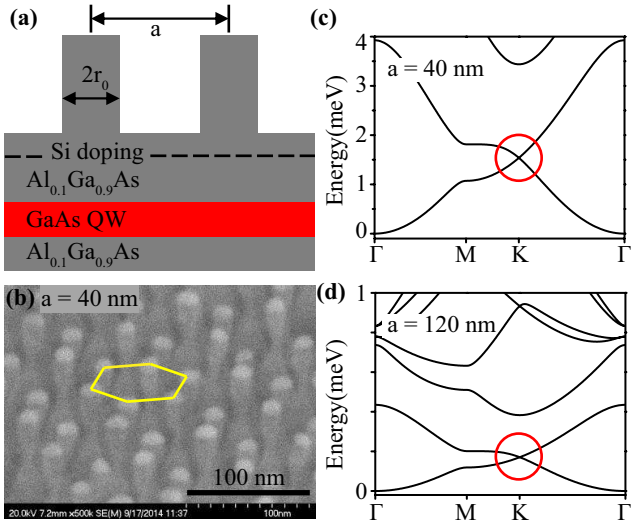


Figure 6.1: Principle of realization of artificial graphene. (a) Cross-section schematic of the nano-patterned QW sample. The radius of potential used in modeling, $r$, is smaller than the physical radius of pillars, $r_0$, indicated here. (b) SEM image of a AG pattern with $a = 40$ nm. A hexagon is drawn for eye guidance. (c)(d) Calculated AG bands for different periods (c) $a = 40$ nm, $r = 11$ nm, $V_0 = -6.0$ meV (d) $a = 120$ nm, $r = 34$ nm, $V_0 = -0.67$ meV. The Dirac cones at K and K' points are indicated by circles. For smaller period, the energy range of the linear dispersion around Dirac points is larger.

calculated AG band structures for two different lattice periods, where the energy scale increases one order of magnitude when the lattice constant decreases from $a = 120$ nm to $a = 40$ nm. The band structure calculation in Figs. 6.1(c)(d) is performed using a muffin-tin potential discussed in Chapter 5.

### 6.2.1 Optical Characterization of the Fermi Energy

The Fermi energy of electrons in the AG lattices is one of the key parameters. We can estimate the electron density from the Fermi energy and the number of electrons per unit cell. The Fermi energy is also critical to understand the occupation of states near the Dirac cones. Another use of Fermi energy is to monitor the lateral modulation potential. In our sample design, a minor reduction in Fermi energy from that of the as-grown wafer usually indicates a weak lateral potential modulation.

Optical emission spectra from transitions between conduction and valence subbands are used to determine the Fermi energy for the unpatterned GaAs quantum well as discussed in Section 3.4. Figure 6.2(a) shows the optical emission spectra from the unpatterned QW and compares it with spectra from AG lattices with $a = 50$ nm of different etch depths. Fig. 6.2(b)(c) shows corresponding SEM images of the AG lattices. The energy difference between optical emissions occurring at the bandgap and at the Fermi level, $\Delta E$, are indicated in the figure. The Fermi energy of the as-grown QW can be calculated within the parabolic dispersion approximation used in Eq. 3.20:

$$E_F = \frac{m_h}{m_e + m_h} \Delta E \tag{6.1}$$

where $m_e$ and $m_h$ are effective masses for conduction and valence bands, respectively. The Fermi energy of the as-grown QW is $E_{F1} = 5.7 \pm 0.3$ meV, which is in agreement with Fermi energy of $6.3 \pm 0.15$ meV estimated from transport measurements (there might be slight difference of Fermi energy across the whole QW wafer, the transport and optical measurements were carried out at different positions of the wafer).

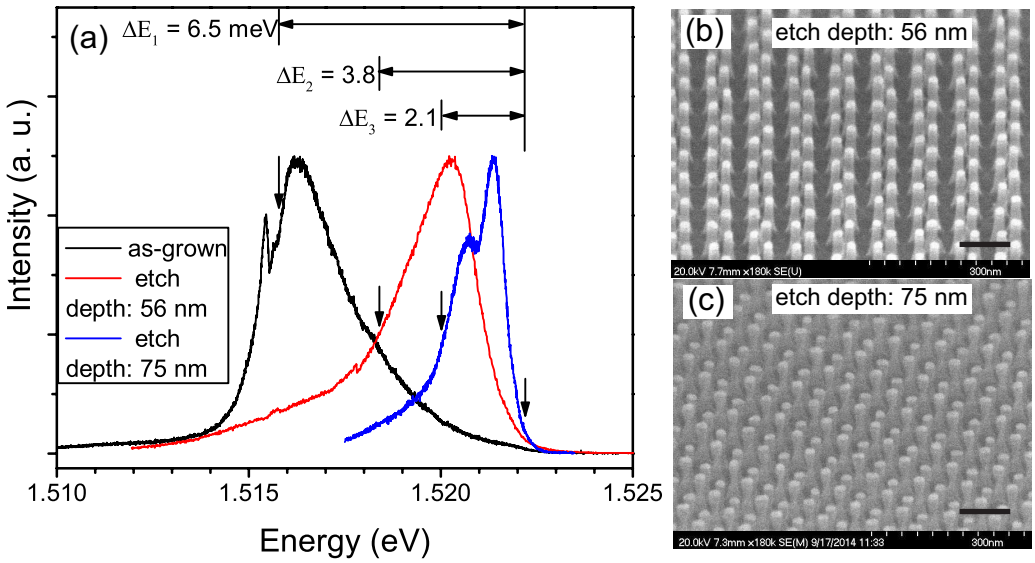


Figure 6.2: Determination of Fermi energy from optical emission. (a) Optical emission spectra from as-grown QW and AG lattices with different etch depths. The lattice constant of AG lattices is $a = 50$ nm. $\Delta E$(see Eq. 3.20) is labeled for each spectrum to determine the Fermi energy. SEM images are shown for AG lattices with etch depth of (b) 56 nm and (c) 75 nm. There is some undercut in the side profile of the deeper etch (75 nm) sample, but we can still observe evidences of AG electronic band structures which will be discussed in the following Subsections 6.2.2 and 6.2.3.

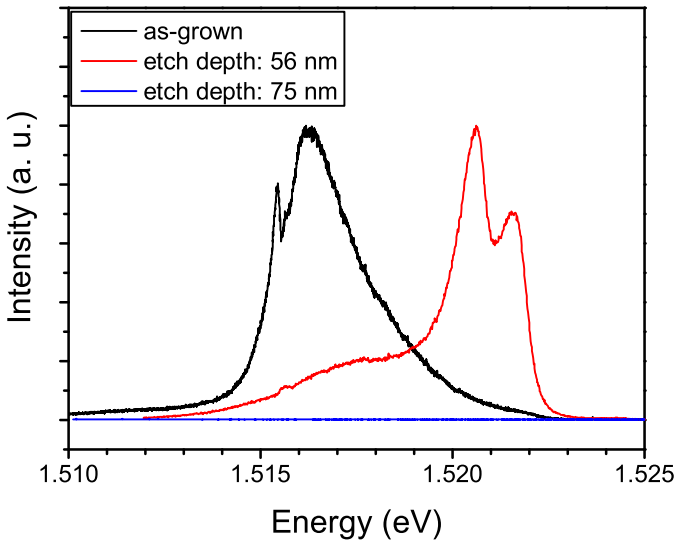


Figure 6.3: Optical emission spectra from the as-grown QW and the off-pattern area of AG samples in Fig. 6.2. From the red spectrum, the sample with etch depth of 56 nm, the off-pattern QW (not shown) is partially depleted, indicating a weak AG potential. The absent of any optical emission from the off-pattern of the AG sample with etch depth of 75 nm indicates a full depletion of electron density outside the AG patterns. The AG potential of this sample is estimated to be about 6 meV.

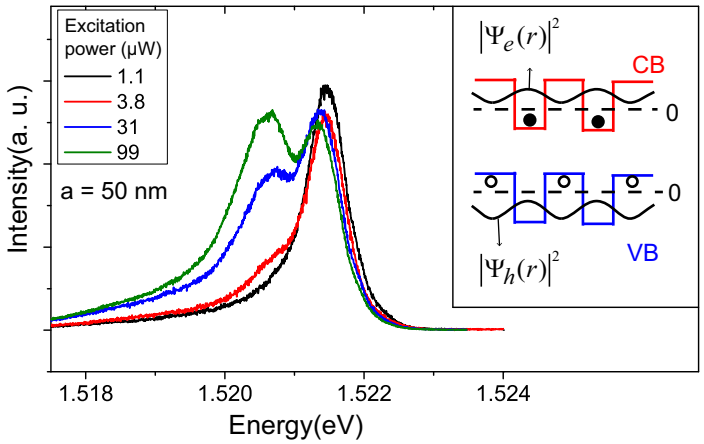


Figure 6.4: Power dependence of optical emission spectra from the AG lattice with $a = 50$ nm. The AG lattice is from the same sample with deep etch depth (75 nm) in Fig. 6.2 and Fig. 6.3. The insert sketches the conduction and valence bands of the AG lattices in real space. The spatial separation of electrons and holes are indicated.

The Fermi energy of AG lattices can not be simply derived from Eq. 6.1 as parabolic band dispersion assumption is not applicable for AG lattices. In AG lattices, electron minibands are formed as well as hole minibands. However the hole minibands are very flat due to the much larger effective hole mass[13], thus $\Delta E$ can still be used to estimate the Fermi energy. The determination of the onset of optical emissions from AG lattices takes into account that such emissions are indirect in real space[29, 30], as discussed in Fig. 5.7. The Fermi energies of AG lattices are estimated to be $0.9\Delta E$ by contributing 10% of $\Delta E$ to valence band curvatures. Thus the Fermi energies of the AG lattices with shallower etch depth (56 nm) and deeper etch depth (75 nm) are estimated to be: $E_{F2} = 3.4 \pm 0.4$ meV and $E_{F3} = 1.9 \pm 0.3$ meV. This is consistent with our intuition that the deeper etch, the more depletion of electrons in the AG lattices.

We can clearly see the reduction of the Fermi energy in AG lattices and the impact of etch depth on such Fermi energy reduction. Moreover we can use the reduction of the Fermi energy outside of AG patterns, as shown in Fig. 6.3, to estimate the depth of the AG potential. It shows the optical emission spectra from off-pattern area corresponds to the samples in Fig. 6.2. For the sample with etch depth of 56 nm, the electron density outside of AG lattices is partially reduced as shown in the red spectrum, and this partial reduction indicates a weak AG potential (less than 5 meV). The peak around 1.522 eV in the spectrum may be due to Fermi edge singularity[84]. On the other hand, the optical emission from the sample with etch depth of 75 nm is absent, which indicates a full depletion of electron density outside AG patterns. Thus the AG potential in this fully depleted case is estimated to be about 6 meV, the Fermi energy of the as-grown sample [13, 37].

Strikingly, the optical emission spectra from the AG lattices have strongly power dependent shapes, as shown in Fig. 6.4. The optical emission onset becomes more apparent with increasing power, which can be explained by the difference in con-

finement for conduction and valence states under the AG potential as shown in the inset to Fig. 6.4. While the electron wavefunction has higher amplitude under the AG pillars, the hole wavefunction has higher amplitude away from the pillars. Thus, electrons and holes tend to be spatially separated, and the overlap of their wave functions is very small at the bandgap, resulting in a diminished onset. Higher excitation power generates non-equilibrium holes in high-energy states with larger overlap with electrons, giving rise to stronger optical recombination. The strong power dependent shape of optical emission spectrum can be used as an indication of a strong AG potential.

### 6.2.2 Intersubband Excitations

Combined intersubband excitations observed in RILS spectra such as those considered in Subsection 5.3.4 offer a powerful tool for probing the electron states produced by the AG lattices. In Subsections 5.3.4 and 5.3.5 I evaluated the JDOS of intersubband excitations from AG band structures. In this subsection I will present RILS of intersubband excitations from AG lattices and the interpretation of these data via calculated JDOS for AG lattices.

Intersubband excitations deriving from changes in the confinement in the QW are illustrated in Fig. 6.5 for the as-grown sample. Collective modes have well-defined polarization selection rules[85]. The spin density excitations (SDE) are strong in the cross polarization configuration while the charge density excitations (CDE) are strong in the parallel polarization configuration. The single particle excitations (SPE), at energy 21.8 meV (denoted by $E_{01}^{0}$ in Fig. 6.5), are independent of the polarization configuration and it is a good measurement of the energy separation between the first two subbands as shown in the inset of Fig. 6.5. The intersubband excitations from the as-grown QW provide the helpful foundation to interpret spectra from the AG lattices.

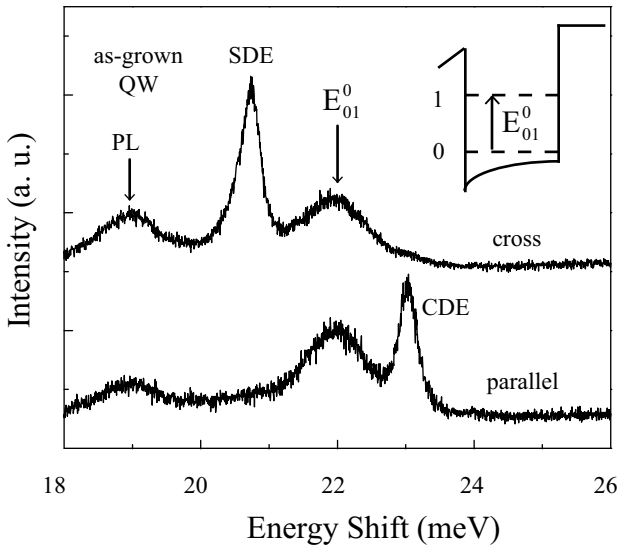


Figure 6.5: Intersubband transitions of the as-grown QW. SDE and CDE (explained in text) have polarization selection rules while SPE denoted by $E_{01}^0$ is present on both polarization configurations.

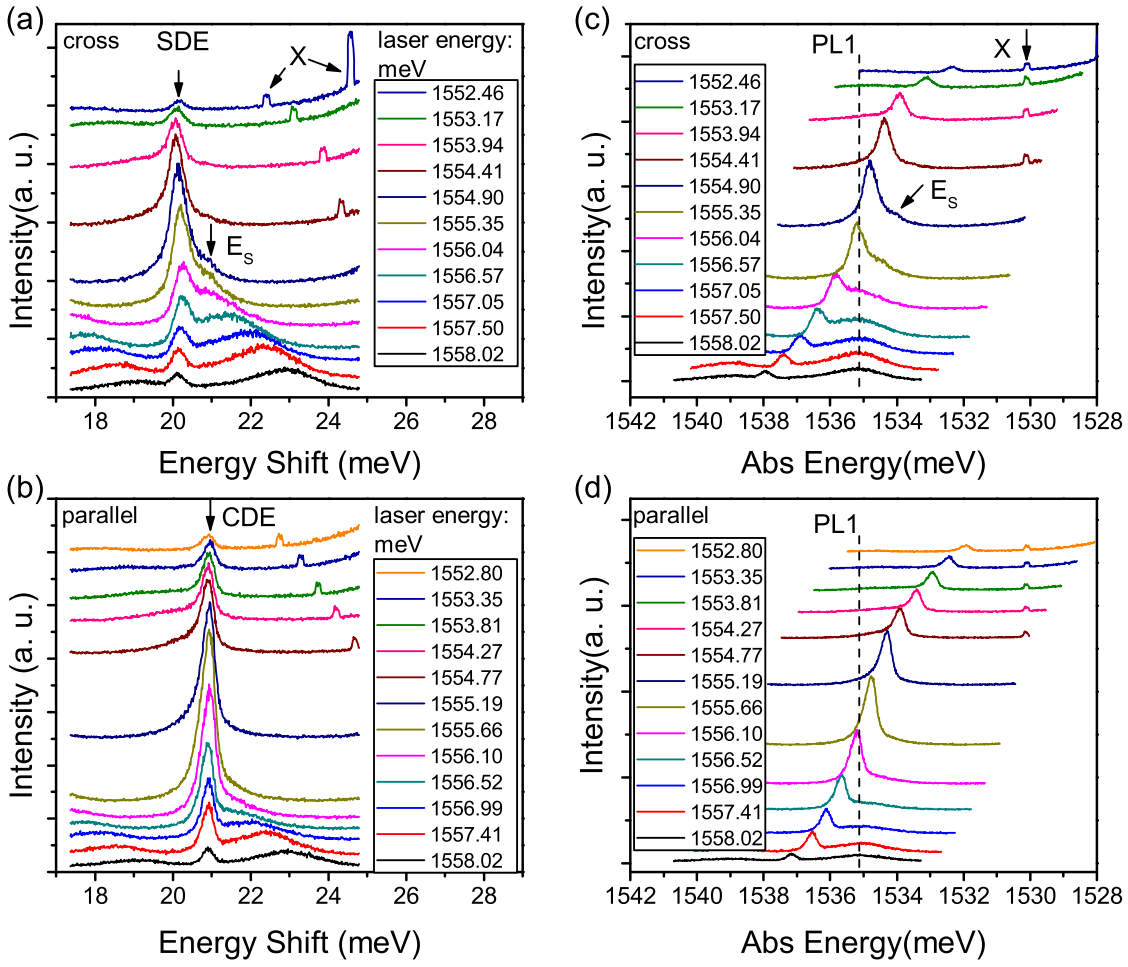


Figure 6.6: Intersubband transitions of an AG lattice with $a = 50$ nm under weak modulation (sample# M10-20-14.1 dev2). Spectra are plotted in Raman shift scale for (a) cross (b) parallel polarization configurations. They are vertically shifted for clarity. The corresponding spectra under absolute energy scale are in (c) and (d). SDE and CDE are labeled in (a) and (b), showing a resonant enhancement profile. Optical emission (PL) peaks are indicated by vertical line at energy denoted by PL1 in (c) and (d).

We first examine the case of weakly modified electron band structures by weak potentials in the AG lattices as shown in Fig. 6.6. It is weakly modulated because electrons are not fully depleted outside of the AG patterns. Intersubband excitations and optical emission spectra (not shown here) clearly indicate the presence of electrons outside the AG lattices. So the modulation potential should be less than 5 meV as discussed in Subsection 6.2.1.

Figure 6.6 shows intersubband excitations with different incident photon energies from an AG lattice with $a = 50$ nm under two polarization configurations. Figure 6.6(a) and (c) are both obtained under cross polarization configuration, but plotted in Raman shift scale and absolute energy scale respectively, while Fig. 6.6(b) and (d) are under parallel polarization configuration. In Raman shift scale, light scattering features, such as SDE and CDE in Fig. 6.6(a)(c), stay at constant energy when incident photon energies are changed. The resonant enhancements of SDE and CDE are clearly shown. On the other hand, in absolute energy scale, optical emission peaks, such as the one around 1535 meV labeled by PL1 in Fig. 6.6, stay when the incident photon energies are changed. X denotes features that are due to CCD artifacts and will not be discussed further.

This QW (sample# M10-20-14.1) is very similar to the one (sample# L06-27-14.1) used in most of this thesis except for a thinner top layer (50 nm instead of 70 nm) above the QW (see Appendix B for details). The optical emission spectra and intersubband excitations from this sample are also similar to those from sample# L06-27-14.1. The discussions and conclusions from one QW sample is also applicable to the other similar QW samples.

One obvious difference in the intersubband excitations between the weakly modulated AG lattices and the as-grown sample (not shown here) is the energy separation between SDE and CDE. The SDE-CDE energy separation in the as-grown sample is about 2.3 meV in Fig. 6.5, while it reduces to only 1 meV in the AG lattice as

shown in Fig. 6.6. This energy separation is closely related to many-body effects[85] and we can use it to estimate the electron density. In first order approximation, we have $E_{CDE}^2 - E_{SDE}^2 \propto n$, where $E_{CDE}$ denotes the energy of CDE, $E_{SDE}$ denotes the energy of SDE and $n$ is the electron density. Given the as-grown electron density of $1.8 \times 10^{11}$ cm$^{-2}$, we can estimate the electron density of the AG lattice to be $8 \times 10^{10}$ cm$^{-2}$. Thus there are approximately 5 electrons per unit cell, which are more than the optimal case of 2 electrons per unit cell. A deeper etch not only increases the potential magnitude, but also reduces electron density. This will be discussed later in the strongly modulated situation.

The impact of AG lattices can be seen through the lineshapes of intersubband transitions. In Fig. 6.6(a) we can see some light scattering signal on the high energy shoulder of SDE denoted by $E_S$, as these signals do not overlap with optical emission peaks shown in Fig. 6.6(c). The light scattering continuum $E_S$ has maximum that overlap with CDE, which is surprising. The frequent leakage of the CDE signal due to the break down of the selection rule can not explain the relatively large intensity of $E_S$. Similar light scattering signals, that appear under cross polarization configuration but overlap with the CDE, have been observed in other weakly modulated samples. In the interpretation of the peak $E_S$ we assume that electron minibands are formed and combined intersubband transitions involving a change of AG band index contribute to the additional peak. However this does not explain the overlap of such satellite signals with CDE and the absent of such peaks on the high energy side of CDE. One possible explanation is that the Hartree term of the Coulomb interaction just nearly cancels out the exchange correlation term, resulting a minor shift of CDE compared to SPE. As the electron density reduces due to nanopatterning, the Hartree term collapses faster than the exchange correlation[86, 87]. Thus $E_S$ might be SPE which has minor energy shift from CDE.

Intriguingly it is easier to interpret the intersubband transitions from strongly

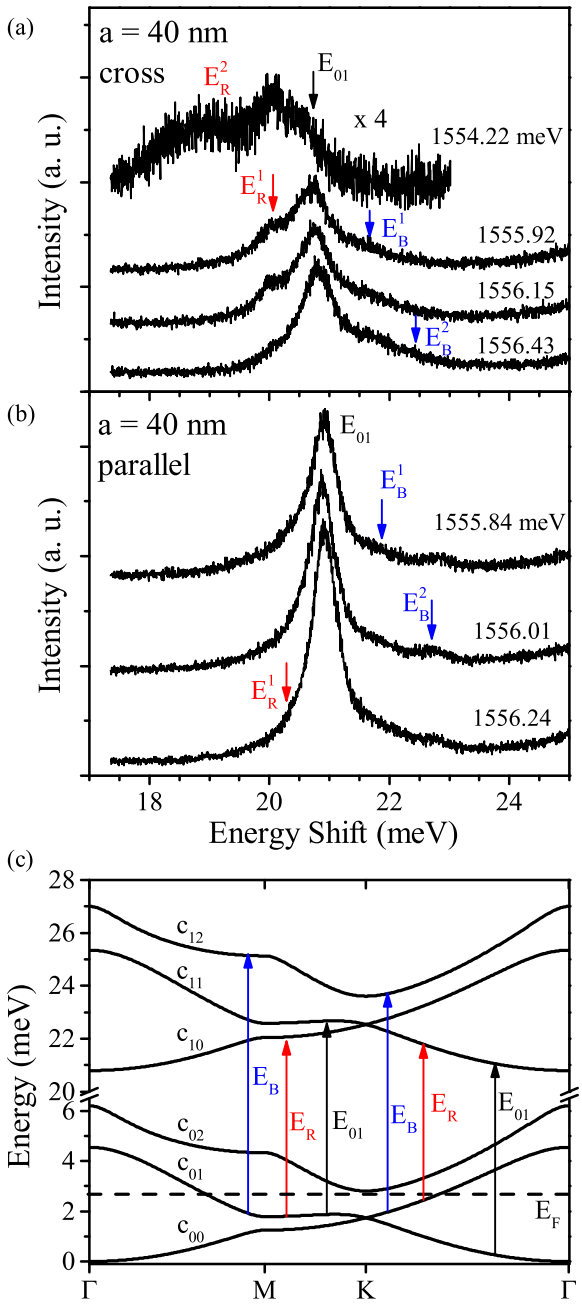


Figure 6.7: RILS spectra of intersubband transitions involving AG bands. (a) Cross and (b) parallel polarization configurations for RILS spectra from the $a = 40$ nm pattern, the incident photon energies are indicated. The peaks are interpreted as transitions between subbands indicated in (c), the band structure calculated with parameters $a = 40$ nm, $r = 8.0$ nm, $V_0 = -6.1$ meV, Fermi energy $E_F = 2.7$ meV. The vertical lines indicate transitions between subbands. The combined intersubband transitions with change of subband and AG band are indicated in blue and red.

modulated AG lattices. We present RILS spectra of intersubband excitations from two AG lattices, one with $a = 40$ nm and one with $a = 50$ nm, both showing interesting satellite peaks that also manifest the impact of the value of the lattice constant.

Figures 6.7(a)(b) shows RILS spectra of intersubband excitations of the AG pattern with $a = 40$ nm. The spectra display a strong peak at 20.9 meV denoted by $E_{01}$ accompanied by several weaker clearly defined satellite peaks. The strong peak $E_{01}$ is present in both polarizations. While many-body Coulomb interactions may have an impact on RILS spectra, $E_{01}$ is interpreted as the single particle transition between the first two subbands of the QW confinement. It is red-shifted from $E_{01}^0$ in Fig. 6.5 due to a decrease of the 2DEG electron density after etching. The satellite peaks, *only present in the etched AG sample*, are interpreted in terms of combined transitions between subbands of QW confinement and electron states created by the periodic potential of the AG lattice as schematically shown in Fig. 6.7(c). In these combined transitions, the change in the AG band index provides insight into physics associated with honeycomb topology.

In a simplified description, the RILS spectra in Figs. 6.7(a)(b) are interpreted as proportional to the JDOS for combined intersubband transitions with AG band index change, such as those shown in Fig. 6.7(c). More features of JDOS have been discussed in Subsection 2.2.2 for general band structures and in Subsections 5.3.4 and 5.3.5 for AG band structures. The JDOS calculation (Fig. 6.8) includes different possible transitions in the energy range close to $E_{01}$ and consists of both red-shifted and blue-shifted transitions. The JDOS is broadened by a Gaussian function with full width at half maximum (FWHM) of 0.2 meV [88]. The calculated JDOS is based on calculated band structures shown in Fig. 6.7(c) and does not take into account the energy dependence of RILS matrix element. The parameters used in calculation, $r$, $V_0$ and Fermi energy $E_F$, are first estimated from experiments and

then slightly adjusted for the best fit of JDOS as discussed in Subsection 5.3.4. As we mentioned in Chapter 5, the radius of potential used in modeling, $r$, is smaller than the physical radius of pillars, $r_0$, indicated in Fig. 6.1(a). Nevertheless this simplified model provides a rather good interpretation of the satellite peaks.

To identify the energies of the satellite peaks $E_R^1$, $E_B^1$ and $E_B^2$, we fit the spectra with multiple Lorentzian peaks. The results of the fit are shown in Fig. 6.8. The calculated JDOS has maxima at energies that overlap with those of the satellite peaks. The strong peak of JDOS at $E_{01}$ (black curve in the lowest panel of Fig. 6.8) arises from transitions between subbands with same AG band index (such as transitions from $c_{00}$ to $c_{10}$ and from $c_{01}$ to $c_{11}$ in Fig. 6.7(c)), which involves parallel bands with a high JDOS. The red-shifted satellites $E_R^1$ and $E_R^2$ are from transitions between $c_{01}$ and $c_{10}$. The blue-shifted satellites $E_B^1$ and $E_B^2$ are from transitions between $c_{01}$ and $c_{12}$. The lowest energy signal $E_R^2$ (shaded in red in the JDOS in Fig. 6.8) can be resonantly enhanced at lower incident photon energy, such as the top spectrum of Fig. 6.7a.

The results from the AG lattice with $a = 50$ nm are shown in Fig. 6.9. The red-shifted peak $E_R^{1,2}$ is resolved at lower incident photon energy while the blue-shifted peak $E_B^{1,2}$ is resolved at higher photon energy, due to the selective resonant enhancement at different incident photon energies. The smaller energy scale, due to the larger lattice constant, results in more narrowly spaced features in the JDOS and single broader RILS satellite peaks $E_R^{1,2}$ and $E_B^{1,2}$ (Fig. 6.9) rather than separate peaks seen for the $a = 40$ nm pattern (Fig. 6.8). The results clearly demonstrates the impact of the lattice constant on AG band structures.

### 6.2.3 Inter-AG-band Transitions

Inter-AG-band transitions, direct transitions between AG bands within the same subband of the QW, are discussed in this subsection. The transitions around Dirac

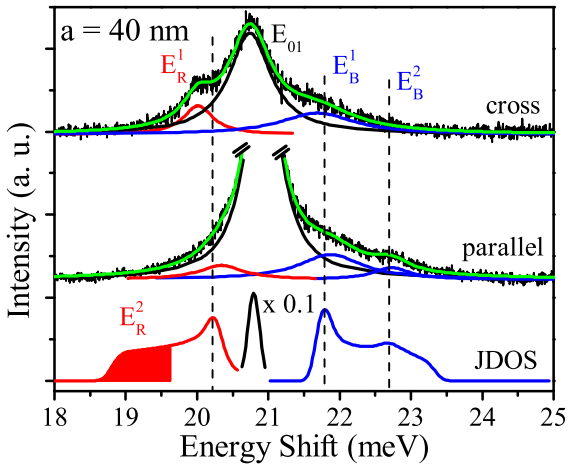


Figure 6.8: Interpretation of RILS spectra in Fig. 6.7 as combined intersubband transitions for the $a = 40$ nm patterns as explained in the text. The calculated JDOS (bottom curves) are for the transitions indicated in Fig. 6.7(c). The central peak, shown in black, is rescaled for clarity. Combined intersubband transitions are shown in blue and red. The peak positions in the RILS spectra (top curves) agree with the peaks observed in the JDOS. The parameters used for the calculation of JDOS are $a = 40$ nm, $r = 8.0$ nm, $V_0 = -6.1$ meV, $E_F = 2.7$ meV.

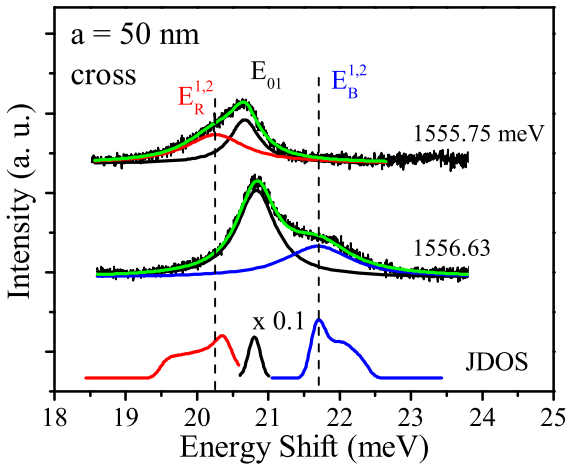


Figure 6.9: RILS spectra of intersubband transitions for the $a = 50$ nm pattern, the incident photon energies are indicated. The combined intersubband transitions are shown in blue and red. The calculated JDOS is shown in the bottom panel. The blue and red curves in the JDOS have maxima at energies overlap the positions of the measured intersubband transitions. The parameters used for calculation of JDOS are $a = 50$ nm, $r = 8.5$ nm, $V_0 = -6.4$ meV, $E_F = 1.7$ meV.

cones are probed in these spectra.

RILS spectra of low-energy excitations from the AG lattice with $a = 50$ nm are shown in Fig. 6.10(a). The light scattering signal overlaps with relatively weak PL, which is due to the optical emission between Fermi level and light hole states and provides an outgoing resonance mechanism. To extract the lineshapes of the low-lying excitations, the weak PL is subtracted as shown in Fig. 6.10(b). Typical spectra after removal of the PL are shown in Fig. 6.10(c), where a clearly identifiable narrow peak (FWHM $\approx$ 0.21 meV) near 0.85 meV is labeled as $E_L$ (similar to $E_B^1$ in Fig. 6.8). A weaker and broader peak located near 1.3 meV is labeled as $E_H$ (similar to $E_B^2$ in Fig. 6.8). These RILS spectra are interpreted as arising from transitions between states belonging to different AG energy bands, specifically from the band $c_{01}$ to the band $c_{02}$, indicated in Fig. 6.10(d). Low-lying excitations from the AG lattice with $a = 40$ nm is not available due to the deterioration of samples after exposure to air.

RILS spectra of the inter-AG-band transitions, shown in Fig. 6.10 (no change in QW subband state), are expected to be proportional to the JDOS for vertical transitions (no wave vector change) as discussed in Subsections 2.2.2 and 5.3.4. The calculated JDOS peak shown in Fig. 6.10(c), which very precisely overlaps the peak $E_L$, is largely due to transitions in the regions of the wave vector space marked as 1 and 2 in Fig. 6.10(c) and (d). This agreement indicates that disorder-induced broadening plays a minor role, a crucial condition for the appearance of MDFs. In region 1, the $c_{01}$ and $c_{02}$ bands are nearly parallel, which results in a maximum in the JDOS. Transitions in region 2 of the JDOS are from the Dirac cones formed at the K and K' points. Transitions in region 3 are mainly transitions around the M point in the Brillouin zone where the $c_{01}$ and $c_{02}$ bands have fairly different k-dispersion, generating the broader peak $E_H$. The excellent agreement between the RILS spectra and the calculated JDOS is strong evidence of the energy-dispersion of the AG bands formed under the periodic potential generated by the fabricated nano-patterns.

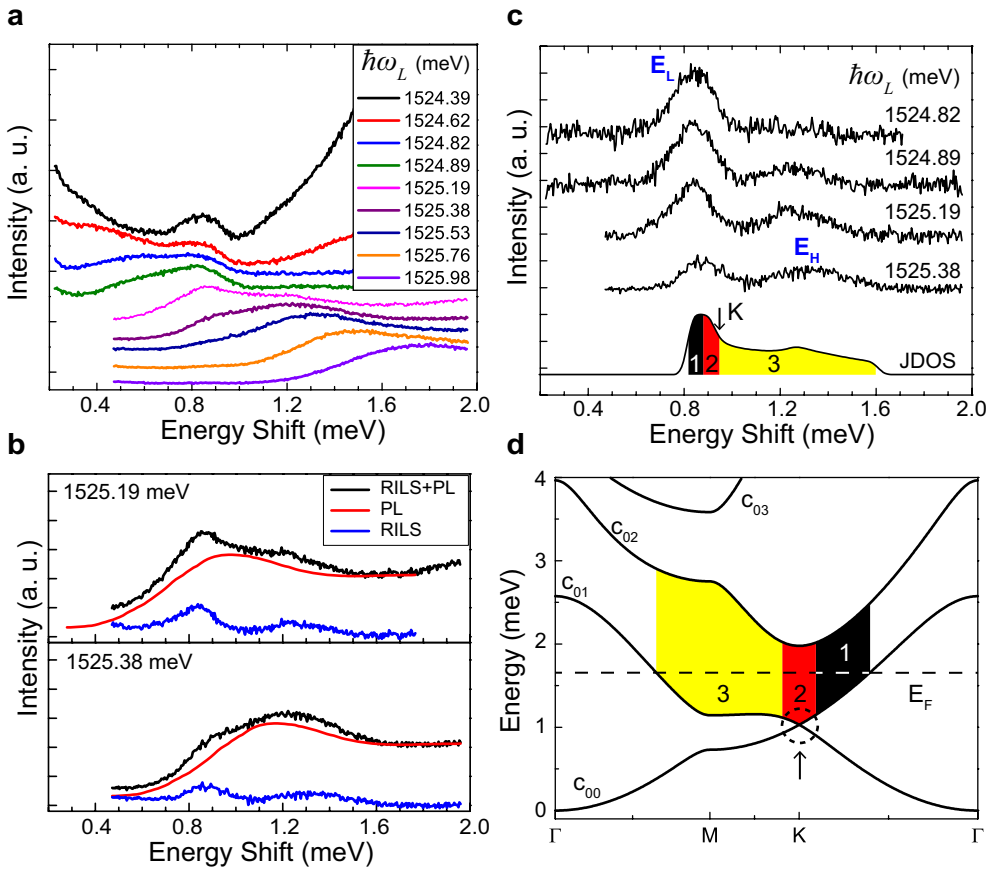


Figure 6.10: Spectra of inter-AG-band transitions from a 50 nm lattice constant AG lattice. (a) Spectra of low-lying excitations at different incident photon energies . The RILS signal overlaps with the PL background. (b) Subtraction of the background PL (red) reveals the RILS signal (blue). (c) RILS spectra for different incident photon energies after the removal of the PL background. Two peaks are identified at EL = 0.85 meV and EH = 1.3 meV. The calculated JDOS of the inter-AG-band transitions between the c01 and c02 bands is in agreement with the observed spectra. The different contributions to the JDOS are explained in (d). (d) Illustration of the electronic transitions associated with the observed RILS spectra. The AG bands are calculated with a = 50 nm, r = 8.5 nm, V0 = - 6.4 meV. The Fermi energy used in the calculation of the JDOS is 1.7 meV. The linear dispersion range in c00 and c01 bands is highlighted by a dashed circle. Three regions of the reciprocal space are identified with different colors in (d), and the transitions in each region are related to the corresponding energy range of the JDOS in (c).

In fact, the peaks $E_L$ and $E_H$ in Fig. 6.10 occur in combined intersubband transitions $E_B^{1,2}$ in Fig. 6.9. The red shifted satellite peaks in intersubband transitions $E_R^{1,2}$ are not allowed in this low-lying excitations because they are from higher AG band index to lower AG band index. The agreements of interpretations between intersubband transitions and inter-AG-band transitions provides convincing evidences of formation of AG miniband structures. Further more, the absence of the strong main peak $E_{01}$ allows us to clearly identify the lineshapes of signals related to the AG lattices thus to selectively resonant enhance transitions at different k spaces.

Transitions from region 2 are of particular interest since they originate from the segments of the reciprocal lattice Brillouin zone near the K and K' points, where MDFs are formed. In order to gain further insight into the contribution from transitions within this region to the $E_L$ peak, we take advantage of the resonance enhancement of RILS, shown in Fig. 6.11. At lower incident photon energies, the asymmetric $E_L$ peak is dominant, as seen in the upper spectrum in Fig. 6.11(a). Region 2 transitions occur at the high-energy cutoff of the $E_L$ peak (Fig. 6.11(a)). At this lower incident photon energy, the $E_L$ peak mainly results from the resonantly enhanced transitions around the Dirac points as shown in the inset to Fig. 6.11(b). The low-energy tail of the $E_L$ peak (grey area) likely arises from non-vertical transitions due to the impact of residual disorder as indicated in the inset to Fig. 6.11(a). The sharp cutoff of the $E_L$ peak at the high energy is interpreted as the cutoff of the JDOS due to Dirac cones at the K and K' points. These results provide evidence of well-defined MDFs.

## 6.3 Summary

In summary, we have realized artificial graphene in a modulation-doped AlGaAs/-GaAs QW patterned with 2D honeycomb lattices with very small period, excellent

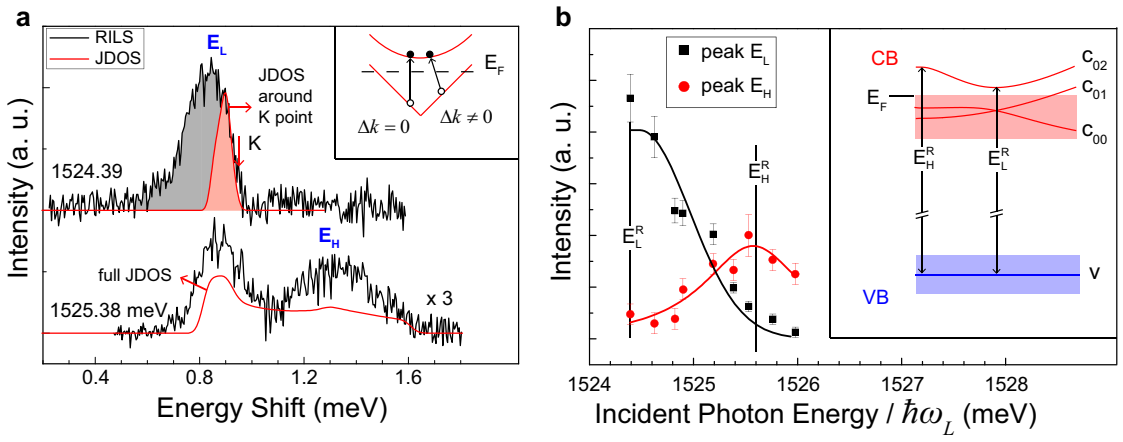


Figure 6.11: Dependence of the RILS on the incident photon energy. (a) RILS spectra at two different incident photon energies as labeled (in meV). The inset shows vertical ($\Delta k = 0$) and non-vertical ($\Delta k \neq 0$) transitions between the $c_{01}$ and $c_{02}$ AG bands. The upper spectrum taken at $\hbar\omega_L = E_L^R$(see inset to (b)) largely derives from transitions close to the K and K' points. It shows an asymmetric $E_L$ peak with a sharp cutoff on the high-energy side. The contribution to the JDOS from transitions near the K and K points (red curve) accurately describes the line shape of the high-energy cutoff due to the vanishing DOS at the Dirac point. The signal at lower energy (gray area) is explained by non-vertical transitions due to residual disorder (see the inset). The lower spectrum, taken at higher and showing peaks at $E_L$ and $E_H$, is interpreted with the JDOS (in red) with contributions from a larger range of k space (regions 1, 2 and 3 in Fig. 6.10(c,d)). (b) Integrated intensities of the $E_L$ and $E_H$ peaks as a function of showing maxima at $E_L^R$ and $E_H^R$. Inset: band diagram (not to scale) showing transitions from the valence band (v) to the conduction bands produced by the AG potential that explains the observed resonant enhancement maxima at $E_L^R$ and $E_H^R$ as a function of the incident photon energy.

long-range order, short-range uniformity and anisotropic etching profile. RILS spectra of intersubband transitions reveal combined transitions involving changes of both QW subbands and AG band index while low-lying excitations reveals direct transitions between AG bands. Such transitions have remarkable agreement with the calculated JDOS based on band structures of the AG lattices.

RILS spectra of inter-AG-band transitions around the Dirac cones have a unique lineshape that is linear around the high energy cut-off. This is a signature resulting from the linear energy-momentum dispersion of the Dirac cones and can be used as an optical method to identify MDFs. The RILS spectra presented in this chapter provide strong evidence of formation of AG electron bands and shine light on of MDFs realized in semiconductor systems.

The observation of MDFs on a macroscopic region of a nanofabricated semiconductor system opens new research opportunities. The ability to alter the lattice period and inter-site coupling by tuning the design of the artificial structure can enable the exploration of changes in Fermi velocity of MDFs and the possibility of opening of a bandgap by removing the inversion symmetry of the lattice. The realization of AG lattices in a nanofabricated high-mobility semiconductor system offers the advantage of great tunability through nanofabrication methods suitable for device scalability and integration. The ability to select the strength of the spin-orbit coupling by modifying the semiconductor system creates venues for seeking novel phenomena linked to opposite propagation of states with reversed spins and emergence of MDFs with intriguing topological character[89]. The implementation of such AG lattice in materials with strong spin-orbit coupling should enable the exploration of topological insulating states with great tunability[16]. The tunable parameters also make AG lattices a new realm for investigations of fractal quantum physics beyond the Hofstadters butterfly[15] studies in semiconductors and in natural graphene[73, 90–92].

Part of the results presented in this chapter have been submitted for

publication[83, 93].

# Chapter 7

# Graphene Growth by MBE

## 7.1 Introduction

Graphene attracts much current interest because of its intriguing 2D electron physics[1, 2] and the significant potential of graphene layers as a material system for novel applications[94]. While mechanical exfoliation method provides high quality graphene[9], the area size is limited to tenth of micrometer size. Creation of reliable epitaxial methods for growth of high quality large area graphene layers is of great importance. Early work was focused on selective evaporation of Silicon in SiC[95]. Growth of graphene by chemical vapor deposition (CVD) on Cu as a catalyst requires a transfer step from the Cu to a suitable substrate for further processing and characterization[96, 97].

Molecular beam epitaxy (MBE), a highly controllable growth method with atomic precision, is a promising alternative for fabrication of large area graphene layers directly on dielectric substrates. MBE methods emerged in the late 1960s[98] and became very successful for growing semiconductor quantum wells hosting high mobility charge carriers. In the ultra-high vacuum ($10^{-9}$ Torr) MBE chamber, atoms or molecules are deposited on the substrate directly. The deposition rate is very low,

thus the thickness of the grown structures can be controlled with the accuracy of one atomic layer. Usually the optimal growth condition is achieved by tuning the substrate temperature and the deposition rate.

Successful growth of graphene layers on diverse dielectric substrates by MBE has been reported recently[99–105]. In graphene MBE the weak van der Waals coupling between the first grown layer and the substrate is a crucial feature that enables graphene growth on a substrate with a different lattice constant. While hexagonal Boron Nitride (h-BN) is an ideal substrate for graphene growth by MBE[101], high quality h-BN substrates are only available as micron-size flakes.

To achieve large area growth of graphene layers by MBE, the choice of substrate is important. c-plane (0001) oriented sapphire is a highly suitable substrate because its atomically flat surface remains stable at relatively high temperatures[99, 102, 104]. This enables us to explore larger temperature range to optimize the growth conditions. Moreover c-plane sapphire substrates with large size ($>$ 1 cm) are available commercially.

This chapter reports the fabrication of nanocrystalline graphene layers on sapphire substrates by MBE. The growth of single- and bi-layer graphene is achieved with a solid carbon source in a unique molecular beam system that has design features to allow large gradients of incident carbon flux and of substrate temperature. The variations of the incident carbon flux and substrate temperature enable the identification of growth parameters that are suitable for fabrication of single layer graphene and multilayer graphene. A removal mechanism of carbon by reduction of sapphire, called "carbo-thermal reduction"[106], is discovered to have a large impact on the graphene growth. The interplay between carbon deposition and its removal drives the growth of graphene layers on sapphire substrate by MBE[107].

## 7.2 Results and Discussion

In our research we uncovered a striking competition between carbon deposition and its removal by reduction of sapphire in this work[107]. The effect is clearly seen in atomic force microscopy (AFM) images that reveal a significant density of etch pits in graphene layers grown at higher substrate temperature (around 1200 ℃). The etch pits are regarded as signatures of carbon removal from chemical reaction with oxygen in sapphire ($Al_2O_3$). Such reduction of sapphire will create etch pits in atomic layers of graphene by releasing CO in a process known as carbo-thermal reduction[106]. Etch pits similar to those reported here in graphene grown by MBE on sapphire have been reported in direct CVD growth of graphene on sapphire[108], a result that indicates that impact of carbo-thermal reduction that we discovered occurs in processing of graphene layers on oxygen containing substrates. The etch rate by carbo-thermal reduction of sapphire substrates has a step-like temperature dependence in the MBE growth chamber: for temperatures $T < T_o$ ($T_o \approx 1100$ ℃), the carbo-thermal reduction is negligible[107]. This is a remarkable finding which indicates that carbo-thermal reduction of sapphire substrates can be prevented. Suitable choices of the growth conditions - substrate temperature, incident carbon flux and growth chamber pressure - would allow growth without etch pits and achieve high quality graphene.

Single graphene layers occur in growth at higher substrate temperature (about 1200 ℃) and higher carbon flux (about 0.05 nm/min)[107]. The layers consist of aggregates of domains with a lateral dimension that is likely to be limited by the spacing between etch pits (about 100 nm). These graphene layers display superior crystallinity as revealed by phonon Raman bands that are consistently sharper than Raman bands reported in prior MBE growth of graphene on sapphire[107]. The Raman bands reported here have widths comparable to those seen in high quality single layer graphene that is directly grown by CVD on sapphire. The presence of intense D bands in Raman spectra of the grown single- and bi-layer graphene is

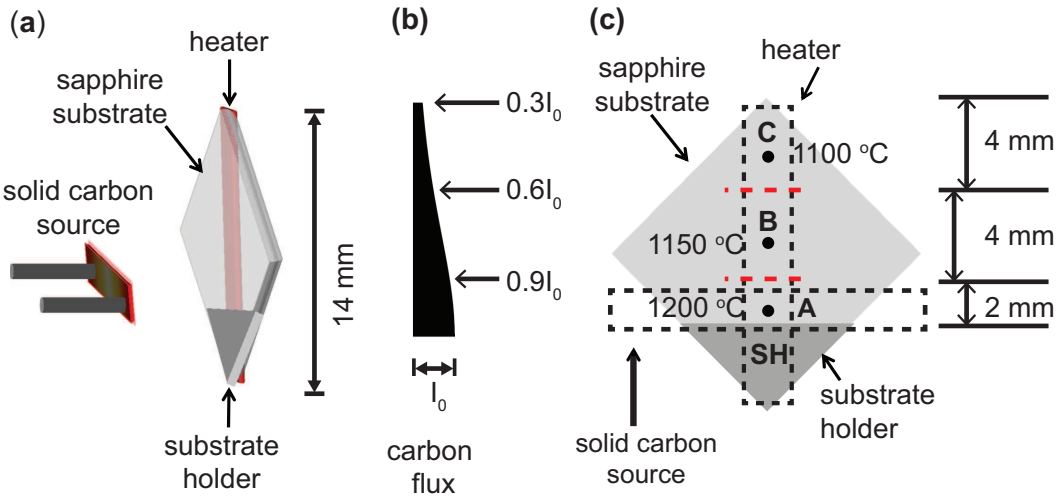


Figure 7.1: (a) Schematic description of the growth geometry showing the solid carbon source, the substrate, and the heater, (b) incident carbon flux as a function of vertical position on the substrate. Normalized flux values are indicated for three positions and (c) three regions A, B, and C having different growth are highlighted. The respective lengths (not to scale) and temperature are indicated. The markedly distinct growths in regions A, B, and C are described in the text.

attributed to contributions from the edges of the relatively dense random array of etch pits.

In our experiments graphene layers are grown in a homemade molecular beam system with a solid carbon source in an ultra-high vacuum (UHV) environment with a base pressure of $10^{-9}$ Torr[109]. Prior to growth the sapphire substrate was annealed for 1h at about 450 ℃ for degassing. The substrate temperature was then raised to the target temperature for growth which is kept within the range between 1100 ℃ to 1200 ℃. The maximum incident carbon flux is about 0.05 nm/min. During growth the chamber pressure increased to $10^{-7}$ Torr. The growth time is 4 h 47 min. After completion of growth the substrate was slowly cooled down (2 ℃/min) in the growth chamber.

Figure 7.1(a) sketches the MBE geometry. The distance between the solid carbon source and the sapphire substrate is 11 mm. This relatively short distance allows for a significant gradient of incident carbon flux on the substrate[101]. The estimated gradient of carbon flux is outlined in Fig. 7.1(b). The (0001) oriented sapphire (c-plane) substrates have area of 10 $\times$10 mm$^2$. A heater is positioned at the back of the substrate along its diagonal. Figure 7.1(c) describes the relative positions of the substrate, the heater, and the carbon source. The substrate temperature was measured with an optical pyrometer and the substrate holder temperature was monitored with a thermocouple.

In the growth configuration described in Fig. 7.1, radiation from the hot carbon source creates a temperature gradient along the substrate. The gradients in temperature and in carbon flux create three different regions marked as A, B, and C in Fig. 7.1(c). The substrate temperature is estimated to be 1200 ℃ in region A and 1100 ℃ in region C. The minimum flux in region C is estimated to be about 0.3 times of the maximum carbon flux incident on region A (see Fig. 7.1(b)). The three regions have strikingly different growths. Region A is covered by single-layer-graphene

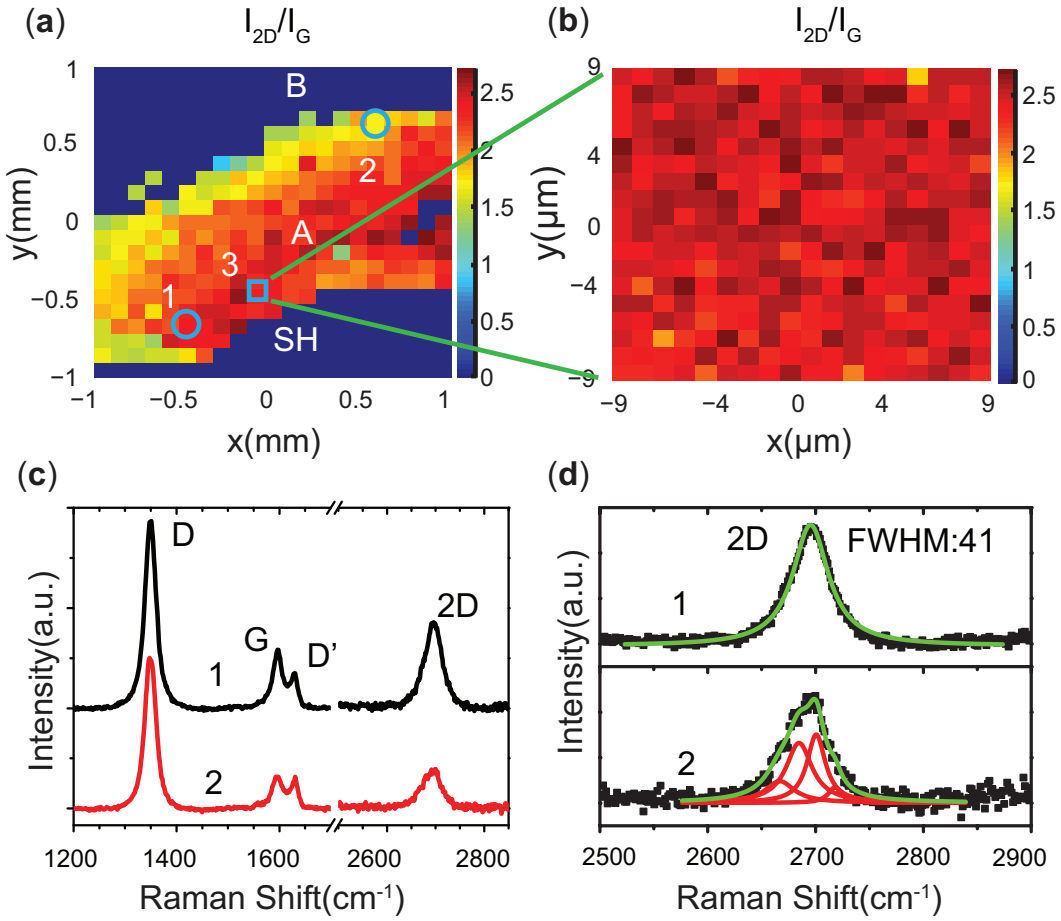


Figure 7.2: (a) Raman map of integrated intensity ratios of $I_{2D} = I_G$ in regions A, B and SH of Fig. 7.1(c). The absence of Raman signal in regions B (see Fig. 7.4(a)) and SH indicates that there is no graphene growth in these regions. The x-axis is approximately along the direction of the carbon source and the y-axis is along the heater direction (see Fig. 7.1(c)), (b) higher spatial resolution Raman map from position 3 in panel (a), (c) Raman spectra obtained from positions 1 and 2 in panel (a) and (d) Lorentzian fits of Raman 2D bands from positions 1 and 2 in panel (a). The spectrum from position 1 is fitted by a single Lorentzian while the best fit of the spectrum from position 2 requires four Lorentzians. These fits reveal SLG in position 1 and BLG in position 2 as described in the text.

(SLG) with some areas of bi-layer-graphene (BLG). We find no evidence of graphene growth in region B while there is growth of graphene multilayers in region C. The absence of graphene in region B and the reappearance of graphene growth in region C is an unexpected finding that is attributed to a marked temperature dependence of carbo-thermal reduction of sapphire. This temperature dependence suggests that the impact of carbo-thermal reduction of sapphire could be tuned to achieve the growth of large area graphene layers on sapphire substrates.

The topography of the grown graphene layers is recorded in tapping mode AFM measurements under ambient conditions. Raman spectroscopy, a powerful tool to study the properties of graphene layers, was employed to monitor crystallinity and the numbers of layers[110–114]. The room temperature Raman measurements were performed in a Renishaw in-via Micro-Raman instrument. The spectra were excited by the 532 nm (2.41 eV) laser emission. The laser spot has a diameter of less than 1 $\mu$m at a low laser power of less than 3 mW. Backgrounds that occur in Raman spectra were removed prior to fitting the phonon bands with Lorentzian line shape functions.

Figure 7.2 shows Raman data of graphene layers in region A. The four bands labeled D, G, D' and 2D shown in Fig. 7.2(c) are characteristic Raman features of graphene. The G peak is a zone center optical phonon and the 2D peak is a second-order two-optical-phonon band. The intensity and width of the 2D band is a measure of crystallinity[110–112]. The D and D' peaks are due to large wave vector optical phonons that are activated by lattice imperfections that break the translation symmetry of the honeycomb lattice[110, 111]. Figure 7.2(a) is a Raman map of the ratio $I_{2D}/I_G$ of the integrated intensities of the 2D and G Raman bands (the ratio is set to zero where there is no graphene growth). The map covers a $2\times2$ mm$^2$ area of the sample in which each pixel has a relatively large area $0.1\times0.1$ mm$^2$. The significant features in this Raman map are two areas of no graphene growth. In the

area labeled SH the substrate holder blocks the carbon flux. The remarkable absence of graphene growth in region B reveals the impact of parameters such as substrate temperature and incident carbon flux on growth. Figure 7.2(b) shows a small area ($19\times19$ $\mu m^2$) micro Raman map with small pixel of 1 $\mu m^2$ centered at position 3 in the map shown in Fig. 7.2(a). The map reveals nearly position independent Raman spectra that suggest there is uniform growth of graphene on a 10 $\mu$m scale.

Figure 7.2(c) shows typical Raman spectra from two positions in region A that are labeled 1 and 2. Strong D and D' peaks are due to large wave vector optical phonons that are activated by imperfections indicate significant presence of defects. The likely origin of the imperfections will be briefly discussed below. Figure 7.2(d) shows an analysis of the spectral lineshape of the 2D Raman bands in Fig. 7.2(c) as a superposition of Lorentzian functions. The fitting parameters for Raman spectra from position 1 are shown in Table 7.1. The full width at half maximum (FWHM) of Raman bands in region A (position 1 in Fig. 7.2(c)) are compared with recent results for MBE graphene grown on sapphire[99, 102, 104].

The spectral decompositions of the 2D Raman band in Fig. 7.2(d) in conjunction with the measured integrated intensities ratio $I_{2D}/I_G$ yield determinations of the number of graphene layers[112]. In Fig. 7.2(d) the Raman spectrum from position 1 is adequately fitted by a single Lorentzian. In contrast, the best fit of the spectrum from position 2 is obtained with four Lorentzians. In Figs. 7.2(c) and (d) the symmetric shape of the 2D band from position 1 as well as large $I_{2D}/I_G$ ratio (2.7) are strong evidence of single layer graphene[112]. The lineshape of the 2D Raman band and the smaller $I_{2D}/I_G$ ratio (2.0) suggests that bilayer graphene growth occurs at position 2[112, 113].

Figure 3(a) is an AFM image obtained in region A near position 2 in Fig. 7.2(a). The image reveals a rather high density of etch pits (about 80 $\mu m^{-2}$). The average distance between etch pits is around 100 nm, which can characterize the size of

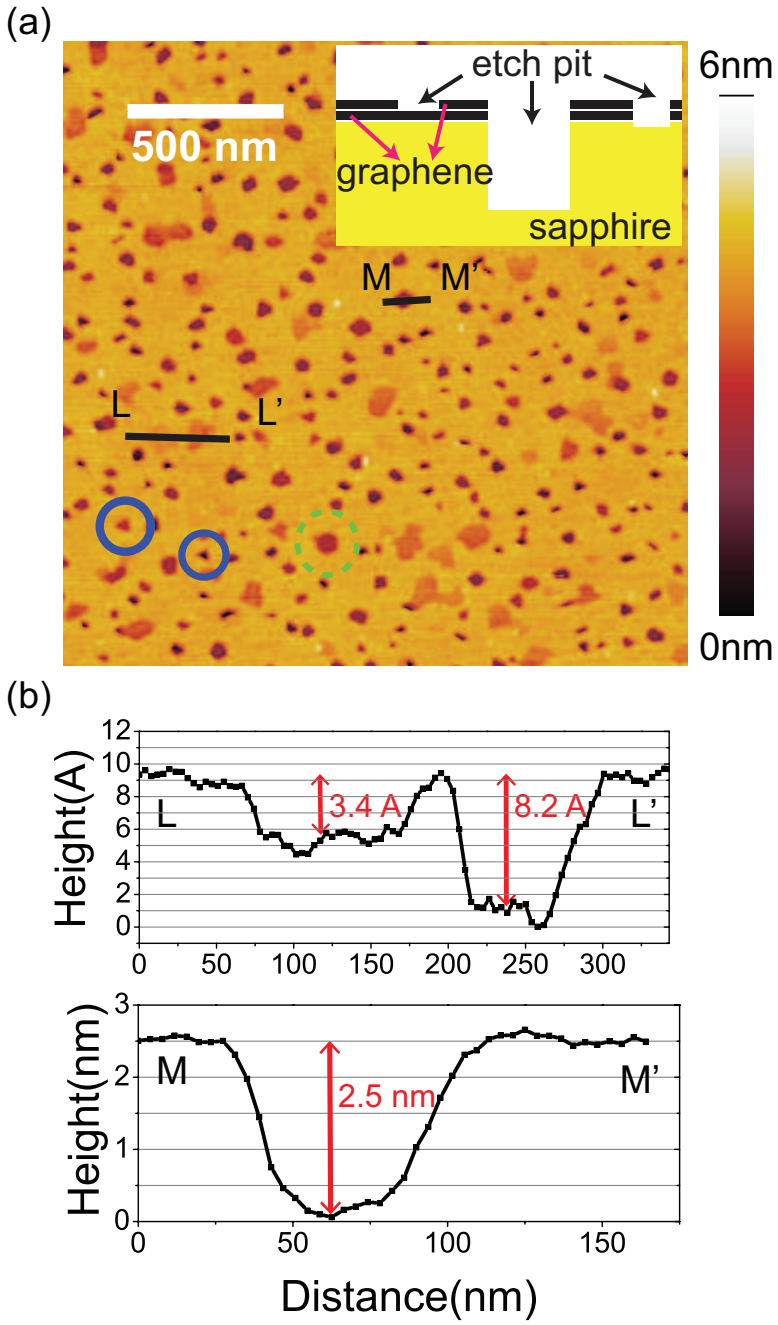


Figure 7.3: (a) AFM image ($2 \times 2\ \mu m^2$) in region A near position 2 in the Raman map in Fig. 7.2(a). The image shows numerous etch pits. Hexagonal (dashed green circles) and triangular (solid blue circles) etch pits are highlighted. Inset: a cartoon showing morphologies of etch pits and (b) height profiles along two lines across selected etch pits.

nanocrystalline graphene. The loss of translation invariance near etch pits may be a reason for the observation of intense D and D' Raman bands in spectra from region A. As already mentioned, the etch pits are attributed to major influence of carbo-thermal reduction of sapphire in the presence of a carbon flux. Some of the etch pits have well defined shapes. Selected etch pits are identified by dashed green circles (hexagons) and solid blue circles (triangles) in Fig. 7.3(a). The hexagonal and triangular shapes are consistent with reported shapes of etch pits on c-plane sapphire[115].

The shallower etch pits can have depths in the range between 0.3-0.4 nm, that is comparable to the thickness of single layer graphene. The deeper pits can have depth as large as 2-3 nm that go deep into sapphire. Figure 3(b) displays height profiles for shallow and deep etch pits. The profile along the line LL' displays two etch pits with depth of 0.34 nm and 0.82 nm which could occur in bilayer graphene. The height profile along the line MM' reveals an etch pit with depth of 2.5 nm. Given that the growth in region A consists largely of single layer and bilayer graphene, the etch pit found along the MM' line must go deep into the sapphire substrate. Despite of high density of etch pits, Fig. 7.3(a) shows a flat graphene surface in the areas without etch pits, which is consistent with the good crystallinity that is associated with sharp Raman bands. The inset of Fig. 7.3(a) shows schematic descriptions of shallow and deep etch pits that are consistent with the AFM imaging results.

Figure 7.4 displays results from region B. The unexpected absence of graphene related peaks in the Raman spectrum shown in Fig. 7.4(a) indicates that there is no growth of graphene for the values of incident carbon flux and substrate temperature in region B. Figure 7.4(b) is an AFM image captured in region B. The image in Fig. 7.4(b) and the height profile along the PP' line in Fig. 7.4(c) show that in region B the shallow and deep etch pits present in region A have been replaced by a set of nearly periodic parallel stripes that are highlighted by dashed lines in Fig. 7.4(b). The periodicity is around 50 nm. The surface morphology features seen in Figs. 7.4(b)

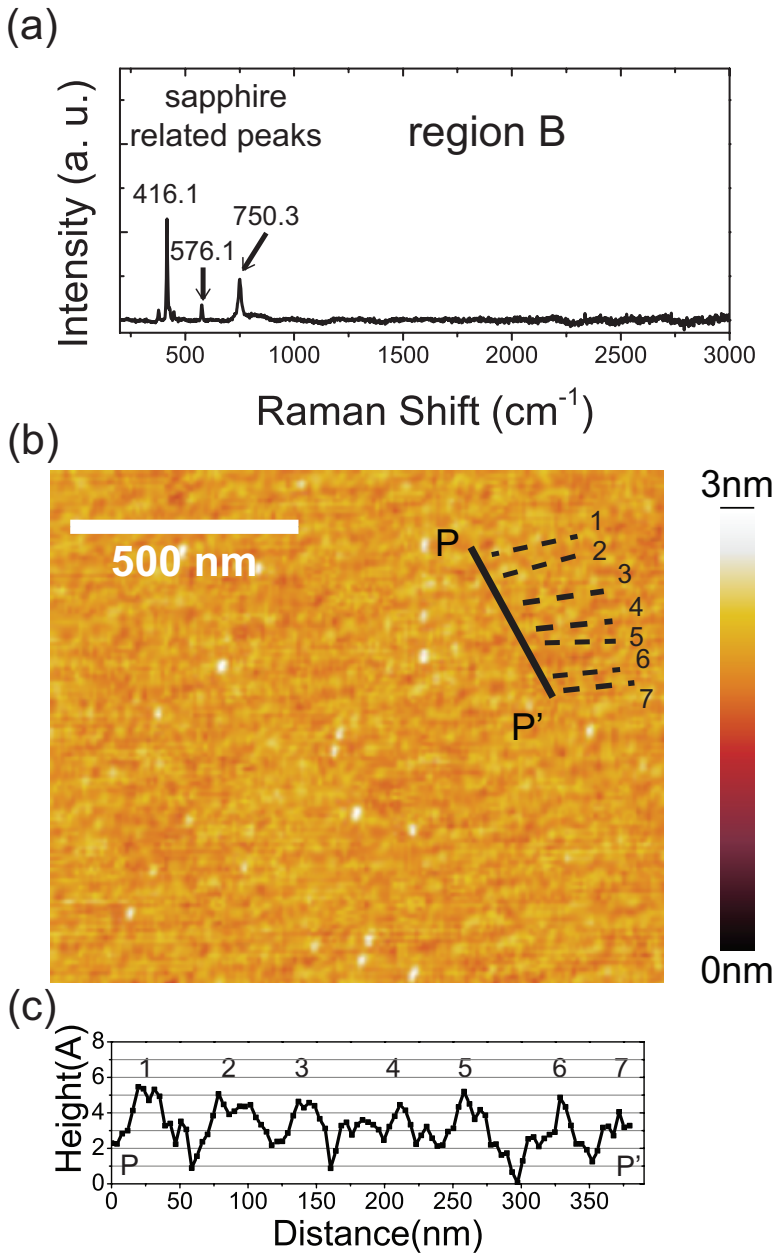


Figure 7.4: (a) A Raman spectrum from region B revealing that there are no graphene related Raman bands, (b) AFM image from an area ($1.3 \times 1.1\ \mu m^2$) in region B. The image shows nearly parallel stripes and absence of etch pits and (c) the height profile along line PP' in (a) indicates ridges with a periodicity of around 50 nm.

and (c) are similar to those reported in sapphire annealed at temperature of about 1100 ℃, as sapphire tends to form surface steps when annealed at temperature over 1000℃[116].

Figure 7.5 shows a typical Raman spectrum from region C. In contrast to findings in region B, here there is growth of graphene layers. The spectra, however, reveal growths that are quite different from the single layer and bilayer graphene found in region A. All the Raman bands are broader in region C. FWHM of 2D band increased from 41 $cm^{-1}$ (position 1 in Fig. 7.2(c)) in region A to 67 $cm^{-1}$ (Fig. 7.5) in region C. The smaller $I_{2D}/I_G$ Raman intensities ratio of about 0.5 in region C is an indication of multilayer graphene growth that is similar to those reported in prior growth of graphene layers MBE on sapphire substrates[99, 102, 104]. The inset to Fig. 4 is a 1 ×1 $mm^2$ Raman map of $I_{2D}/I_G$ ratio in region C, in which spectra were obtained at every 0.1 mm. In this Raman map the small variation of the $I_{2D}/I_G$ ratio, from about 0.5 to about 0.6, indicates quite a uniform growth in region C.

As indicated in Figs. 7.1(b) and 1(c), regions A, B, and C have different substrate temperatures and incident carbon flux. The unexpected results in Fig. 7.5 show that while region C has the smallest incident carbon flux, in the range of $0.3I_0$ - $0.6I_0$, multi-layer graphene is formed in this region. In contrast, while region B has a larger incident carbon flux ($0.6I_0$ - $0.9I_0$), it shows no graphene growth at all. It is even more surprising to find the reappearance of graphene growth in region A with marginally larger incident carbon flux. These surprising results are interpreted in terms of the competition between the rate of carbon deposition, the amount of carbon sticking to substrate surface per unit time per unit area, and of carbon removal due to carbothermal reduction of sapphire.

The proposed interplay between carbon deposition and carbon removal rates is schematically shown in Fig. 7.6. The horizontal axis denotes the distance from the substrate holder, as shown in Fig. 7.1, in the diagonal of the sapphire substrate. The

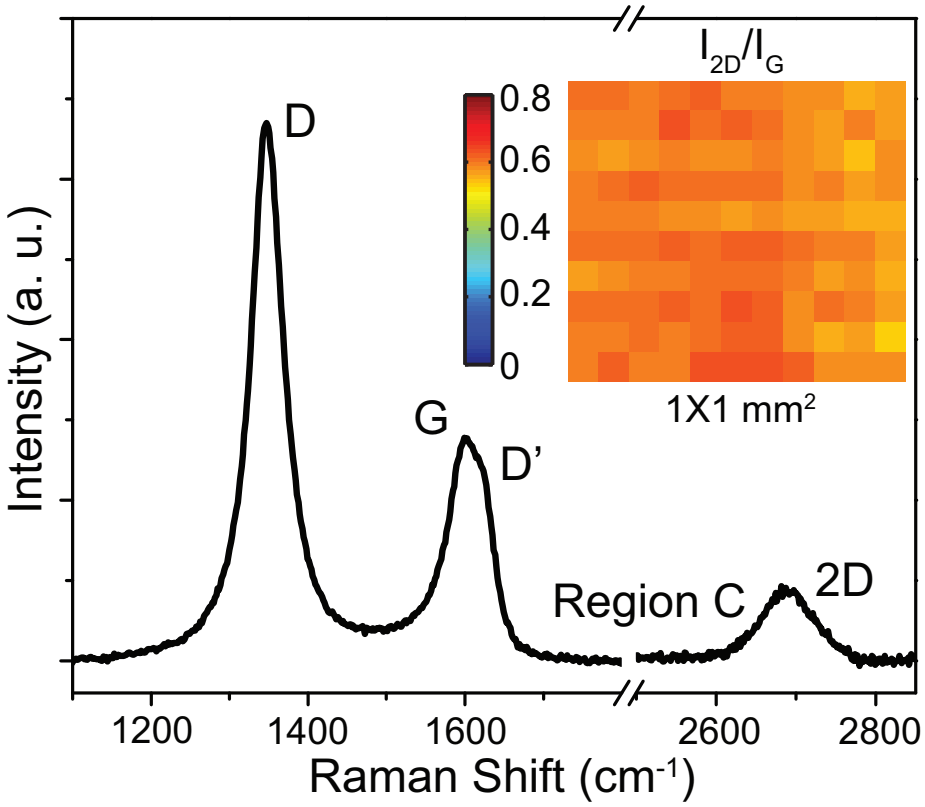


Figure 7.5: A Raman spectrum from the center of region C. The inset shows a Raman map of integrated intensity ratios of $I_{2D}/I_G$ indicating a variation of about 25% in the uniformity of the layers.

Table 7.1: FWHM Γ of Raman bands reported for MBE growth of graphene on sapphire.

| | $\Gamma_D$ $cm^{-1}$ | $\Gamma_G$ $cm^{-1}$ | $\Gamma_{D'}$ $cm^{-1}$ | $\Gamma_{2D}$ $cm^{-1}$ |
|---|---|---|---|---|
| this work[a] | 24 | 21 | 13 | 41 |
| Oliveira *et.al.*[b] | 33.7 | 29.2 | 16.9 | 54.2 |
| Liu *et.al.*[c] | - | 38 | - | 60 |
| Jerng *et.al.*[d] | 61.1 | 65.1 | 33.8 | 85.2 |

[a] Fitting parameters are from spectrum 1 in Fig. 7.2(c); [b] Ref. 12; [c] Ref. 10; [d] Ref. 8;

carbon deposition rate is the result reported in Ref[101]. Both carbon deposition and carbon removal rate decrease from region A to region C. This is due to the two gradients of incident carbon flux and substrate temperature. However the rate of carbon removal needs to be larger than the carbon deposition rate in region B while the opposite occurs in region A and region C due to the fact that graphene is only formed in region A and region C. In addition no etch pits are formed in region C, revealing a much reduced carbon removal rate in region C as indicated by the red line in Fig. 7.6 .

In this interpretation the appearance of three distinct growth regions A, B and C requires that the rate of carbo-thermal reduction of sapphire should have a very rapid temperature dependence in the relatively narrow temperature interval between 1100℃ and 1200 ℃ indicated in Fig. 7.1(c). This is a very sharp, step-like, temperature dependence which is shown in Fig. 7.6: carbo-thermal reduction is negligible in region C (around 1100 ℃), then it increases rapidly in region B at temperature close to 1150 ℃ to become nearly constant at higher temperature. Such a remarkable step-like temperature dependence for carbo-thermal reduction of sapphire at around 1100 ℃ is consistent with the reported step-like temperature dependence of carbo-thermal reduction of alumina[117, 118].

The step-like temperature dependence of carbo-thermal reduction of sapphire has

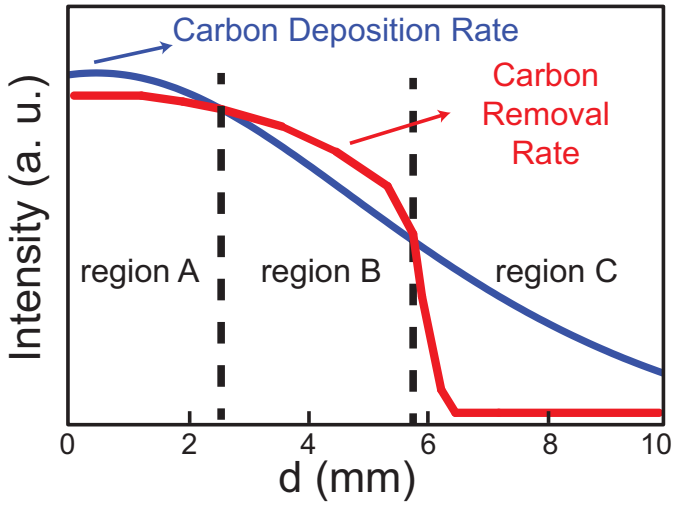


Figure 7.6: Interplay of carbon deposition and carbon removal rate that results in three distinct regions for growth of graphene on sapphire by MBE. The horizontal axis $d$ denotes the distance from the substrate holder, as shown in Fig. 7.1, in the diagonal of the sapphire substrate. The blue line is the carbon deposition rate determined from experiment. The red line is the proposed removal of carbon by carbo-thermal reduction of sapphire. No graphene is formed in region B because the carbon deposition rate is below the carbon removal rate.

a significant role on MBE growth of graphene on sapphire substrates. It is reasonable to conjecture that carbo-thermal reduction could be controlled by suitable tuning of substrate temperature, growth chamber pressure and of carbon flux. Similar considerations would apply for graphene growth on other large area substrates containing oxygen such as $SiO_2$.

## 7.3 Summary

In conclusion, single- and bi-layer graphene have been grown by MBE on a c-plane sapphire substrate. Sharp optical phonon Raman bands from single- and bi-layer graphene reveal the good crystallinity of grains of nanoscale dimensions. The dependence of growth on substrate temperature and incident carbon flux suggests a model for MBE graphene growth on sapphire in which there is competition between carbon deposition and carbon removal by reduction of sapphire that has a sharp step-like temperature dependence. Control and suppression of carbo-thermal reduction model could enable the growth of high quality graphene on a diverse class of substrates containing oxygen.

Part of the results presented in this chapter are published in Ref.[107].

# Chapter 8

# Future Research

This dissertation presents advances of studies of AG lattices on nano-patterned GaAs QWs. The milestone I achieved here opens up new realms of study that are to be explored further. In this chapter I propose some future lines of research that are inspired by my research.

## 8.1 Optimization of the AG Potential

The major challenges in our AG lattices design are from nano-fabrication. AG lattices with a lattice constant smaller than 40 nm are not successfully obtained at this stage. Further optimizations in nano-fabrication could reach smaller lattice constants (such as $a = 35$ nm). However tuning other parameters of the AG potential may be easier.

To achieve well-developed Dirac cones, the impacts of other parameters, potential height $V_0$ and ratio $r/a$, are explored as shown in Fig. 5.6. The Fermi energy (about 6 meV) sets the range for the potential height [13, 36], so the room left for further tuning is the ratio $r/a$.

For AG lattices with $a = 40$ nm and $V_0 = -6$ meV, the threshold of the ratio $r/a$ to obtain isolated Dirac cones is 0.19. Obtaining a ratio of 0.3, corresponds to a radius of 12 nm, will greatly improve the linear dispersion range of the Dirac cones as

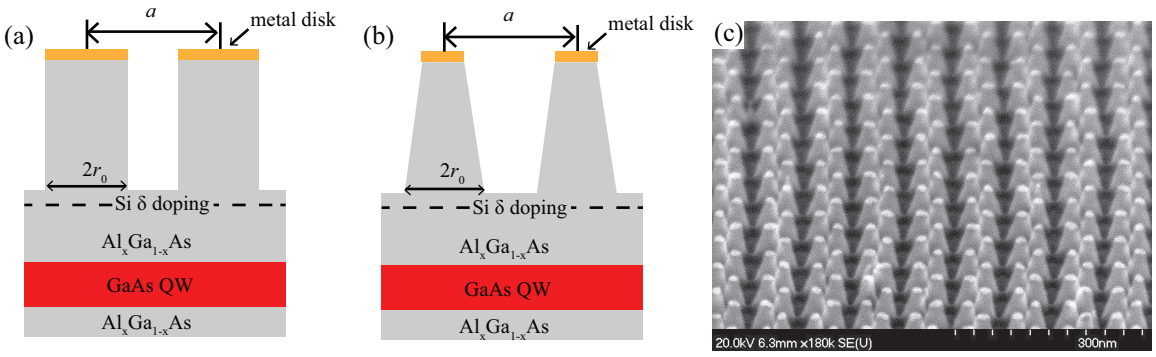


Figure 8.1: Two methods to achieve large potential radius: (a) large metal disks as etch mask and etch recipe with vertical side wall profile, (b) small metal disks as etch mask and etch recipe resulting cone shape profile, (c) a SEM image of AG pillars with $a = 50$ nm showing the proposed side profile of (b).

shown in Fig. 5.6. As I discussed in Chapter 5, due to the surface states on the side wall of the AG pillars, the potential radius is smaller than the geometrical radius of the AG pillars. This requires that the geometrical radius of the AG pillars, especially on the bottom portion, to be larger than 12 nm, say 15 nm. Two ways of achieving large ratio are suggested in Fig. 8.1. The first one is to create large metal disks which act as the etch mask. This is a straight forward method, but the lift-off is easy to fail with large radius. The second one is to change the ICP-RIE recipe to have cone-shape AG pillars as shown in Fig. 8.1(b). A preliminary work is displayed in Fig. 8.1(c), which shows a SEM image of AG pillars with $a = 50$ nm. The diameter of the bottom portion of the AG pillars is significantly larger than the etch mask on the top, and this will be very helpful to create AG band structures with large linear dispersion range around the Dirac cones.

## 8.2 Antidots with Triangular Lattice

Working with small lattice constant such as $a = 40$ nm is at the limit of equipments. Any improvement, if possible, needs significant efforts on optimizations of each fabrication step. A way to work around this is to design antidots arranged in triangular lattice. Instead of making nano disks of etch mask, antidots are making nano holes in the etch mask. Since honeycomb lattice dots and triangular lattice antidots have the same underlying Bravais lattice, linear dispersion also appears in the triangular lattice antidots. The advantage of using antidots is that the distance between nearest neighboring holes is $a' = \sqrt{3}a$ for the same Bravais lattice where $a$ is the distance between nearest dots in the honeycomb lattice as shown in Fig. 8.2(a)(c). The red regions in these two figures represent the etch mask and everywhere else are etched to appropriate depths to create potential modulations.

For honeycomb lattice with $a = 40$ nm, the distance between holes in correspond-

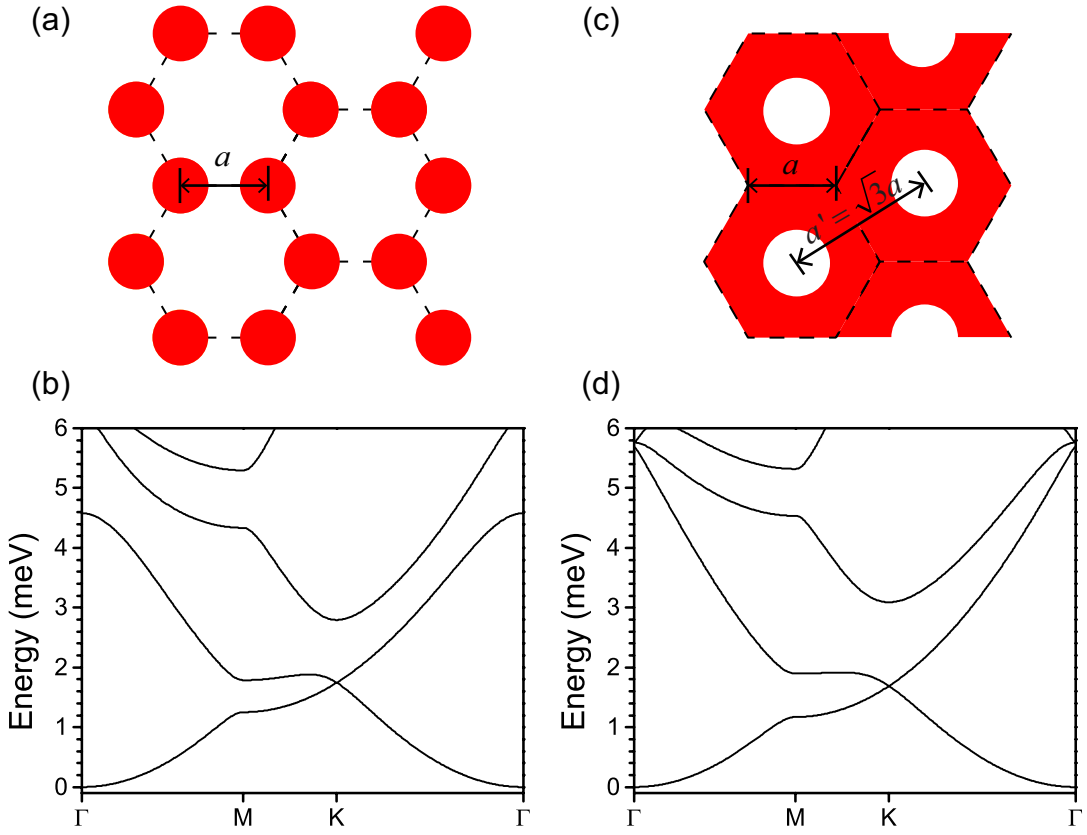


Figure 8.2: Comparison of honeycomb lattice dots and triangular lattice antidots. (a)(c) shows the etch mask (red regions) of honeycomb lattice dots and triangular lattice antidots. For the same underlying Bravais lattice, the inter-dot distance for honeycomb lattice is $a$ while the inter-hole distance is $a' = \sqrt{3}a$ for the triangular lattice. (b)(d) are corresponding band structures for the honeycomb lattice dots and triangular lattice antidots with parameters: (b)$a = 40$ nm, $V_0 = -6$ meV, ratio $= 0.20$ (b)$a' = 69$ nm, $V_0 = -6$ meV, ratio $= 0.20$.

ing antidots is $a' = 69$ nm, which is much easier for fabrication. Figures 8.2(b)(d) display the band structures of corresponding honeycomb lattice dots and triangular lattice antidots for $a = 40$ nm and $a' = 69$ nm. The potential magnitude and ratio of radius over inter-site distance are the same in both cases: $|V_0| = 6$ meV, ratio $= 0.2$. The linear dispersion does appear in the triangular lattice antidots band structure, similar to the honeycomb lattice case. In fact, the linear dispersion range is larger in the triangular lattice antidots. An example of the triangular antidot etch mask with $a' = 60$ nm is shown in Fig. 8.3.

Working with large inter-site distance, as in the case of triangular lattice antidots, will make the fabrication optimization much easier. On the other side, triangular lattice antidots will also enable us to create much smaller periods. For example, it is not hard to fabricate a triangular antidot lattice with $a' = 40$ nm with current equipments. This antidot lattice is equivalent to a honeycomb lattice with $a = 23$ nm, which is very challenging to make directly.

## 8.3 Changing the Fermi Level

With our shallow etch methods, the potential height $V_0$ and Fermi energy $E_F$ of AG lattices are strongly coupled. They are both modified by the etching profile of the AG lattices and can not be tuned separately. It is very hard to achieve both of them exactly right to have isolated MDFs. Adding another independent control would be essential to have a highly tunable AG system.

Figure 8.4 shows possible designs to tune the Fermi level by applying an external voltage through a metal gate. Fig. 8.4(a) shows a backgate design for honeycomb lattice dots. A heavily doped n+ layer is located about 1$\mu$m below the QW and a voltage is applied between the QW and n+ layer. The contact to the n+ layer could be accessed from the substrate while the contact to the 2DEG in the QW could

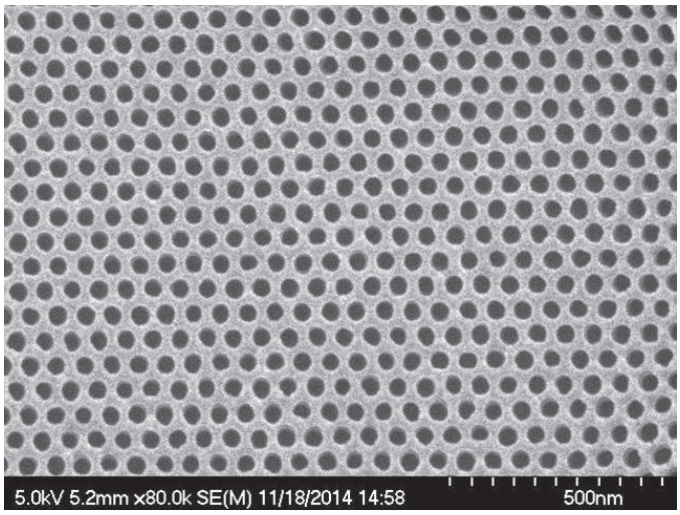


Figure 8.3: Triangular antidot lattice with $a' = 60$ nm. The bright parts are etch mask (PMMA coated by Au) while the dark parts are open area that can expose the QW sample to the ICP-RIE dry etching.

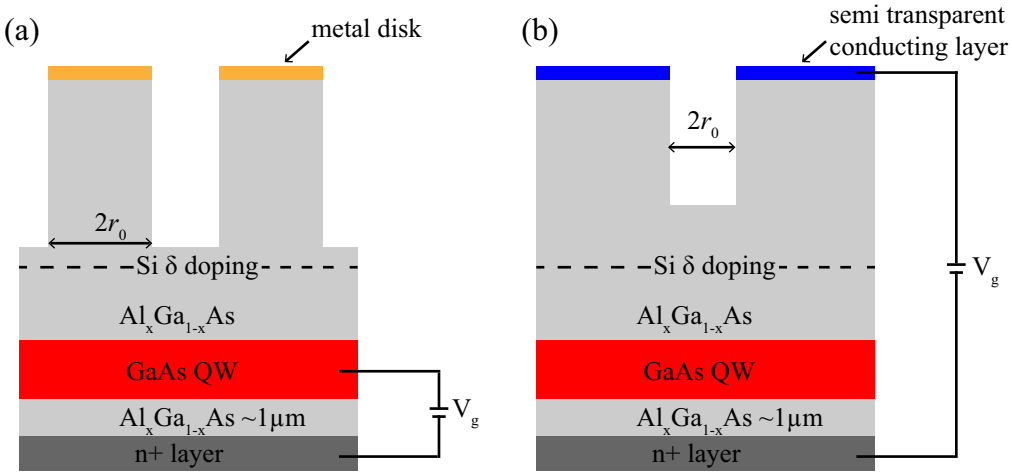


Figure 8.4: Tuning Fermi level by applying a gate. (a) A back gate design for honeycomb lattices. A heavily doped n+ GaAs layer is located 1 $\mu$m below the QW. A voltage is applied between the 2DEG in the QW and the n+ layer. (b) Gate design for triangular lattice antidots. An voltage is applied between a similar n+ layer below the QW and an additional semitransparent conducting layer (blue regions) deposited on the surface. It has the advantage of tuning the system when 2DEG in the QW is not conducting.

be achieved by AuGe/Ni/Au ohmic contact[119]. The same back gate design can be applied to the triangular lattice antidots as well (not shown in the figure). This design does not work well when electrons in the QW are localized under AG patterns in the weakly coupled systems, because the contact to 2DEG will be lost. This problem can be solved in the antidot case by a front gate using semitransparent metal layers such as NiCr[31, 71] on the top as shown in Fig. 8.4(b). This design allows further tuning of Fermi level even when the 2DEG in the QW is not conducting.

There are lots of more related designs and experiments that can be conducted such as applying magnetic field and/or doing transport measurements. New insights associated with such experiments should bring advancements in both fundamental and applied science.

# Chapter 9

# Concluding Remarks

In this dissertation I have presented recent advances in studies of artificial graphene on nano-patterned GaAs QWs. State of the art fabrication technologies used here opens up the possibility to integrate fascinating AG physics into semiconductor devices. The AG lattices provide highly tunable platforms to study Dirac fermions and related phenomena such as topological states linked to spin-orbit coupling. Graphene growth on dielectric substrate by MBE provides an alternative fabrication method of graphene, which has the potential to integrating graphene layers with semiconductor industry directly.

Small lattice constants (sub 100 nm) for AG lattices are essential to create well-developed Dirac cones, which impose challenges on fabrication technologies. We demonstrate the realizations of AG lattices with lattice constant as small as 40 nm on nano-patterned GaAs QWs. The high quality AG lattices with long range uniformity are achieved by optimized E-beam lithography and ICP-RIE dry etching as discussed in Chapter 4. The realizations of small period AG lattices on semiconductors provide venues for intriguing fundamental physics as well as applied science such as device integrations.

AG lattices mimic the lattice symmetry of graphene, which results in a linear

energy-momentum dispersion at the K and K' points of the Brillouin zone. I use a periodic muffin-tin potential to study electron states around Dirac cones as discussed in Chapter 5. The parameters required to create isolated, well-developed Dirac cones are discussed as well as the impact of individual parameter on the linear dispersion range. DOS and JDOS are calculated for AG band structures as well as the optimization of AG band structures. These calculations provide a basis to understand our RILS spectra as well as guidance to optimize sample design.

Optical spectra are powerful tools to probe electron states in our AG systems. In Chapter 6, optical emission and RILS are employed to characterize the AG systems. Optical emission spectra provide estimates for Fermi energy as well as potential magnitude. RILS of intersubband transitions reveal intriguing satellite peaks that is not present in the as-grown QWs. These additional peaks are interpreted as combined intersubband transitions with a change of AG band index, showing a remarkable agreement with calculated JDOS. In additional, RILS spectra find low-lying excitation peaks that are interpreted as direct transitions between AG bands within the same subband. Transitions around Dirac cone are selectively resonant enhanced by varying incident photon energies and the lineshape provides insights on the formation of Dirac cone. The results confirm the formation of AG miniband structures and well-developed Dirac cones.

Growth of nanocrystalline single layer and bilayer graphene has been achieved on sapphire substrate by MBE with a solid carbon source as discussed in Chapter 7. Raman spectroscopy reveals that fabrication of single layer, bilayer or multilayer graphene crucially depends on MBE growth conditions. Formation of etch pits, revealed by AFM, is regarded as evidence for a removal mechanism of carbon by reduction of sapphire. Tuning the interplay between carbon deposition and its removal, by varying the incident carbon flux and substrate temperature, should enable the growth of high quality graphene layers on large area sapphire substrates.

# References


[1] K. S. Novoselov, A. K. Geim, S. V. Morozov, D. Jiang, M. I. Katsnelson, I. V. Grigorieva, S. V. Dubonos, and A. A. Firsov. Two-dimensional gas of massless Dirac fermions in graphene. *Nature*, 438(7065):197–200, 2005.

[2] Y. B. Zhang, Y. W. Tan, H. L. Stormer, and P. Kim. Experimental observation of the quantum Hall effect and Berry's phase in graphene. *Nature*, 438(7065): 201–204, 2005.

[3] A. K. Geim and K. S. Novoselov. The rise of graphene. *Nat Mater*, 6(3): 183–191, 2007.

[4] P. R. Wallace. The band theory of graphite. *Phys. Rev.*, 71(9):622–634, 1947.

[5] J. L. Carter and J. A. Krumhansl. Band structure of graphite. *J. Chem. Phys.*, 21(12):2238–2239, 1953.

[6] J. W. Mcclure. Diamagnetism of graphite. *Phys. Rev.*, 104(3):666–671, 1956.

[7] R. Peierls. Quelques proprietes typiques des corps solides. *Annales de l'Institut Henri Poincare*, 5(3):177–222, 1935.

[8] L. D. Landau. Zur Theorie der phasenumwandlungen II. *Phys. Z. Sowjetunion*, 11:26–35, 1937.

[9] K. S. Novoselov, A. K. Geim, S. V. Morozov, D. Jiang, Y. Zhang, S. V. Dubonos, I. V. Grigorieva, and A. A. Firsov. Electric field effect in atomically thin carbon films. *Science*, 306(5696):666–669, 2004.

[10] K. S. Novoselov, D. Jiang, F. Schedin, T. J. Booth, V. V. Khotkevich, S. V. Morozov, and A. K. Geim. Two-dimensional atomic crystals. *Proc. Natl. Acad. Sci. U.S.A.*, 102(30):10451–10453, 2005.

[11] Y. B. Zhang, J. P. Small, W. V. Pontius, and P. Kim. Fabrication and electric-field-dependent transport measurements of mesoscopic graphite devices. *Appl. Phys. Lett.*, 86(7), 2005.

[12] C. H. Park and S. G. Louie. Making massless Dirac fermions from a patterned two-dimensional electron gas. *Nano Letters*, 9(5):1793–1797, 2009.

[13] M. Gibertini, A. Singha, V. Pellegrini, M. Polini, G. Vignale, A. Pinczuk, L. N. Pfeiffer, and K. W. West. Engineering artificial graphene in a two-dimensional electron gas. *Physical Review B*, 79(24), 2009.

[14] M. Polini, F. Guinea, M. Lewenstein, H. C. Manoharan, and V. Pellegrini. Artificial honeycomb lattices for electrons, atoms and photons. *Nature Nanotechnology*, 8(9):625–633, 2013.

[15] D. R. Hofstadter. Energy-levels and wave-functions of bloch electrons in rational and irrational magnetic-fields. *Phys. Rev. B*, 14(6):2239–2249, 1976.

[16] O. P. Sushkov and A. H. Castro Neto. Topological insulating states in laterally patterned ordinary semiconductors. *Phys. Rev. Lett.*, 110(18), 2013.

[17] K. K. Gomes, W. Mar, W. Ko, F. Guinea, and H. C. Manoharan. Designer Dirac fermions and topological phases in molecular graphene. *Nature*, 483(7389):306–310, 2012.

[18] B. Wunsch, F. Guinea, and F. Sols. Dirac-point engineering and topological phase transitions in honeycomb optical lattices. *New J. Phys.*, 10, 2008.

[19] P. Soltan-Panahi, J. Struck, P. Hauke, A. Bick, W. Plenkers, G. Meineke, C. Becker, P. Windpassinger, M. Lewenstein, and K. Sengstock. Multi-component quantum gases in spin-dependent hexagonal lattices. *Nature Physics*, 7(5):434–440, 2011.

[20] L. Tarruell, D. Greif, T. Uehlinger, G. Jotzu, and T. Esslinger. Creating, moving and merging Dirac points with a Fermi gas in a tunable honeycomb lattice. *Nature*, 483(7389):302–U91, 2012.

[21] O. Peleg, G. Bartal, B. Freedman, O. Manela, M. Segev, and D. N. Christodoulides. Conical diffraction and gap solitons in honeycomb photonic lattices. *Phys. Rev. Lett.*, 98(10), 2007.

[22] R. A. Sepkhanov, Y. B. Bazaliy, and C. W. J. Beenakker. Extremal transmission at the Dirac point of a photonic band structure. *Phys. Rev. A*, 75(6), 2007.

[23] R. A. Sepkhanov, J. Nilsson, and C. W. J. Beenakker. Proposed method for detection of the pseudospin-1/2 Berry phase in a photonic crystal with a Dirac spectrum. *Phys. Rev. B*, 78(4), 2008.

[24] F. D. M. Haldane and S. Raghu. Possible realization of directional optical waveguides in photonic crystals with broken time-reversal symmetry. *Phys. Rev. Lett.*, 100(1), 2008.

[25] M. C. Rechtsman, J. M. Zeuner, A. Tunnermann, S. Nolte, M. Segev, and A. Szameit. Strain-induced pseudomagnetic field and photonic Landau levels in dielectric structures. *Nature Photonics*, 7(2):153–158, 2013.

[26] L. Esaki and R. Tsu. Superlattice and negative differential conductivity in semiconductors. *IBM J. Res. Dev.*, 14(1):61–65, 1970.

[27] G. Bernstein and D. K. Ferry. Negative differential conductivity in lateral surface superlattices. *J. Vac. Sci. Technol. B*, 5(4):964–966, 1987.

[28] D. Weiss, K. v. Klitzing, K. Ploog, and G. Weimann. Magnetoresistance oscillations in a two-dimensional electron-gas induced by a submicrometer periodic potential. *Europhysics Letters*, 8(2):179–184, 1989.

[29] J. S. Weiner, G. Danan, A. Pinczuk, J. Valladares, L. N. Pfeiffer, and K. West. Electron-gas in semiconductor multiple quantum wires: spatially indirect optical transitions. *Phys. Rev. Lett.*, 63(15):1641–1644, 1989.

[30] T. Egeler, G. Abstreiter, G. Weimann, T. Demel, D. Heitmann, P. Grambow, and W. Schlapp. Anisotropic plasmon dispersion in a lateral quantum-wire superlattice. *Phys. Rev. Lett.*, 65(14):1804–1807, 1990.

[31] A. Lorke, J. P. Kotthaus, and K. Ploog. Coupling of quantum dots on GaAs. *Physical Review Letters*, 64(21):2559–2562, 1990.

[32] A. Lorke, I. Jejina, and J. P. Kotthaus. Far-infrared response of lateral superlattices in high magnetic-fields. *Physical Review B*, 46(19):12845–12848, 1992.

[33] D. Heitmann and J. P. Kotthaus. The spectroscopy of quantum-dot arrays. *Physics Today*, 46(6):56–63, 1993.

[34] J. P. Kotthaus. Spectroscopy on lateral superlattices. *Nato Adv Sci Inst Se*, 248:247–263, 1993.

[35] L. Pfeiffer and K. W. West. The role of MBE in recent quantum Hall effect physics discoveries. *Physica E*, 20(1-2):57–64, 2003.

[36] G. De Simoni, A. Singha, M. Gibertini, B. Karmakar, M. Polini, V. Piazza, L. N. Pfeiffer, K. W. West, F. Beltram, and V. Pellegrini. Delocalized-localized transition in a semiconductor two-dimensional honeycomb lattice. *Applied Physics Letters*, 97(13), 2010.

[37] A. Singha, M. Gibertini, B. Karmakar, S. Yuan, M. Polini, G. Vignale, M. I. Katsnelson, A. Pinczuk, L. N. Pfeiffer, K. W. West, and V. Pellegrini. Two-dimensional Mott-Hubbard electrons in an artificial honeycomb lattice. *Science*, 332(6034):1176–1179, 2011.

[38] E. Rasanen, C. A. Rozzi, S. Pittalis, and G. Vignale. Electron-electron interactions in artificial graphene. *Phys. Rev. Lett.*, 108(24), 2012.

[39] L. Nadvornik, M. Orlita, N. A. Goncharuk, L. Smrcka, V. Novak, V. Jurka, K. Hruska, Z. Vyborny, Z. R. Wasilewski, M. Potemski, and K. Vyborny. From laterally modulated two-dimensional electron gas towards artificial graphene. *New Journal of Physics*, 14, 2012.

[40] I. Kylanpaa, M. Aichinger, S. Janecek, and E. Rasanen. Finite-size effects and interactions in artificial graphene formed by repulsive scatterers. *J Phys-Condens Mat*, 27(42), 2015.

[41] K. v. Klitzing, G. Dorda, and M. Pepper. New method for high-accuracy determination of the fine-structure constant based on quantized Hall resistance. *Phys. Rev. Lett.*, 45(6):494–497, 1980.

[42] D. C. Tsui, H. L. Stormer, and A. C. Gossard. Two-dimensional magnetotransport in the extreme quantum limit. *Phys. Rev. Lett.*, 48(22):1559–1562, 1982.

[43] H. L. Stormer, A. Chang, D. C. Tsui, J. C. M. Hwang, A. C. Gossard, and W. Wiegmann. Fractional quantization of the Hall-effect. *Phys. Rev. Lett.*, 50(24): 1953–1956, 1983.

[44] M. E. Levinshtein, S. L. Rumyantsev, and M. Shur. *Handbook series on semiconductor parameters*. World Scientific, 1996.

[45] D. A. B. Miller. *Optical Physics of Quantum Wells*, pages 239–266. Quantum Dynamics of Simple Systems (Institute of Physics, London 1996).

[46] G. Bastard. *Wave mechanics applied to semiconductor heterostructures*. John Wiley and Sons Inc, United States, 1990.

[47] J. H. Davies. *The physics of low-dimensional semiconductors : an introduction*. Cambridge University Press, 1998.

[48] I found a free package from Gregory Snider specifically helpful in self-cosistent calculation of band diagram of GaAs quantum well, which can be downloaded from http://www3.nd.edu/ gsnider/. I believe there also exist lots of other good software for the self-consistent band calculation of heterestructures.

[49] C. V. Raman and K. S. Krishnan. A new type of secondary radiation. *Nature*, 121:501–502, 1928.

[50] W. H. Weber and R. Merlin. *Raman scattering in materials science*. Springer, 2000.

[51] W. Hayes and R. Loudon. *Scattering of light by crystals*. Wiley, 1978.

[52] P. A. Wolff. Thomson and Raman scattering by mobile electrons in crystals. *Phys Rev Lett*, 16(6):225, 1966.

[53] Y. Yafet. Raman scattering by carriers in Landau levels. *Phys. Rev.*, 152(2): 858, 1966.

[54] F. A. Blum. Inelastic light scattering from semiconductor plasmas in a magnetic field. *Phys Rev B-Solid St*, 1(3):1125, 1970.

[55] R. Loudon. *The quantum theory of light*. Clarendon Press, 1973.

[56] G. B. Wright and N. Y. University. *Light scattering spectra of solids; proceedings*. Springer-Verlag New York, 1969.

[57] G. Abstreiter, M. Cardona, and A. Pinczuk. Light-scattering by free carrier excitations in semiconductors. *Top Appl Phys*, 54:5–150, 1984.

[58] E. O. Kane. Band structure of Indium Antimonide. *J Phys Chem Solids*, 1(4): 249–261, 1957.

[59] D. C. Hamilton and A. L. McWhorter. *Raman Scattering from Spin Density Fluctuations in n - GaAs*, pages 309–316. Springer Berlin Heidelberg, Berlin, Heidelberg, 1969.

[60] *Semiconductors - Basic Data*. Springer, 1996. ISBN 9783642976759 9783642976773 (print).

[61] E. Burstein, A. Pinczuk, and D. L. Mills. Inelastic light-scattering by charge carrier excitations in two-dimensional plasmas - theoretical considerations. *Surface Science*, 98(1-3):451–468, 1980.

[62] E. Burstein, A. Pinczuk, and S. Buchner. *Physics of Semiconductors 1978*. Institute of Physics, London, 1979.

[63] A. Pinczuk, H. L. Stormer, R. Dingle, J. M. Worlock, W. Wiegmann, and A. C. Gossard. Observation of intersubband excitations in a multilayer 2 dimensional electron-gas. *Solid State Commun.*, 32(11):1001–1003, 1979.

[64] G. Abstreiter and K. Ploog. Inelastic light-scattering from a quasi-2-dimensional electron-system in GaAs-$Al_xGa_{1-x}As$ heterojunctions. *Phys. Rev. Lett.*, 42(19):1308–1311, 1979.

[65] G. Bastard. *Wave Mechanics Applied to Semiconductor Heterostructures*. EDP SCIENCES, 1988.

[66] M. Gurioli, J. Martinez-Pastor, M. Colocci, C. Deparis, B. Chastaingt, and J. Massies. Thermal escape of carriers out of GaAs/$Al_xGa_{1-x}As$ quantum-well structures. *Phys. Rev. B*, 46(11):6922–6927, 1992.

[67] A. Pinczuk, J. Shah, H. L. Stormer, R. C. Miller, A. C. Gossard, and W. Wiegmann. Investigation of optical processes in a semiconductor 2D electron-plasma. *Surface Science*, 142(1-3):492–497, 1984.

[68] A. Pinczuk, J. Shah, R. C. Miller, A. C. Gossard, and W. Wiegmann. Optical processes of 2D electron-plasma in GaAs-(AlGa)As heterostructures. *Solid State Commun.*, 50(8):735–739, 1984.

[69] J. M. Worlock, A. Pinczuk, Z. J. Tien, C. H. Perry, H. Stormer, R. Dingle, A. C. Gossard, W. Wiegmann, and R. L. Aggarwal. Spectroscopy of Landau transitions of two-dimensional electron gases. *Solid State Commun.*, 40(9):867–871, 1981.

[70] A. Mooradian and H. Y. Fan. Recombination emission in InSb. *Phys. Rev.*, 148(2):873, 1966.

[71] R. W. Winkler, J. P. Kotthaus, and K. Ploog. Landau-band conductivity in a two-dimensional electron-system modulated by an artificial one-dimensional superlattice potential. *Physical Review Letters*, 62(10):1177–1180, 1989.

[72] A. Soibel, U. Meirav, D. Mahalu, and H. Shtrikman. Fabrication and transport measurements of honeycomb surface superlattices. *Semiconductor Science and Technology*, 11(11):1756–1760, 1996.

[73] S. Melinte, M. Berciu, C. Zhou, E. Tutuc, S. J. Papadakis, C. Harrison, E. P. De Poortere, M. Wu, P. M. Chaikin, M. Shayegan, R. N. Bhatt, and R. A. Register. Laterally modulated 2D electron system in the extreme quantum limit. *Physical Review Letters*, 92(3), 2004.

[74] S. Hugger, T. Heinzel, and T. Thurn-Albrecht. Small scale lateral superlattices in two-dimensional electron gases prepared by diblock copolymer masks. *Applied Physics Letters*, 93(10), 2008.

[75] S. Yasin, D. G. Hasko, and H. Ahmed. Comparison of sensitivity and exposure latitude for polymethylmethacrylate, UVIII, and calixarene using conventional dip and ultrasonically assisted development. *J. Vac. Sci. Technol. B*, 17(6): 3390–3393, 1999.

[76] W. C. Hu, K. Sarveswaran, M. Lieberman, and G. H. Bernstein. Sub-10 nm electron beam lithography using cold development of poly(methylmethacrylate). *J. Vac. Sci. Technol. B*, 22(4):1711–1716, 2004.

[77] T. Maeda, J. W. Lee, R. J. Shul, J. Han, J. Hong, E. S. Lambers, S. J. Pearton, C. R. Abernathy, and W. S. Hobson. Inductively coupled plasma etching of III-V semiconductors in $BCl_3$-based chemistries I. GaAs, GaN, GaP, GaSb and AlGaAs. *Applied Surface Science*, 143(1-4):174–182, 1999.

[78] M. Volatier, D. Duchesne, R. Morandotti, R. Ares, and V. Aimez. Extremely high aspect ratio GaAs and GaAs/AlGaAs nanowaveguides fabricated using chlorine ICP etching with $N_2$-promoted passivation. *Nanotechnology*, 21(13), 2010.

[79] D. A. Czaplewski, M. V. Holt, and L. E. Ocola. The range and intensity of backscattered electrons for use in the creation of high fidelity electron beam lithography patterns. *Nanotechnology*, 24(30), 2013.

[80] D. Scarabelli, S. Wang, A. Pinczuk, S. J. Wind, Y. Y. Kuznetsova, L. N. Pfeiffer, K. West, G. C. Gardner, M. J. Manfra, and V. Pellegrini. Fabrication of artificial graphene in a GaAs quantum heterostructure. *J. Vac. Sci. Technol. B*, 33(6), 2015.

[81] N. W. Ashcroft and N. D. Mermin. *Solid State Physics*. Cengage Learning, 1976.

[82] C. Scheuller. *Inelastic light scattering of semiconductor nanostructures : fundamentals and recent advances*, page 30. Springer, 2006.

[83] S. Wang, D. Scarabelli, Y. Y. Kuznetsova, S. J. Wind, A. Pinczuk, V. Pellegrini, M. J. Manfra, G. C. Gardner, L. N. Pfeiffer, and K. West. Observation of electron states of small period artificial graphene in nano-patterned GaAs quantum wells. *Appl. Phys. Lett.*, submitted, 2016.

[84] J. S. Lee, Y. Iwasa, and N. Miura. Observation of the Fermi edge anomaly in the absorption and luminescence spectra of n-type modulation-doped GaAs-AlGaAs quantum-wells. *Semicond Sci Tech*, 2(10):675–678, 1987.

[85] A. Pinczuk, S. Schmittrink, G. Danan, J. P. Valladares, L. N. Pfeiffer, and K. W. West. Large exchange interactions in the electron-gas of GaAs quantum wells. *Phys. Rev. Lett.*, 63(15):1633–1636, 1989.

[86] S. Ernst, A. R. Goni, K. Syassen, and K. Eberl. Collapse of the Hartree term of the Coulomb interaction in a very dilute 2D electron-gas. *Phys Rev Lett*, 72 (25):4029–4032, 1994.

[87] C. Scheuller. *Inelastic light scattering of semiconductor nanostructures : fundamentals and recent advances*, page 52. Springer, 2006.

[88] This Gaussian broadening smoothes JDOS, but it does not change peak positions or overall shape of JDOS. The FWHM of broadening used here (0.2 meV) considers the spectrometer resolution used in RILS (0.1 meV) and the variation of diameter of pillars.

[89] C. L. Kane and E. J. Mele. Quantum spin Hall effect in graphene. *Phys. Rev. Lett.*, 95(22), 2005.

[90] C. Albrecht, J. H. Smet, K. v. Klitzing, D. Weiss, V. Umansky, and H. Schweizer. Evidence of Hofstadter's fractal energy spectrum in the quantized Hall conductance. *Phys. Rev. Lett.*, 86(1):147–150, 2001.

[91] C. R. Dean, L. Wang, P. Maher, C. Forsythe, F. Ghahari, Y. Gao, J. Katoch, M. Ishigami, P. Moon, M. Koshino, T. Taniguchi, K. Watanabe, K. L. Shepard, J. Hone, and P. Kim. Hofstadter's butterfly and the fractal quantum Hall effect in moire superlattices. *Nature*, 497(7451):598–602, 2013.

[92] L. A. Ponomarenko, R. V. Gorbachev, G. L. Yu, D. C. Elias, R. Jalil, A. A. Patel, A. Mishchenko, A. S. Mayorov, C. R. Woods, J. R. Wallbank, M. Mucha-Kruczynski, B. A. Piot, M. Potemski, I. V. Grigorieva, K. S. Novoselov, F. Guinea, V. I. Fal'ko, and A. K. Geim. Cloning of Dirac fermions in graphene superlattices. *Nature*, 497(7451):594–597, 2013.

[93] S. Wang, D. Scarabelli, Y. Y. Kuznetsova, L. N. Pfeiffer, K. West, G. C. Gardner, M. J. Manfra, V. Pellegrini, S. J. Wind, and A. Pinczuk. Observation of Dirac bands in artificial graphene realized in small period nano-patterned GaAs quantum wells. *Nat Nanotechnol*, submitted, 2015.

[94] M. S. Fuhrer, C. N. Lau, and A. H. MacDonald. Graphene: materially better carbon. *MRS Bulletin*, 35(4):289–295, 2010.

[95] C. Berger, Z. M. Song, T. B. Li, X. B. Li, A. Y. Ogbazghi, R. Feng, Z. T. Dai, A. N. Marchenkov, E. H. Conrad, P. N. First, and W. A. de Heer. Ultrathin epitaxial graphite: 2D electron gas properties and a route toward graphene-based nanoelectronics. *J. Phys. Chem. B*, 108(52):19912–19916, 2004.

[96] X. S. Li, W. W. Cai, J. H. An, S. Kim, J. Nah, D. X. Yang, R. Piner, A. Velamakanni, I. Jung, E. Tutuc, S. K. Banerjee, L. Colombo, and R. S. Ruoff. Large-area synthesis of high-quality and uniform graphene films on copper foils. *Science*, 324(5932):1312–1314, 2009.

[97] B. Hu, H. Ago, Y. Ito, K. Kawahara, M. Tsuji, E. Magome, K. Sumitani, N. Mizuta, K.-i. Ikeda, and S. Mizuno. Epitaxial growth of large-area single-layer graphene over Cu(111)/sapphire by atmospheric pressure CVD. *Carbon*, 50(1): 57–65, 2012.

[98] A. Cho and J. Arthur. Molecular beam epitaxy. *Progress in Solid State Chemistry*, 10:157 – 191, 1975. ISSN 0079-6786.

[99] S. K. Jerng, D. S. Yu, Y. S. Kim, J. Ryou, S. Hong, C. Kim, S. Yoon, D. K. Efetov, P. Kim, and S. H. Chun. Nanocrystalline graphite growth on sapphire by carbon molecular beam epitaxy. *J. Phys. Chem. C*, 115(11):4491–4494, 2011.

[100] S. K. Jerng, J. H. Lee, D. S. Yu, Y. S. Kim, J. Ryou, S. Hong, C. Kim, S. Yoon, and S. H. Chun. Graphitic carbon growth on MgO(100) by molecular beam epitaxy. *J. Phys. Chem. C*, 116(13):7380–7385, 2012.

[101] J. M. Garcia, U. Wurstbauer, A. Levy, L. N. Pfeiffer, A. Pinczuk, A. S. Plaut, L. Wang, C. R. Dean, R. Buizza, A. M. Van Der Zande, J. Hone, K. Watanabe, and T. Taniguchi. Graphene growth on h-BN by molecular beam epitaxy. *Solid State Commun.*, 152(12):975–978, 2012.

[102] Z. L. Liu, J. Tang, C. Y. Kang, C. W. Zou, W. S. Yan, and P. S. Xu. Effect of substrate temperature on few-layer graphene grown on $Al_2O_3$ (0001) via direct carbon atoms deposition. *Solid State Commun.*, 152(11):960–963, 2012.

[103] U. Wurstbauer, T. Schiros, C. Jaye, A. S. Plaut, R. He, A. Rigosi, C. Gutierrez, D. Fischer, L. N. Pfeiffer, A. N. Pasupathy, A. Pinczuk, and J. M. Garcia. Molecular beam growth of graphene nanocrystals on dielectric substrates. *Carbon*, 50(13):4822–4829, 2012.

[104] M. H. Oliveira Jr, T. Schumann, R. Gargallo-Caballero, F. Fromm, T. Seyller, M. Ramsteiner, A. Trampert, L. Geelhaar, J. M. J. Lopes, and H. Riechert. Mono- and few-layer nanocrystalline graphene grown on $Al_2O_3$ by molecular beam epitaxy. *Carbon*, 56(0):339–350, 2013.

[105] G. Lippert, J. Dabrowski, Y. Yamamoto, F. Herziger, J. Maultzsch, J. Baringhaus, C. Tegenkamp, M. C. Lemme, W. Mehr, and G. Lupina. Molecular beam epitaxy of graphene on mica. *Phys. Status Solidi B*, 249(12):2507–2510, 2012.

[106] J. H. Cox and L. M. Pidgeon. An investigation of the Aluminum-Oxygen-Carbon system. *Can. J. Chem.*, 41(3):671–683, 1963.

[107] S. Wang, L. F. dos Santos, U. Wurstbauer, L. Wang, L. N. Pfeiffer, J. Hone, J. M. Garcia, and A. Pinczuk. Single- and bi-layer graphene grown on sapphire by molecular beam epitaxy. *Solid State Commun.*, 189:15–20, 2014.

[108] J. Hwang, M. Kim, D. Campbell, H. A. Alsalman, J. Y. Kwak, S. Shivaraman, A. R. Woll, A. K. Singh, R. G. Hennig, S. Gorantla, M. H. Ruemmeli, and M. G. Spencer. van der Waals epitaxial growth of graphene on sapphire by chemical vapor deposition without a metal catalyst. *ACS Nano*, 7(1):385–395, 2013.

[109] J. M. Garcia, R. He, M. P. Jiang, J. Yan, A. Pinczuk, Y. M. Zuev, K. S. Kim, P. Kim, K. Baldwin, K. W. West, and L. N. Pfeiffer. Multilayer graphene films grown by molecular beam deposition. *Solid State Commun.*, 150(17-18): 809–811, 2010.

[110] M. A. Pimenta, G. Dresselhaus, M. S. Dresselhaus, L. G. Cancado, A. Jorio, and R. Saito. Studying disorder in graphite-based systems by Raman spectroscopy. *Phys. Chem. Chem. Phys.*, 9(11):1276–1291, 2007.

[111] A. C. Ferrari. Raman spectroscopy of graphene and graphite: Disorder, electron-phonon coupling, doping and nonadiabatic effects. *Solid State Commun.*, 143(1-2):47–57, 2007.

[112] D. Graf, F. Molitor, K. Ensslin, C. Stampfer, A. Jungen, C. Hierold, and L. Wirtz. Spatially resolved Raman spectroscopy of single- and few-layer graphene. *Nano Lett.*, 7(2):238–242, 2007.

[113] L. M. Malard, J. Nilsson, D. C. Elias, J. C. Brant, F. Plentz, E. S. Alves, A. H. Castro Neto, and M. A. Pimenta. Probing the electronic structure of bilayer graphene by Raman scattering. *Phys. Rev. B*, 76(20), 2007.

[114] J. Yan, Y. Zhang, P. Kim, and A. Pinczuk. Electric field effect tuning of electron-phonon coupling in graphene. *Phys. Rev. Lett.*, 98(16), 2007.

[115] C.-M. Liu, J.-C. Chen, Y.-C. Huang, and H.-L. Hsieh. The morphology of etch pits on a sapphire surface. *J. Phys. Chem. Solids*, 69(2-3):572–575, 2008.

[116] F. Cuccureddu, S. Murphy, I. V. Shvets, M. Porcu, H. W. Zandbergen, N. S. Sidorov, and S. I. Bozhko. Surface morphology of c-plane sapphire (alpha-alumina) produced by high temperature anneal. *Surface Science*, 604(15-16): 1294–1299, 2010.

[117] M. Kruesi, M. E. Galvez, M. Halmann, and A. Steinfeld. Solar aluminum production by vacuum carbothermal reduction of alumina-thermodynamic and experimental analyses. *Metall Mater Trans B*, 42(1):254–260, 2011.

[118] Ref. 25 reports that at a pressure of about $10^{-3}$ Torr there is a step-like behavior in the carbo-thermal reduction of alumina at a temperature $T_o \approx 1100$ ℃ in which no carbo-thermal reduction occurs for temperature $T < T_o$.

[119] E. J. Koop, M. J. Iqbal, F. Limbach, M. Boute, B. J. van Wees, D. Reuter, A. D. Wieck, B. J. Kooi, and C. H. van der Wal. On the annealing mechanism of AuGe/Ni/Au ohmic contacts to a two-dimensional electron gas in GaAs/$Al_xGa_{1-x}$As heterostructures. *Semicond Sci Tech*, 28(2), 2013.

# Appendix A

# Abbreviations

| variable | definition |
|---|---|
| 2D | two dimensional |
| AG | aritificial graphene |
| CDE | charge density excitation |
| DOS | density of states |
| FWHM | full width at halft maximum |
| ICP | inductively coupled plasma |
| JDOS | joint density of states |
| MBE | molecular beam epitaxy |
| MDF | massless Dirac fermion |
| PL | photoluminescence |
| QW | quantum well |
| RIE | reactive-ion etching |
| RILS | resonant inelastic light scattering |
| SDE | spin density excitation |
| SPE | single particle excitation |

Table A.1: List of abbreviations used in this dissertation.

# Appendix B

# Samples

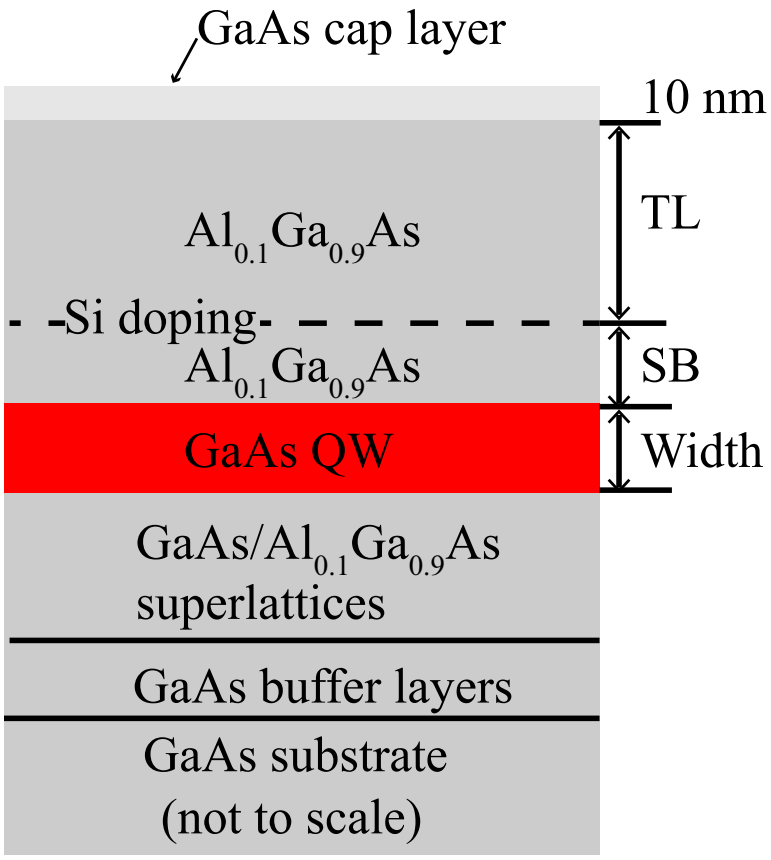


Figure B.1: Layout of GaAs QW used in this dissertation.

| sample# | n | $\mu$ | Width(nm) | SB(nm) | TL(nm) |
|---|---|---|---|---|---|
| L06-27-14.1 | 1.80 | 3.2 | 25 | 30 | 70 |
| L02-12-16.2 | 1.90 | 1.5 | 25 | 30 | 70 |
| L04-04-16.1 | 1.67 | 3.6 | 25 | 30 | 70 |
| L04-05-16.1 | 1.79 | 3.9 | 25 | 30 | 70 |
| L06-18-13.2 | 1.70 | 4.5 | 25 | 30 | 100 |
| L06-13-13.1 | 0.93 | 9.9 | 25 | 60 | 100 |
| L10-20-14.1 | 2.08 | 0.71 | 25 | 20 | 50 |
| L10-20-14.2 | 1.58 | 2.3 | 25 | 30 | 50 |
| M11-11-14.1 | 3.00 | 4.8 | 25 | 30 | 40 |
| M11-11-14.2 | 4.50 | 0.98 | 25 | 20 | 40 |
| M11-21-14.1 | 2.30 | 4.56 | 25 | 30 | 40 |

Table B.1: List of samples used for the studies of AG lattices. Our results show that sample L06-27-14.1 is most suitable for investigations of AG lattices (sample L02-12-16.2, L04-04-16.1, L04-05-16.1 are duplicates of L06-27-14.1, the density and mobility slightly vary due to different MBE chamber conditions). The electron density is listed in units of $10^{11}\text{cm}^{-2}$ and the mobility is listed in units of $10^{6}\text{cm}^{2}/(\text{Vs})$. Width, SB, TL are defined in Fig. B.1.

# Appendix C

# Matlab code for Calculating AG Bands

```
%% parameter definition
%constant definition
m0=9.109e-31;
c=2.998e8;
h=6.626e-34;
hbar=h/2/pi;
%me=0.45*m0;
me=0.067*m0;
e=1.602e-19;

%period of lattice anm, ratio of pillar radius over period, ...
   potential V0
anm=40;
a=anm*10^-9;
ratio=0.30;
V0=-6.0;

%period of reciprocal lattice and energy scale
b=4*pi/3/3^0.5/a;
E0=hbar^2/2/me*b^2/e*1000;


%% define reciprocal lattice vector in unit of b
K_n=48;
K_r=zeros(K_n,2);

K_r(1,:)=[0,0];

K_r(2,:)=[0,3^0.5];
K_r(3,:)=[3/2,3^0.5/2];
K_r(4,:)=[-3/2,3^0.5/2];
K_r(5,:)=[3/2,-3^0.5/2];
K_r(6,:)=[-3/2,-3^0.5/2];
K_r(7,:)=[0,-3^0.5];
```

```
34
35 K_r(8,:)=[3/2,3*3^0.5/2];
36 K_r(9,:)=K_r(3,:)+K_r(5,:);
37 K_r(10,:)=K_r(5,:)+K_r(7,:);
38 K_r(11,:)=K_r(7,:)+K_r(6,:);
39 K_r(12,:)=K_r(6,:)+K_r(4,:);
40 K_r(13,:)=K_r(4,:)+K_r(2,:);
41
42 K_r(14,:)=K_r(2,:)*2;
43 K_r(15,:)=K_r(3,:)*2;
44 K_r(16,:)=K_r(4,:)*2;
45 K_r(17,:)=K_r(5,:)*2;
46 K_r(18,:)=K_r(6,:)*2;
47 K_r(19,:)=K_r(7,:)*2;
48
49 K_r(20,:)=K_r(5,:)+K_r(9,:);
50 K_r(21,:)=K_r(5,:)+K_r(15,:);
51 K_r(22,:)=K_r(3,:)+K_r(15,:);
52 K_r(23,:)=K_r(2,:)+K_r(15,:);
53 K_r(24,:)=K_r(2,:)+K_r(8,:);
54 K_r(25,:)=K_r(2,:)+K_r(14,:);
55 K_r(26,:)=K_r(2,:)+K_r(13,:);
56 K_r(27,:)=K_r(2,:)+K_r(16,:);
57 K_r(28,:)=K_r(4,:)+K_r(16,:);
58 K_r(29,:)=K_r(4,:)+K_r(12,:);
59 K_r(30,:)=K_r(6,:)+K_r(12,:);
60 K_r(31,:)=K_r(6,:)+K_r(18,:);
61 K_r(32,:)=K_r(6,:)+K_r(11,:);
62 K_r(33,:)=K_r(7,:)+K_r(11,:);
63 K_r(34,:)=K_r(7,:)+K_r(19,:);
64 K_r(35,:)=K_r(7,:)+K_r(10,:);
65 K_r(36,:)=K_r(7,:)+K_r(17,:);
66 K_r(37,:)=K_r(5,:)+K_r(17,:);
67
68 K_r(38,:)=K_r(5,:)+K_r(20,:);
69 K_r(39,:)=K_r(5,:)+K_r(21,:);
70 K_r(40,:)=K_r(5,:)+K_r(22,:);
71 K_r(41,:)=K_r(3,:)+K_r(22,:);
72 K_r(42,:)=K_r(3,:)+K_r(23,:);
73 K_r(43,:)=K_r(3,:)+K_r(24,:);
74 K_r(44,:)=K_r(2,:)+K_r(24,:);
75 K_r(45,:)=K_r(2,:)+K_r(25,:);
76 K_r(46,:)=K_r(2,:)+K_r(26,:);
77 K_r(47,:)=K_r(2,:)+K_r(27,:);
78 K_r(48,:)=K_r(4,:)+K_r(27,:);
79
80
81 %% calculate interaction elements
82
83 M=zeros(K_n,K_n);
84
85 for i =1:K_n
86     for j=i+1:K_n
87
```

```
88              G=K_r(i,:)-K_r(j,:);%K1-K2
89
90              G_m=(G(1,1)^2+G(1,2)^2)^0.5*4*pi/3^1.5;%abs(G)
91              c1=2*cos(2*pi/3^1.5*G(1,2))*(2/3^1.5)*...
92                  (2*pi*besselj(1,G_m*ratio)*ratio/G_m);%integral
93
94              M(i,j)=c1*V0/E0;
95              M(j,i)=M(i,j);
96
97      end
98  end
99
100
101 % number k points for 1/12 BZ
102 N=40000;
103
104 dk=(3^0.5/8/N)^0.5;
105
106 % calculate band structure along high symmetry direction
107 len1=3^0.5/2;
108 len2=0.5;
109 len3=1.0;
110
111 n1=173;
112 n2=100;
113 n3=200;
114 dl1=len1/173;
115 dl2=len2/100;
116 dl3=len3/200;
117
118 x1=0:dl1:len1;
119 x2=0:dl2:len2;
120 x3=0:dl3:len3;
121
122 nsize=473;
123 result=zeros(K_n,nsize);
124
125 n=0;
126 x=0;
127 for y=0:dl1:len1 % from Gamma to M point
128
129         for i=1:K_n
130             M(i,i)=(x-K_r(i,1))^2+(y-K_r(i,2))^2;
131         end
132
133         E=eig(M)*E0;
134         E=sort(E);
135         % store result
136         n=n+1;
137         result(:,n)=E;
138 end
139
140 y=3^0.5/2;
141 for x=0:dl2:len2 % from M to K point
```

```
142
143         for i=1:K_n
144             M(i,i)=(x-K_r(i,1))^2+(y-K_r(i,2))^2;
145         end
146
147         E=eig(M)*E0;
148         E=sort(E);
149         % store result
150         n=n+1;
151         result(:,n)=E;
152
153 end
154
155 for l=0:dl3:len3 % from K to Gamma point
156
157         x=(1-l)/2;
158         y=(1-l)/2*3^0.5;
159
160         for i=1:K_n
161             M(i,i)=(x-K_r(i,1))^2+(y-K_r(i,2))^2;
162         end
163
164         E=eig(M)*E0;
165         E=sort(E);
166         % store result
167         n=n+1;
168         result(:,n)=E;
169 end
170
171
172
173 result=result-result(1);%set bottom of bands to zero
174
175 %% plot AG bands
176 figure
177 set(gca,'Fontsize',18);
178 hold on
179 plot(x1,result(:,1:n1+1),'k','Linewidth',2);
180 plot(x2+len1,result(:,n1+2:n1+n2+2),'k','Linewidth',2);
181 plot(x3+len1+len2,result(:,n1+n2+3:end),'k','Linewidth',2);
182
183 % set figure labels and range
184 ylabel('Energy(meV)');
185 title([num2str(anm),'nm pattern',' V_0=',num2str(V0),' meV ...
       ratio=',num2str(ratio)]);
186 set(gca,'XTickLabel',{'';'M';'K';''},'XTick',[0,0.866,1.366,2.366]);
187 ylim([0,6]);
188 xlim([0,2.366]);
189 box on;
```